SQUID FUNDAMENTALS

JOHN CLARKE
Department of Physics, University of California
and
Materials Sciences Division, Lawrence Berkeley National Laboratory
Berkeley, California 94720

ABSTRACT. DC Superconducting QUantum Interference Devices (SQUIDs) incorporating two resistively shunted tunnel junctions are routinely fabricated from thin films of low-transition-temperature (T_c) superconductors. An integrated superconducting input coil couples the SQUID to the signal source. Typical dc SQUIDs operating at 4.2K have a magnetic flux noise of $10^{-6}\Phi_0\ \mathrm{Hz}^{-1/2}$ corresponding to a noise energy of $10^{-32}\ \mathrm{JHz}^{-1}$ at frequencies f above the 1/f noise knee, which may be below 1Hz ($\Phi_0 \equiv h/2e$ is the flux quantum). Recently, the performance of thin-film rf SQUIDs, which involve a single junction, has improved significantly, and the sensitivity of a device operated at 3 GHz approaches that of dc SQUIDs. In the last two years, there have been dramatic improvements in the performance of both dc and rf SQUIDs made from high-T_c thin films, and noise energies of about $10^{-30}\ \mathrm{JHz}^{-1}$ and magnetic field noise levels below $10\mathrm{fTHz}^{-1/2}$ at frequencies down to a few Hz have been achieved at 77K. Multilayer thin-film flux transformers are now available. Instruments based on low-T_c SQUIDs include magnetometers, magnetic gradiometers, voltmeters, susceptometers, amplifiers, and displacement sensors; their applications vary from neuromagnetism and magnetotelluric sounding to the detection of gravity waves and magnetic resonance.

1. Introduction

Superconducting QUantum Interference Devices (SQUIDs) are the most sensitive detectors of magnetic flux currently available. They are amazingly versatile, being able to measure any physical quantity that can be converted to a flux, for example, magnetic field, magnetic field gradient, current, voltage, displacement, and magnetic susceptibility. As a result, the applications of SQUIDs are wide ranging, from the detection of tiny magnetic fields produced by the human brain and the measurement of fluctuating geomagnetic fields in remote areas to the detection of gravity waves and the observation of spin noise in an ensemble of magnetic nuclei.

SQUIDs combine two physical phenomena, flux quantization, the fact that the flux Φ in a closed superconducting loop is quantized [1] in units of the flux quantum $\Phi_0 \equiv h/2e \cong 2.07 \times 10^{-15}$ Wb, and Josephson tunneling [2]. There are two kinds of SQUIDs. The first [3], the dc SQUID, consists of two Josephson junctions connected in parallel in a superconducting loop, and is so named because it can be operated with a steady current bias. The second [4,5], the rf SQUID, involves a single Josephson junction interrupting the current flow around a superconducting loop, and is operated with a radiofrequency flux bias. In both cases, the output from the SQUID is periodic with period Φ_0 in the magnetic flux applied to the loop. One generally is able to detect an output signal corresponding to a flux change of much less than one flux quantum.

H. Weinstock (ed.), SQUID Sensors: Fundamentals, Fabrication and Applications, 1–62.

In this chapter I give an overview of the current state of the SQUID art. I cannot hope to describe all of the SQUIDs that have been made or, even less, all of the applications in which they have been successfully used. I begin, in Sec. 2, with a brief review of the resistively-shunted Josephson junction, with particular emphasis on the effects of noise. Section 3 contains a description of the dc SQUID: how these devices are made and operated, and the limitations imposed by noise. Section 4 contains a similar description of the properties of rf SQUIDs. In Sec. 5, I describe a selection of instruments based on SQUIDs and mention some of their applications. Section 6 contains a discussion of the present state of the art of high temperature SQUIDs, and Sec. 7 some concluding remarks.

Sections 2-5 are identical to those in the chapter I wrote for an earlier NATO Advanced Study Institute [6], apart from Sec. 3.6 which I have partly rewritten. However, I have substantially rewritten and updated Sec. 6 on high-T_c SQUIDs and magnetometers, the performance of which has improved tremendously in the intervening three years. I have also rewritten Sec. 7.

Some topics I touch on briefly are dealt with in much greater detail by the authors of other chapters in these proceedings. The chapter by Dietmar Drung provides a comprehensive review of alternative readout schemes for dc SQUIDs, and that by Alex Braginski gives an overview of high-T_c thin film fabrication and describes rf SQUIDs and their applications in some detail. I have said nothing about nondestructive evaluation with SQUIDs, which is covered by Gordon Donaldson and John Wikswo, or about gravity gradiometers, which are discussed by Ho Jung Paik. Finally, I have omitted the vast subject of biomagnetism, which is surveyed in great detail by the remaining authors.

2. The Resistively-Shunted Junction

A Josephson junction [2] consists of two superconductors separated by a thin insulating barrier. Cooper pairs of electrons are able to tunnel through the barrier, maintaining phase coherence in the process. The applied current, I, controls the difference $\delta = \phi_1 - \phi_2$ between the phases of the two superconductors according to the current-phase relation

$$I = I_0 \sin \delta, \tag{2.1}$$

where I_0 is the critical current, that is, the maximum supercurrent the junction can sustain. When the current is increased from zero, initially there is no voltage across the junction, but for $I > I_0$ a voltage V appears, and δ evolves with time according to the voltage-frequency relation

$$\dot{\delta} = 2eV/\hbar = 2\pi V/\Phi_0 \; . \tag{2.2}$$

A high quality Josephson tunnel junction has a hysteretic current-voltage (I - V) characteristic. As the current is increased from zero, the voltage switches abruptly to a nonzero value when I exceeds I_0, but returns to zero only when I is reduced to a value much less than I_0. This hysteresis must be eliminated for SQUIDs operated in the conventional manner, and one does so by shunting the junction with an external shunt resistance. The "resistively shunted junction" (RSJ) model [7, 8] is shown in Fig.1(a). The junction has a critical current I_0 and is in parallel with its self-capacitance C and its shunt resistance R, which has a current noise source $I_N(t)$ associated with it. The equation of motion is

$$C\dot{V} + I_0 \sin \delta + V/R = I + I_N(t). \tag{2.3}$$

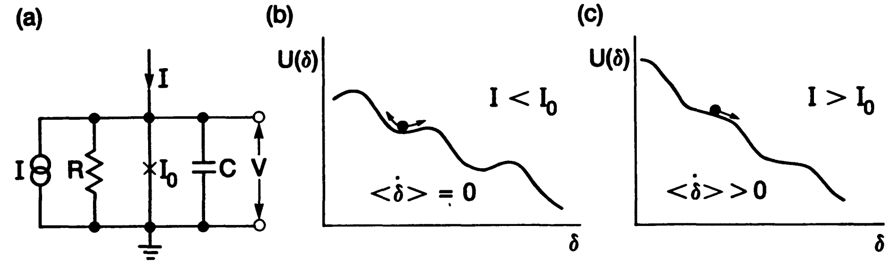

Figure 1. (a) The resistively-shunted Josephson junction; (b) and (c) show the tilted washboard model for $I < I_0$ and $I > I_0$.

Neglecting the noise term for the moment and setting $V = \hbar\dot{\delta}/2e$, we obtain

$$\frac{\hbar C}{2e}\ddot{\delta} + \frac{\hbar}{2eR}\dot{\delta} = I - I_0 \sin\delta = -\frac{2e}{\hbar}\frac{\partial U}{\partial \delta}, \tag{2.4}$$

where

$$U = -\frac{\Phi_0}{2\pi}(I\delta + I_0 \cos\delta). \tag{2.5}$$

One obtains considerable insight into the dynamics of the junction by realizing that Eq. (2.4) also describes the motion of a ball moving on the "tilted washboard" potential U. The term involving C represents the mass of the particle, the 1/R term represents the damping of the motion, and the average "tilt" of the washboard is proportional to -I. For values of $I < I_0$, the particle is confined to one of the potential wells [Fig. 1(b)], where it oscillates back and forth at the plasma frequency [2] $\omega_p = (2\pi I_0/\Phi_0 C)^{1/2}[1-(I/I_0)^2]^{1/4}$. In this state $<\dot{\delta}>$ and hence the average voltage across the junction are zero (< > represents a time average). As the current is increased to I_0, the tilt increases, and when I exceeds I_0, the particle rolls down the washboard; in this state $<\dot{\delta}>$ is nonzero, and a voltage appears across the junction [Fig.1(c)]. As the current is increased further, $<\dot{\delta}>$ increases, as does V. For the nonhysteretic case, as soon as I is reduced below I_0 the particle becomes trapped in one of the wells, and V returns to zero. In this, the overdamped case, we require [7, 8]

$$\beta_c \equiv (2\pi I_0 R/\Phi_0)RC = \omega_J RC \lesssim 1; \tag{2.6}$$

$\omega_J / 2\pi$ is the Josephson frequency corresponding to the voltage $I_0 R$.

We introduce the effects of noise by restoring the noise term in Eq. (2.4) to obtain the Langevin equation

$$\frac{\hbar C}{2e}\ddot{\delta} + \frac{\hbar}{2eR}\dot{\delta} + I_0 \sin\delta = I + I_N(t). \tag{2.7}$$

In the thermal noise limit, the spectral density of $I_N(t)$ is given by the Nyquist formula

$$S_I(f) = 4k_B T/R, \tag{2.8}$$

where f is the frequency. It is evident that $I_N(t)$ causes the tilt in the washboard to fluctuate with time. This fluctuation has two effects on the junction. First, when I is less than I_0 , from time to time fluctuations cause the total current $I + I_N(t)$ to exceed I_0 , enabling the particle to roll out of one potential minimum into the next. For the underdamped junction, this process produces a series of voltage pulses randomly spaced in time. Thus, the time average of the voltage is nonzero even though $I < I_0$, and the I - V characteristic is "noise-rounded" at low voltages. [9] Because this thermal activation process reduces the observed value of the critical current, there is a minimum value of I_0 for which the two sides of the junction remain coupled together. This condition may be written as

$$I_0\Phi_0/2\pi \gtrsim 5k_BT, \tag{2.9}$$

where $I_0\Phi_0 / 2\pi$ is the coupling energy of the junction [2] and the factor of 5 is the result of a computer simulation [10]. For T = 4.2K, we find $I_0 \gtrsim 0.9\mu A$.

The second consequence of thermal fluctuations is voltage noise. In the limit $\beta_c << 1$ and for $I > I_0$, the spectral density of this noise at a measurement frequency f_m that we assume to be much less than the Josephson frequency f_J is given by [11,12]

$$S_V(f_m) = \left[1+\frac{1}{2}\left(\frac{I_0}{I}\right)^2\right]\frac{4k_BTR_d^2}{R} \quad . \quad \left\{\begin{matrix}\beta_c << 1\\ I > I_0\\ f_m << f_J\end{matrix}\right\} \tag{2.10}$$

The first term on the right-hand side of Eq. (2.10) represents the Nyquist noise current generated at the measurement frequency f_m flowing through the dynamic resistance $R_d \equiv dV/dI$ to produce a voltage noise - see Fig. 2. The second term, $(1/2)(I_0 / I)^2 (4k_BT/R) R_d^2$, represents Nyquist noise generated at frequencies $f_J \pm f_m$ mixed down to the

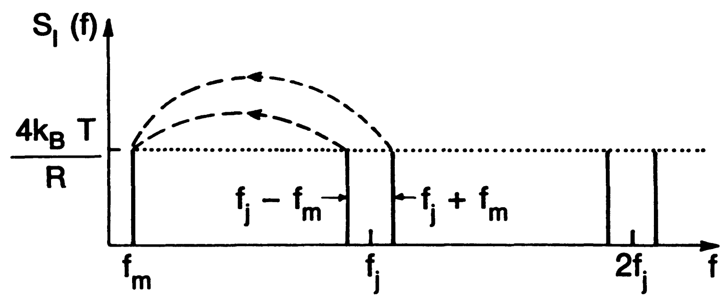

Figure 2. Schematic representation for the noise terms in Eq.(2.10). The Nyquist noise generated in the resistor at frequency f_m contributes directly at f_m; that generated at $f_J \pm f_m$ is mixed down to f_m .

measurement frequency by the Josephson oscillations and the inherent nonlinearity of the junction. The factor $(1/2)(I_0 / I)^2$ is the mixing coefficient, and it vanishes for sufficiently large bias currents. The mixing coefficients for the Nyquist noise generated near harmonics of the Josephson frequencies $2f_J$, $3f_J$, ... are negligible in the limit $f_m / f_J << 1$.

At sufficiently high bias current, the Josephson frequency f_J exceeds k_BT/h, and quantum corrections [13] to Eq. (2.10) become important, provided the term $(1/2)(I_0 / I)^2$ is not too small. The requirement for observing significant quantum corrections is $eI_0 R / k_BT >> 1$. The spectral density of the voltage noise becomes

$$S_V(f_m) = \left[\frac{4k_BT}{R} + \frac{2eV}{R}\left(\frac{I_0}{I}\right)^2 \coth\left(\frac{eV}{k_BT}\right)\right] R_d^2, \qquad \left\{\begin{matrix} \beta_c << 1 \\ I > I_0 \\ f_m << f_J \end{matrix}\right\} \qquad (2.11)$$

where we have assumed that $hf_m / k_BT << 1$, so that the first term on the right-hand side of Eq. (2.11) remains in the thermal limit. In the limit $T \to 0$, the second term, $(2eV/R)(I_0/I)^2 R_d^2$, represents noise mixed down from zero point fluctuations near the Josephson frequency.

This concludes our review of the RSJ, and we now turn our attention to the dc SQUID.

3. The dc SQUID

3.1. A FIRST LOOK

The essence of the dc SQUID [3] is shown in Fig. 3(a). Two junctions are connected in parallel on a superconducting loop of inductance L. Each junction is resistively shunted to eliminate hysteresis on the I -V characteristics, which are shown in Fig. 3(b) for $\Phi = n\Phi_0$ and $(n + 1/2)\Phi_0$, where Φ is the external flux applied to the loop and n is an integer. If we bias the SQUID with a constant current ($> 2 I_0$), the voltage across the SQUID oscillates with period Φ_0 as we steadily increase Φ, as indicated in Fig. 3(c). The SQUID is generally operated on the steep part of the V - Φ curve where the transfer coefficient, $V_\Phi \equiv |(\partial V/\partial \Phi)_I|$, is a maximum. Thus, the SQUID produces an output voltage in response to a small input flux $\delta\Phi$ ($<< \Phi_0$), and is effectively a flux-to-voltage transducer.

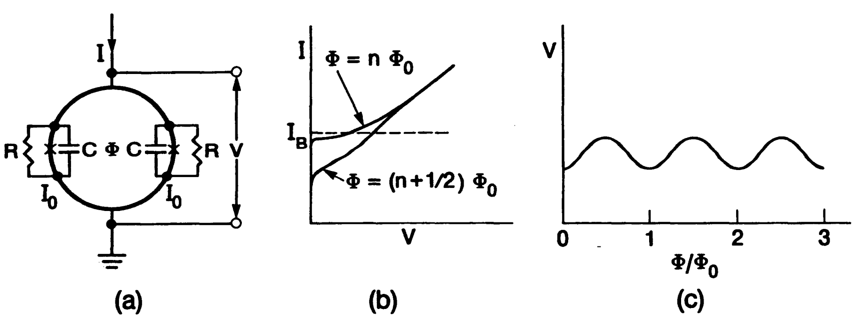

Figure 3. (a) The dc SQUID; (b) I-V characteristics; (c) V vs. Φ/Φ_0 at constant bias current I.

Before we give a detailed description of the signal and noise properties of the SQUID, it may be helpful to give a simplified description that, although not rigorous, gives some insight into the operation of the device. We assume the two junctions are identical and arranged symmetrically on the loop. We further assume, for simplicity, that the bias current is swept from zero to a value above the critical current of the two junctions at a frequency much higher than $d\Phi/\Phi_0 dt$. In the absence of any applied flux (or with $\Phi = n \Phi_0$), there is no current circulating around the loop and the bias current divides equally between the two junctions. The measured critical current is $2I_0$ (if we ignore noise rounding). If we apply a magnetic flux, Φ, the flux in the loop will be quantized and will generate a current $J = -\Phi / L$, where we have neglected the effects of the two junctions [Figs. 4(a) and (b)]. The circulating current adds to the bias current flowing through junction 1 in Fig. 4(a) and subtracts from that flowing through junction 2. In this naive picture, the critical current of junction 1 is reached when $I/2 + J = I_0$, at which point the current flowing through junction 2 is $I_0 - 2J$. Thus, the SQUID switches to the voltage state when $I = 2I_0 - 2J$. As Φ is increased to $\Phi_0 / 2$, J increases to $\Phi_0 / 2L$ [Fig. 4(b)], and the critical current falls to $2I_0 - \Phi_0 / L$ [Fig. 4(c)]. As the flux is increased beyond $\Phi_0 / 2$, however, the SQUID makes a transition from the flux state $n = 0$ to $n = 1$, and J changes sign [Fig. 4(b)]. As we increase Φ to Φ_0, J is reduced to zero and the critical current is restored to its maximum value $I_m = 2I_0$[Fig. 4(c)].

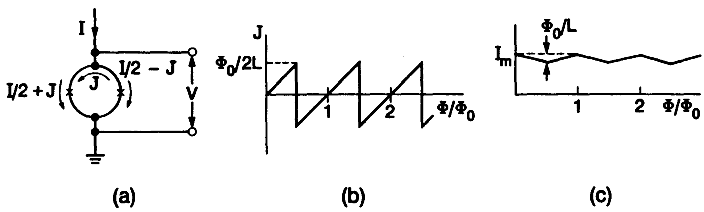

Figure 4. Simplistic view of the dc SQUID: (a) a magnetic flux Φ generates a circulating current J that is periodic in Φ as shown in (b); as a result (c), the maximum supercurrent I_m is also periodic in Φ.

In this way the critical current oscillates as a function of Φ.

Continuing with our simplified model, we see that the voltage change across the SQUID (at the peak of the current sweep) as we change Φ from 0 to $\Phi_0 / 2$ is $\Delta V = (\Phi_0 / L)R/2$, where R/2 is the parallel resistance of the two shunts. Hence, $V_\Phi = \Delta V / (\Phi_0 / 2) = R / L$.

We also can estimate the equivalent flux noise of the SQUID. If the noise voltage across the SQUID is $V_N(t)$ with a spectral density $S_V(f)$, the corresponding flux noise referred to the SQUID loop is just

$$S_\Phi(f) = S_V(f)/ V_\Phi^2 \ . \tag{3.1}$$

A convenient way of characterizing the flux noise is in terms of the noise energy per unit bandwidth,

$$\varepsilon(f) = S_\Phi(f) / 2L. \tag{3.2}$$

If we assume that the noise in the SQUID is just the Nyquist noise in the shunt resistors with spectral density $4k_BT\,(R/2)$, we find $\varepsilon(f) = k_BTL/R$. Although these results are not quantitatively correct, they do give the correct scaling with the various parameters. For example, we see that to lower $\varepsilon(f)$ we should reduce T and L while using the largest possible value of R subject to the I - V characteristic remaining nonhysteretic.

Exact results for the signal and noise can be obtained only from computer simulation. The results show that the plots of the circulating supercurrent and the critical current vs. Φ become smoothed. Furthermore, the noise voltage is higher than Nyquist noise because of mixed-down noise; unfortunately the magnitude of this noise cannot be obtained analytically.

One final remark is appropriate at this point. To observe quantum interference effects, we require the modulation depth of the critical current, Φ_0 / L, to be much greater than the root mean square noise current in the loop, $\langle I_N^2 \rangle^{1/2} = (k_BT / L)^{1/2}$. We shall return to this issue in Sec. 6 in the context of high-T_c SQUIDs.

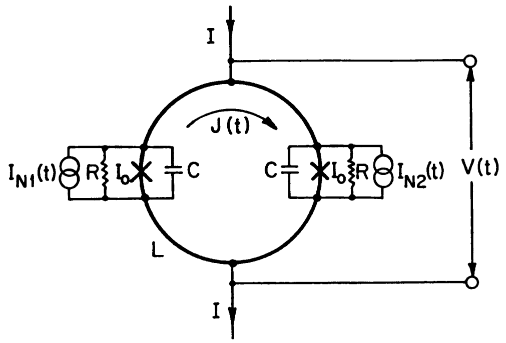

Figure 5. Model of dc SQUID showing noise sources associated with the shunt resistors.

3.2. THERMAL NOISE IN THE SQUID : THEORY

A model for noise calculations is shown in Fig. 5. This figure shows two independent Nyquist noise currents, $I_{N1}(t)$ and $I_{N2}(t)$, associated with the two shunt resistors. The phase differences across the junctions, $\delta_1(t)$ and $\delta_2(t)$, obey the following equations: [14-16]

$$V = \frac{\hbar}{4e}\left(\dot{\delta}_1 + \dot{\delta}_2\right), \tag{3.3}$$

$$J = \frac{\Phi_0}{2\pi L}\left(\delta_1 - \delta_2 - \frac{2\pi\Phi}{\Phi_0}\right), \tag{3.4}$$

$$\frac{\hbar C}{2e}\ddot{\delta}_1 + \frac{\hbar}{2eR}\dot{\delta}_1 = \frac{I}{2} - J - I_0 \sin\delta_1 + I_{N1}, \tag{3.5}$$

and

$$\frac{\hbar C}{2e}\ddot{\delta}_2 + \frac{\hbar}{2eR}\dot{\delta}_2 = \frac{I}{2} + J - I_0 \sin\delta_2 + I_{N2}. \tag{3.6}$$

Equation (3.3) relates the voltage to the average rate of change of phase; Eq. (3.4) relates the current in the loop, J, to $\delta_1 - \delta_2$ and to Φ; and Eqs. (3.5) and (3.6) are Langevin equations coupled via J. These equations have been solved numerically for a limited range of values of the noise parameter $\Gamma = 2\pi k_B T / I_0 \Phi_0$, reduced inductance $\beta = 2 L I_0 / \Phi_0$ and hysteresis parameter β_c. For typical SQUIDs in the ^{4}He temperature range, $\Gamma = 0.05$. One computes the time-averaged voltage V vs. Φ, and hence finds V_Φ, which, for a given value of Φ, peaks smoothly as a function of bias current. The transfer function exhibits a shallow maximum around $(2n + 1)\,\Phi_0 / 4$. One computes the noise voltage for a given value of Φ as a function of I, and finds that the spectral density is white at frequencies much less than the Josephson frequency. For each value of Φ, the noise voltage peaks smoothly at the value of I where V_Φ is a maximum. From these simulations, one finds that the noise energy has a minimum when $\beta \approx 1$. For $\beta = 1$, $\Gamma = 0.05$, $\Phi = (2n + 1)\,\Phi_0 / 4$ and for the value of I at which V_Φ is a maximum, the results can be summarized as follows:

$$V_\Phi \approx R/L, \tag{3.7}$$

$$S_V(f) \approx 16k_BTR, \tag{3.8}$$

and

$$\varepsilon(f) \approx 9k_BTL/R. \tag{3.9}$$

We see that our rough estimate of V_Φ in Sec. 3.1 was rather accurate, but that the assumption that the noise spectral density was given by the Nyquist result underestimated the computed value by a factor of about 8.

It is often convenient to eliminate R from Eq. (3.9) using the expression $R = (\beta_c \Phi_0 / 2\pi I_0 C)^{1/2}$. We find

$$\varepsilon(f) \approx 16\, k_BT(LC/\beta_c)^{1/2}. \quad (\beta_c \lesssim 1) \tag{3.10}$$

Equation (3.10) gives a clear prescription for improving the resolution: one should reduce T, L and C. A large number of SQUIDs with a wide range of parameters have been tested and found to have white noise energies generally in good agreement with the predicted values. It is common practice to quote the noise energy of SQUIDs in units of $\hbar$ ($\approx 10^{-34}$J sec $= 10^{-34}$JHz^{-1}).

In closing this discussion, we emphasize that although $\varepsilon(f)$ is a useful parameter for characterizing the resolution of SQUIDs with different inductances, it is not a complete specification because it does not account fully for the effects of current noise in the SQUID loop. We defer a discussion of this point to Sec. 5.4.

3.3. PRACTICAL DC SQUIDS

Modern dc SQUIDs are invariably made from thin films with the aid of either photolithography or electron-beam lithography. A major concern in the design is the need to couple an input coil inductively to the SQUID with rather high efficiency. This problem was elegantly solved by Ketchen and Jaycox, [17, 18] who introduced the idea of depositing a spiral input coil on a SQUID in a square washer configuration. The coil is separated from the SQUID with an insulating layer (Fig. 6). Figure 7 shows a typical example [19] of one of these designs, involving trilayer Nb/Al-Al_2O_3/Nb junctions [20]. The SQUIDs are made in batches of 400 on oxidized, 100 mm-diameter silicon wafers. After the Nb base electrode and a thin Al layer have been sputtered, the Al is oxidized in a reduced pressure of O_2 and the Nb counterelectrode is then deposited. The entire trilayer is formed without removing the wafers from the controlled atmosphere of the sputter system. One defines the junction areas by anodizing a small ring of the counterelectrode, and the base electrode is etched to form the SQUID washer. In subsequent operations one adds the Nb layer that forms the input and flux modulation coils and makes the connection to the counterelectrode, the shunt resistors (Mo or Pb), and the final Nb layer that makes the connection to the innermost turn of the input coil. The insulation between each layer is SiO_2, formed by plasma-enhanced chemical vapor deposition (PECVD). All patterning is performed with reactive ion etching. The estimated SQUID inductance is L = 0.29 nH and the measured shunt resistance R = 4.0 Ω.

Design guidelines for square washer SQUIDs have been given by Jaycox and Ketchen [18], who showed that a square washer (with no slit) with inner and outer edges d and w has an inductance L (loop) = $1.25\mu_0 d$ in the limit w >> d. They gave the following expressions for the inductances of the SQUID, L, and of the spiral coil, L_i, and for the mutual inductance, M_i, and coupling coefficient, α^2, between the spiral coil and the SQUID:

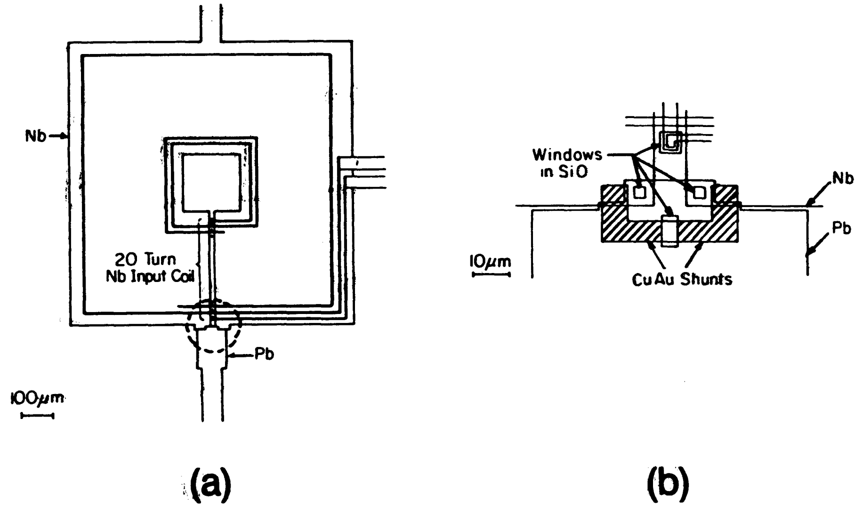

Figure 6. (a) Configuration of planar dc SQUID with overlaid spiral input coil; (b) expanded view of junctions and shunts.

$$L = L\,(\text{loop}) + L_j, \tag{3.11}$$

$$L_i = n^2\,(L-L_j) + L_s, \tag{3.12}$$

$$M_i = n(L-L_j) \tag{3.13}$$

and

$$\alpha^2 = (1-L_j\,/\,L)\,/\,[1+L_s\,/\,n^2(L-L_j)]. \tag{3.14}$$

Here, L_j is the parasitic inductance associated with the junctions (and possibly with the slit), n is the number of turns of the input coil and L_s is the stripline inductance of this coil, which is generally much smaller than L_i for $n \gtrsim 20$. Measured parameters are generally in good agreement with these predictions.

References [21-28] are a selection of papers describing SQUIDs fabricated on the basis of the Ketchen-Jaycox design. Some of the devices involve edge junctions in which the counter-electrode is a strip making a tunneling contact to the base electrode only at the edge. This technique enables one to make junctions with a small area and thus a small self-capacitance without resorting to electron-beam lithography. However, stray capacitances are often critically important. As has been emphasized by a number of authors, parasitic capacitance between the square washer and the input coil can produce resonances that, in turn, induce structure on the I-V characteristics and give rise to excess noise. Knuutila *et al.* [27] successfully damped the resonances in the input coil by terminating the stripline with a matched resistor. In an alternative scheme, Foglietti *et al.* [25] introduced additional damping across the two Junctions in series by depositing a thin-film resistor across the slit in the square washer. Other approaches have been devised to reduce the parasitic capacitance. For example, Muhlfelder *et al.* [26] coupled the SQUID to the signal source via an intermediate superconducting transformer, thereby reducing the number of turns on the SQUID

(a)

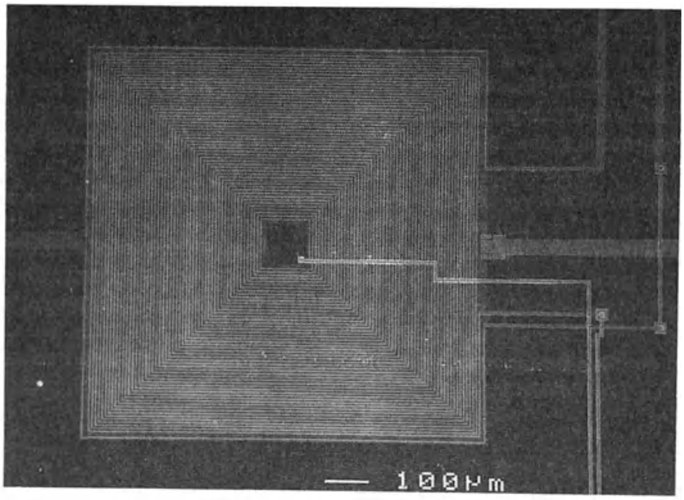

(b)

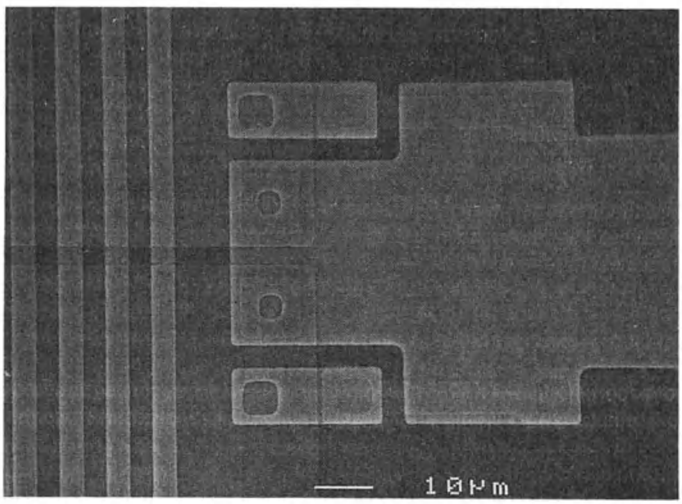

Figure 7. (a) Electron micrograph of planar dc SQUID with 53-turn input coil; the modulation and feedback coil consists of a single-turn outside the input coil. (b) Electron micrograph showing junctions on either side of the slit in the square washer. (Courtesy A. Barfknecht, M. S. Colclough and A. de la Cruz, Conductus, Inc. [19].)

washer; Carelli and Foglietti [29] fabricated "fractional turn SQUIDs" with many loops in parallel that are coupled to a thin-film input coil surrounding them.

Most SQUIDs are patterned with conventional photolithographic techniques which yield linewidths of 2-3μm. Recently, however, Ketchen *et al.* [30] fabricated devices in which the input coils had linewidths of 0.5μm. The inductances of these designs were in good agreement with predicted values. Ultimately, one expects a new generation of SQUIDs with submicron features and a corresponding reduction in the noise energy.

3.4 FLUX-LOCKED LOOP

In most, although not all, practical applications one uses the SQUID in a feedback circuit as a null detector of magnetic flux [31]. One applies a modulating flux to the SQUID with a peak-to-peak amplitude $\Phi_0/2$ and a frequency f_m usually between 100 and 500kHz, as indicated in Fig. 8. If the quasistatic flux in the SQUID is exactly $n\Phi_0$ the resulting voltage is a rectified version of the input signal, that is, it contains only the frequency $2f_m$ [Fig. 8(a)]. If this voltage is sent through a lock-in detector referenced to the fundamental frequency f_m, the output will be zero. On the other hand, if the quasistatic flux is $(n + 1/4)\Phi_0$, the voltage across the SQUID is at frequency f_m [Fig. 8(b)], and the output from the lock-in will be a maximum. Thus, as one increases the flux from $n\Phi_0$ to $(n + 1/4)\Phi_0$, the output from the lock-in will increase steadily; if one reduces the flux from $n\Phi_0$ to $(n - 1/4)\Phi_0$, the output will increase in the negative direction [Fig. 8(c)].

The alternating voltage across the SQUID is coupled to a low-noise preamplifier, usually at room temperature, via either a cooled transformer [32] or a cooled LC series-resonant circuit [31]. The first of these options presents an impedance N^2R_d to the preamplifier, and

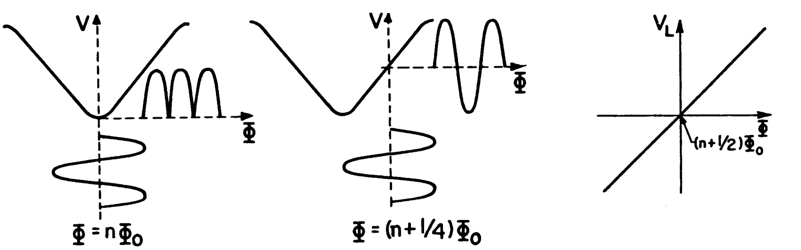

Figure 8 Flux modulation scheme showing voltage across the SQUID for (a) $\Phi = n\Phi_0$ and (b) $\Phi = (n+1/4)\Phi_0$. The output V_L from the lock-in detector vs. Φ is shown in (c).

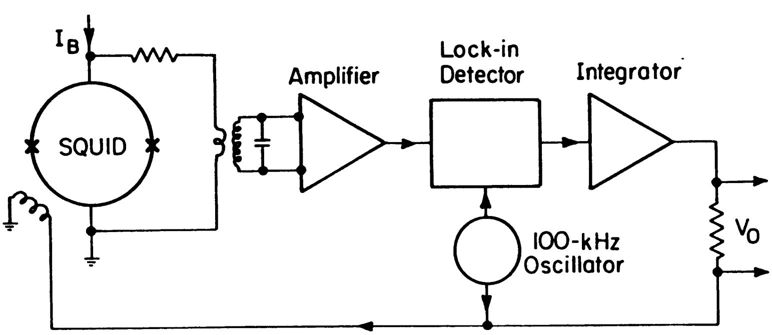

Figure 9. Modulation and feedback circuit for the dc SQUID.

the second an impedance Q^2R_d, where R_d is the dynamic resistance of the SQUID at the bias point, N is the turns ratio of the transformer, and Q is the quality factor of the tank circuit. The value of N or Q is chosen to optimize the noise temperature of the preamplifier; with careful design, the noise from the amplifier can be appreciably less than that from the SQUID at 4.2 K.

Figure 9 shows a typical flux-locked loop in which the SQUID is coupled to the preamplifier via a cooled transformer. An oscillator applies a modulating flux to the SQUID. After amplification, the signal from the SQUID is synchronously detected and sent through an integrating circuit. The smoothed output is connected to the modulation and feedback coil via a large series resistor R_f. Thus, if one applies a flux $\delta\Phi$ to the SQUID, the feedback circuit will generate an opposing flux $-\delta\Phi$, and a voltage proportional to $\delta\Phi$ appears across R_f. This technique enables one to measure changes in flux ranging from much less than a single flux quantum to many flux quanta. The use of a modulating flux eliminates 1/f noise and drift in the bias current and preamplifier. Using a modulation frequency of 500kHz, a double transformer between the SQUID and the preamplifier, and a two-pole integrator, Wellstood *et al.* [28] achieved a dynamic range of $\pm$ 2 x 10^7 $Hz^{1/2}$ for signal frequencies up to 6 kHz, a frequency response from 0 to 70kHz ($\pm$3 dB), and a maximum slew rate of 3 x 10^6 Φ_0 sec^{-1}.

3.5 THERMAL NOISE IN THE DC SQUID : EXPERIMENT

One determines the spectral density of the equivalent flux noise in the SQUID by connecting a spectrum analyzer to the output of the flux-locked loop. A representative power spectrum [33] is shown in Fig. 10: above a 1/f noise region, the noise is white at frequencies up to the roll-off of the feedback circuit. In this particular example, with L = 200pH and R = 8Ω, the measured flux noise was $S_\Phi^{1/2} = (1.9 \pm 0.1) \times 10^{-6}\Phi_0 Hz^{-1/2}$, in reasonable agreement with the predictions of Eqs. (3.7) and (3.8). The corresponding flux-noise energy was 4 x 10^{-32} $JHz^1 \approx 400\,\hbar$. Many groups have achieved noise energies that are comparable or, with lower values of L or C, somewhat better.

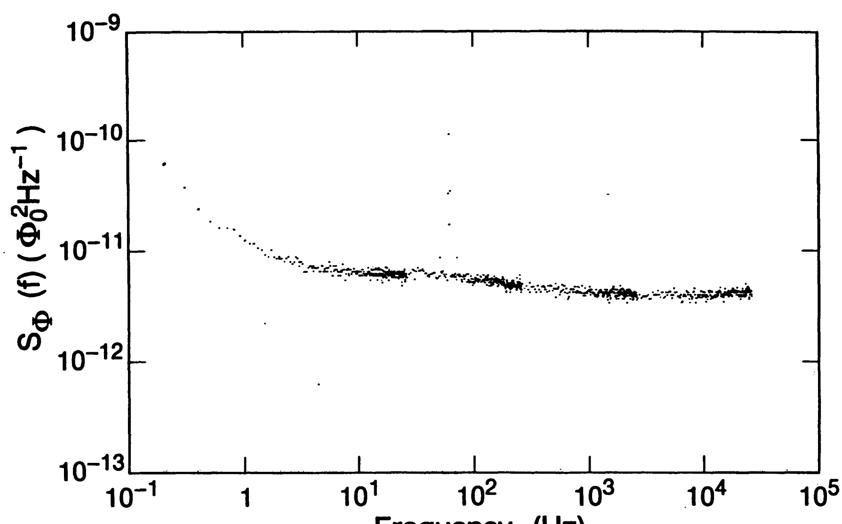

Figure 10. Spectral density of equivalent flux noise for dc SQUID: L = 0.2nH, R = 8Ω, and T = 4.2K. (Courtesy F.C. Wellstood [33])

To investigate the temperature dependence of their SQUIDs, Wellstood *et al.* [34] cooled them in a dilution refrigerator to temperatures below 1K , and used a second dc SQUID as a preamplifier. They found that the noise energy scaled accurately with T at temperatures down to about 150mK, below which the noise energy became nearly constant. This saturation was traced to heating in the resistive shunts, which prevented them from cooling much below 150mK. This heating is actually a hot-electron effect: the bottleneck in the cooling process is the rate at which the electrons can transfer energy to the phonons which, in turn, transfer energy to the substrate [35, 36]. The temperature of the shunts was lowered by connecting each of them to a CuAu "cooling fin" of large volume. The hot electrons diffuse into the fins where they rapidly transfer energy to other electrons. Since the "reaction volume" is now greatly increased, the numbers of electrons and phonons interacting are also increased, and the electron gas is cooled more effectively. In this way, the effective electron temperature was reduced to about 50mK when the SQUID was at a bath temperature of 20mK, with a concomitant reduction in ε to about $5\hbar$. Subsequently, Ketchen *et al.* [37] have achieved a noise energy of about $3\hbar$ at 0.3 K in a SQUID with L = 100 pH and C = 0.14 pF.

3.6 1/f NOISE IN DC SQUIDS

The white noise in dc SQUIDs is well understood. However, some applications of SQUIDs, for example neuromagnetism, require good resolution at frequencies down to 0.1 Hz or less, and the level of the 1/f or "flicker" noise becomes very important.

There are at least two separate sources of 1/f noise in the dc SQUID [38]. The first arises from 1/f fluctuations in the critical current of the Josephson junctions, and the mechanism for this process is reasonably well understood [39]. In the process of tunneling through the barrier, an electron becomes trapped on a defect in the barrier and is subsequently released. While the trap is occupied, there is a local change in the height of the tunnel barrier and hence in the critical current density of that region. As a result, the presence of a single trap causes the critical current of the junction to switch randomly back and forth between two values, producing a random telegraph signal. If the mean time between pulses is τ, the spectral density of this process is a Lorentzian,

$$S(f) \propto \frac{\tau}{1+(2\pi f\tau)^2}, \tag{3.15}$$

namely white at low frequencies and falling off as $1/f^2$ at frequencies above $1/2\pi\tau$. In many cases, the trapping process is thermally activated, and τ is of the form

$$\tau = \tau_0 \exp(E/k_BT), \tag{3.16}$$

where τ_0 is a constant and E is the barrier height.

In general, there may be several traps in the junction, each with its own characteristic time τ_i. One can superimpose the trapping processes, assuming them to be statistically independent, to obtain a spectral density [40]

$$S(f) \propto \int dE\ D(E)\left[\frac{\tau_0 \exp(E/k_BT)}{1+(2\pi f\tau_0)^2\exp(2E/k_BT)}\right], \tag{3.17}$$

where D(E) is the distribution of activation energies. The term in square brackets is a strongly peaked function of E, centered at $\tilde{E} \equiv k_BT\ln(1/2\pi f\tau_0)$, with a width $\sim k_BT$. Thus, at a given temperature, only traps with energies within a range k_BT of $\tilde{E}$ contribute significantly to the noise. If one now assumes D(E) is broad with respect to k_BT, one can take $D(\tilde{E})$ outside the integral, and carry out the integral to obtain

$$S(f,T) \propto \frac{k_BT}{f} D(\tilde{E}). \quad (3.18)$$

In fact, one obtains a l/f-like spectrum from just a few traps.

The magnitude of the l/f noise in the critical current depends strongly on the quality of the junction as measured by the current leakage at voltages below $(\Delta_1 + \Delta_2)/e$, where Δ_1 and Δ_2 are the energy gaps of the two superconductors. Traps in the barrier enable electrons to tunnel in this voltage range, a process producing both leakage current and l/f noise. Thus, for a given technology, junctions with low subgap leakage currents will have low l/f noise. Figure 11 shows an example of a Nb-Al_2O_3-Nb junction with a single trap [41]. The junction was resistively shunted and voltage biased at typically 1.5 μV; the noise currents were measured with a SQUID. At 4.2 K [Fig.11(a)], the noise is approximately Lorentzian; the switching process producing the noise is shown in the inset. Figure 11(b) shows that at 1.5 K the noise is substantially reduced as the trap freezes out. By measuring the temperature dependence of the random telegraph signal, Savo *et al.* [41] found that τ obeyed Eq. (3.16) with τ_0 = 10 s and E = 1.8 meV. Furthermore, τ was exponentially distributed, as expected,

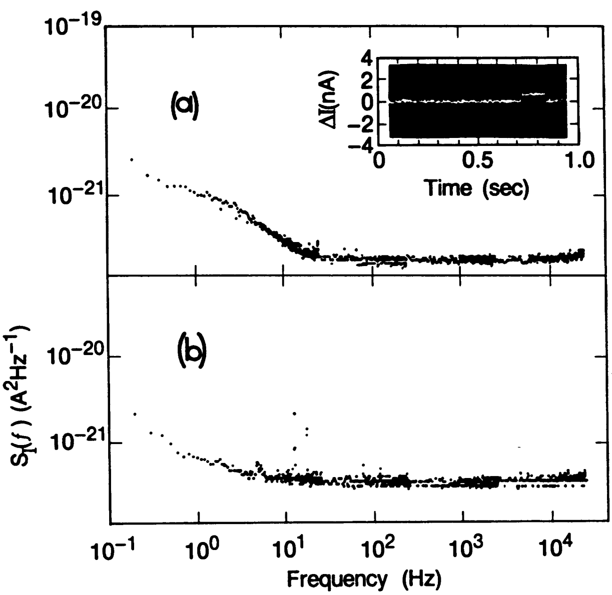

Figure 11. Spectral density of fluctuations in the critical current of a single Nb-Al_2O_3-Nb tunnel junction at (a) 4.2K and (b) 1.5K. Inset in (a) shows fluctuations vs. time (from ref. 41).

with an average value of 107 ms at 4.2 K.

The second source of l/f noise in SQUIDs arises from the motion of flux lines trapped in the body of the SQUID [38]. This mechanism manifests itself as a flux noise; for all practical purposes the noise source behaves as if an external flux noise were applied to the SQUID. Thus, the spectral density of the l/f flux noise scales as V_Φ^2, and, in particular, vanishes at $\Phi = (n \pm 1/2)\Phi_0$ where $V_\Phi = 0$. By contrast, critical current noise is still present when $V_\Phi = 0$, although its magnitude does depend on the applied flux.

The level of 1/f flux noise appears to depend strongly on the microstructure of the thin films. For example, SQUIDs fabricated at Berkeley with Nb loops sputtered under a particular set of conditions show 1/f flux noise levels of typically [38] $10^{-10}\,\Phi_0^2\,Hz^{-1}$ at 1 Hz. On the other hand, SQUIDs with Pb loops in exactly the same geometry exhibited a 1/f noise level of about $2 \times 10^{-12}\,\Phi_0^2 Hz^{-1}$ at 1 Hz, arising from critical current fluctuations. Tesche *et al.* [42] reported a 1/f noise level in Nb-based SQUIDs of about $3 \times 10^{-13}\,\Phi_0^2\,Hz^{-1}$, while Foglietti *et al.* [43] found a critical current 1/f noise corresponding to $2 \times 10^{-12}\,\Phi_0^2\,Hz^{-1}$, also in Nb-based devices. Thus, we conclude that the quality of the Nb films plays a significant role in the level of 1/f flux noise. It is of considerable fundamental and practical interest to understand the mechanism in detail.

There is an important practical difference between the two sources of 1/f noise: critical current noise can be reduced by a suitable modulation scheme, whereas flux noise cannot. To understand how to reduce critical current 1/f noise, we first note that at constant current bias the spectral density of the 1/f voltage noise across the SQUID can be written in the approximate form

$$S_V(f) \approx \frac{1}{2}\left[(\partial V/\partial I_0)^2 + L^2 V_\Phi^2\right] S_{I_0}(f). \tag{3.19}$$

In Eq. (3.19), we have assumed that each junction has the same level of critical current noise, with a spectral density $S_{I_0}(f)$. The first term on the right is the "in-phase mode", in which each of the two junctions produces a fluctuation of the same polarity. This noise is eliminated (ideally) by the conventional flux modulation scheme described in Sec. 3.4, provided the modulation frequency is much higher than the 1/f noise frequency. The second term on the right of Eq. (3.19) is the "out-of phase" mode in which the two fluctuations are of opposite polarity and, roughly speaking, result in a current around the SQUID loop. This term appears, therefore, as a flux noise, vanishing for $V_\Phi = 0$, but is not reduced by the usual flux modulation scheme. Fortunately, there are schemes by which this second term, as well as the first, can be reduced. These include the bias reversal scheme introduced by Koch *et al.* [38], which is similar to that available on the dc SQUID system manufactured by BTi [44]. An alternative scheme, second harmonic detection (SHAD), was developed by Foglietti *et al.* [43].

We briefly describe the scheme of Koch *et al.* [38]; the principle is illustrated in Fig. 12 and the practical implementation in Fig. 13. The SQUID is flux-modulated with a 100 kHz square wave of peak-to-peak amplitude $\Phi_m = \Phi_0/2$. Synchronously with the modulation the bias current I through the SQUID is reversed, typically at a frequency $f_r = 3.125$ kHz. The resistance bridge shown in Fig. 13 minimizes the 3.125 kHz switching transients across the transformer. Simultaneously with the bias reversal a flux $\Phi/2$ is applied to the SQUID. In Figs. 12(a) and (b) we see that the bias reversal changes the sign of the voltage across the SQUID while the flux shift ensures that the sign of the flux-to-voltage transfer function remains the same. The transformer coupling the SQUID to the preamplifier is often tuned at the modulation frequency with a Q of about 3, so that any 100 kHz signals at the secondary are approximately sinusoidal.

We assume that the SQUID is operated in the usual flux-locked loop, with the output from the lock-in detector integrated and fed back to the SQUID (Fig. 13). Thus, the 100 kHz signal across the SQUID consists of just the tiny error signal. Suppose now that we apply a small external flux $\delta\Phi$ to the SQUID at a frequency well below f_r. The V-Φ curves are shifted as in Figs. 12(a), and the 100 kHz flux modulation switches the SQUID between the points 1 and 2 for positive bias and 3 and 4 for negative bias. As a function of time, the voltage V across the SQUID is as shown in Fig. 12, and the signal across the tuned transformer V_t is at the fundamental frequency. When this signal is mixed with the reference

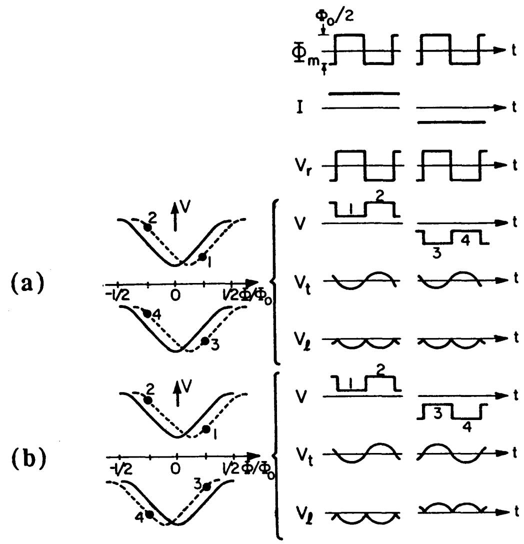

Figure 12. Principle of bias reversal scheme to reduce 1/f noise due to out-of-phase critical current fluctuations. The left-hand column shows the V-Φ curves (solid lines), and the dashed lines indicate the effect of (a) an external flux change $\delta\Phi$ and (b) a flux change generated by out-of-phase critical current fluctuations. The right-hand column shows, as a function of time t, (top to bottom) the flux modulation Φ_m, the bias current I, and the reference voltage V_r used to lock-in detect the signal from the SQUID; the next three rows are for an external flux change $\delta\Phi$, and show the voltage V across the SQUID, the voltage V_t across the secondary of the tuned transformer and the output V_ℓ of the lock-in detector; the last three rows show the same voltages for an out-of-phase critical current fluctuation.

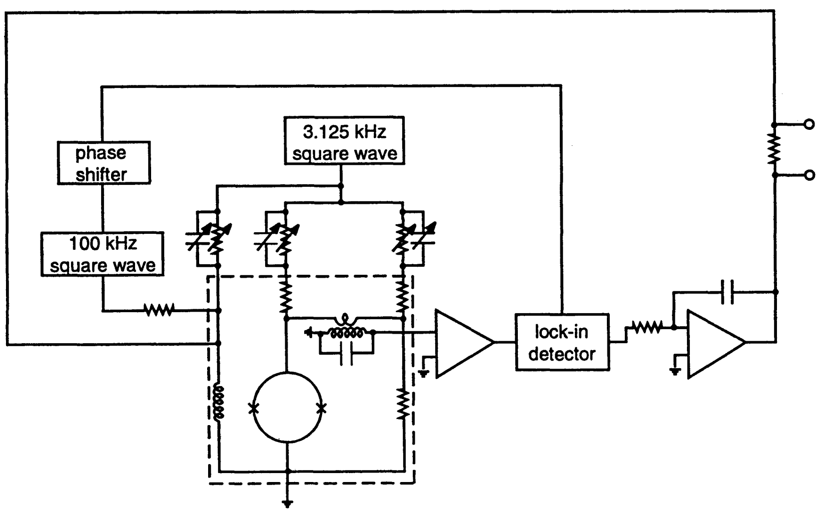

Figure 13. Schematic for flux-locked loop with bias current reversal. Cryogenic components are enclosed in the dashed box.

voltage V_r, the output from the lock-in detector V_ℓ will consist of a series of negative-going peaks for both polarities of the bias current. The average of this output produces a negative signal proportional to $\delta\Phi$ which is then used to cancel the flux applied to the SQUID. Thus, in the presence of bias reversal and flux shift, the SQUID responds to an applied flux in the usual way.

We consider now the effects of 1/f noise on the critical currents. The in-phase mode is eliminated by the 100kHz flux modulation as in Sec. 3.4. Suppose, instead, we have an out-of-phase critical current fluctuation at a frequency below f_r. Because the flux generated by this fluctuation *changes sign* when the bias current is reversed, the V-Φ curves are displaced in opposite directions. As a result, the voltage across the SQUID undergoes a phase change of π when the bias current is reversed, as shown in Fig. 12. Consequently, the voltage at the output of the lock-in due to the out-of-phase critical current fluctuation changes sign each time the bias current is reversed, and the time average of the signal over periods much longer than $1/f_r$ is zero. Thus, the 1/f noise due to both in-phase and out-of-phase critical current fluctuations is eliminated by this scheme.

As we shall see in Sec. 6, the 1/f noise in the critical current of high-T_c SQUIDs is severe, and it is essential to use a suitable noise reduction scheme for low-frequency applications. As stressed before, no bias reversal scheme can remove the 1/f noise due to the motion of flux.

3.7 ALTERNATIVE READ-OUT SCHEMES

Although the flux modulation method described in Sec. 3.4 has been used successfully for many years, a number of alternate schemes recently have been developed. These efforts have been motivated, at least in part, by the need to simplify the electronics required for the multichannel systems used in neuromagnetism - see Sec. 5.1. Fujimaki and co-workers [45] and Drung and co-workers [46] have devised schemes in which the output from the SQUID is sensed digitally and fed back as an analog signal to the SQUID to flux-lock the loop. Fujimaki *et al.* [45] used Josephson digital circuitry to integrate their feedback system on the same chip as the SQUID so that the flux-locked signal was available directly from the cryostat. The system of Drung and co-workers, however, is currently the more sensitive, with a flux resolution of about $10^{-6}\,\Phi_0\mathrm{Hz}^{-1/2}$ in a 50 pH SQUID. These workers also were able to reduce the 1/f noise in the system using a modified version of the modulation scheme of Foglietti *et al.* [43]. Although they need further development, cryogenic digital feedback schemes offer several advantages: they are compact, produce a digitized output for transmission to room temperature, offer wide flux-locked bandwidths, and need not add any noise to the intrinsic noise of the SQUID.

In a quite different approach, Mück and Heiden [47] have operated a dc SQUID with hysteretic junctions in a relaxation oscillator. The oscillation frequency depends on the flux in the SQUID, reaching a maximum at $(n+1/2)\Phi_0$ and a minimum at $n\Phi_0$. A typical frequency modulation is 100kHz at an operating frequency of 10 MHz. This technique produces large voltages across the SQUID so that no matching network to the room temperature electronics is required. The room temperature electronics is simple and compact, and the resolution at 4.2 K is about $10^{-5}\Phi_0\mathrm{Hz}^{-1/2}$ with an inductance estimated to be about 80pH.

More recently, Drung [48] introduced the concept of additional positive feedback (APF). In this technique, the SQUID is shunted with a small resistor in series with an inductance that is magnetically coupled to the SQUID. When the flux applied to the SQUID is changed, there is a re-distribution of the current between the SQUID and the parallel shunt, and the inductance links an additional flux to the SQUID. This feedback is positive or negative, depending on the sign of V_Φ. The voltage across the shunted SQUID is connected directly to a low-noise preamplifier. After additional stages of amplification and integration, the signal is fed back to another coil coupled to the SQUID to flux-lock the SQUID in the usual way; the phase of the feedback is chosen to ensure that the additional feedback is positive. APF enhances V_Φ by an order of magnitude or more, boosting its value to the point at which the preamplifier noise is comparable with or less than the intrinsic SQUID noise. This technique eliminates the need for a coupling network between the SQUID and the preamplifier, and allows for a rather simple, direct-coupled feedback circuit.

In yet another novel approach, Seppä [49] has used adaptive noise cancellation to reduce the preamplifier noise, again allowing one to couple the SQUID directly to the room temperature preamplifier without sacrificing noise performance. In this mode of operation, the SQUID is voltage biased and coupled to an inductor connected across it. The voltage noise of the preamplifier induces a current noise in the inductor and thus a flux noise in the SQUID. The phase of the feedback is such that the voltage noise generated across the SQUID cancels the preamplifier voltage noise.

4 The rf SQUID

4.1 PRINCIPLES OF OPERATION

The rf SQUID has continued to be widely used because of its long-standing commercial availability, but for many years had seen very little development. Recently, however, there has been an upsurge of interest in rf SQUIDs, spurred in part by the advent of high-T_c superconductivity. After a rather brief account of the principles and noise limitations, following rather closely descriptions in earlier reviews [50, 51], I shall describe one of these recent advances.

The rf SQUID [4, 5] shown in Fig. 14 consists of a superconducting loop of inductance L interrupted by a single Josephson junction with critical current I_0 and a nonhysteretic current-voltage characteristic. Flux quantization [1] imposes the constraint

$$\delta + 2\pi\Phi_T/\Phi_0 = 2\pi n \tag{4.1}$$

on the total flux Φ_T threading the loop. The phase difference δ across the junction determines the supercurrent

$$I_s = -I_0 \sin (2\pi\Phi_T/\Phi_0) \tag{4.2}$$

flowing in the ring. A quasistatic external flux Φ thus gives rise to a total flux

$$\Phi_T = \Phi - LI_0 \sin (2\pi\Phi_T/\Phi_0). \tag{4.3}$$

The variation of Φ_T with Φ is sketched in Fig. 15(a) for the typical value $LI_0 = 1.25\ \Phi_0$. The regions with positive slope are stable, whereas those with negative slope are not. A "linearized" version of Fig. 15(a) showing the path traced out by Φ and Φ_T is shown in Fig. 15(b). Suppose we slowly increase Φ from zero. The total flux Φ_T increases less rapidly than Φ because the response flux $-LI_s$ opposes Φ. When I_s reaches I_0, at an applied flux Φ_c and a total flux Φ_{Tc}, the junction switches momentarily into a nonzero voltage state and the SQUID jumps from the k = 0 to the k = 1 quantum state. If we subsequently reduce Φ from a value just above Φ_c, the SQUID remains in the k = 1 state until $\Phi = \Phi_0 - \Phi_c$, at which point I_s again exceeds the critical current and the SQUID returns to the k = 0 state. In the same way, if we lower Φ to below $-\Phi_c$ and then increase it, a second hysteresis loop will be traced. We note that this hysteresis occurs provided $LI_0 > \Phi_0/2\pi$; most practical SQUIDs are operated in this regime. For $LI_0 \approx \Phi_0$, the energy ΔE dissipated when one takes the flux around a single hysteresis loop is its area divided by L :

$$\Delta E \approx I_0\Phi_0. \tag{4.4}$$

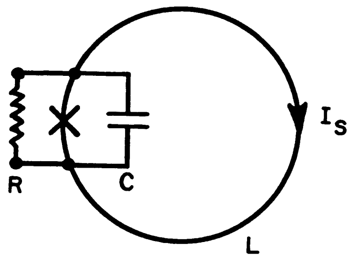

Figure 14. The rf SQUID.

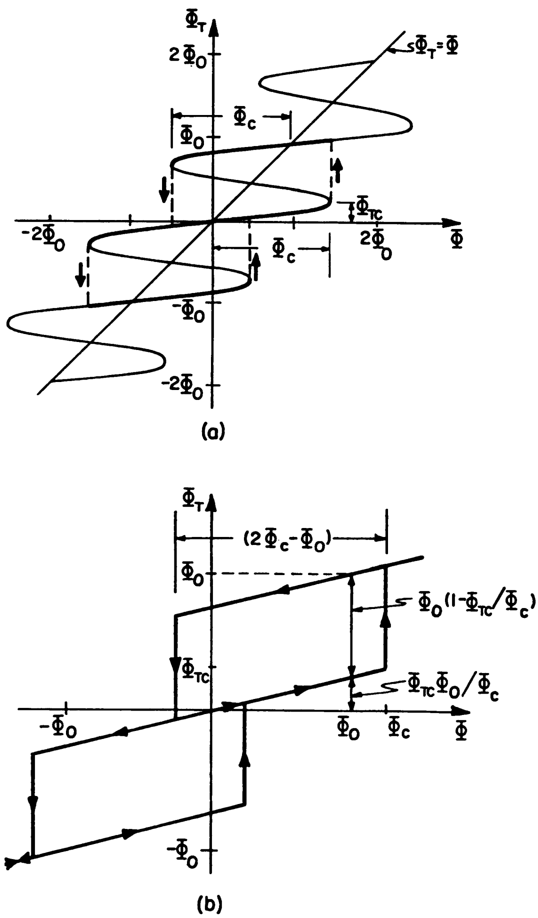

Figure 15. The rf SQUID: (a) total flux Φ_T vs. Φ for $LI_0 = 1.25\ \Phi_0$; (b) values of Φ_T as Φ is quasistatically increased and then decreased.

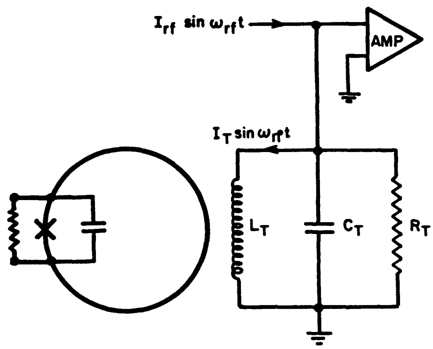

Figure 16. The rf SQUID inductively coupled to a resonant tank circuit.

We now consider the radio frequency operation of the device. The SQUID is inductively coupled to the coil of an LC-resonant circuit with a quality factor $Q = R_T/\omega_{rf}L_T$ via a mutual inductance $M = K(LL_T)^{1/2}$ – see Fig. 16. Here, L_T, C_T, and R_T are the inductance, capacitance and (effective) parallel resistance of the tank circuit, and $\omega_{rf}/2\pi$ is its resonant frequency, typically 20 or 30 MHz. The tank circuit is excited at its resonant frequency by a current I_{rf} $\sin\omega_{rf}t$, which generates a current of amplitude $I_T = QI_{rf}$ in the inductor. The voltage V_T across the tank circuit is amplified with a preamplifier having a high input impedance. First, consider the case $\Phi = 0$. As we increase I_{rf} from zero, the peak rf flux applied to the loop is $MI_T = QMI_{rf}$, and V_T increases linearly with I_{rf}. The peak flux becomes equal to Φ_c when $I_T = \Phi_c/M$ or $I_{rf} = \Phi_c/MQ$, at A in Fig. 17. The corresponding peak rf voltage across the tank circuit is

$$V_T^{(n)} = \omega_{rf}L_T\Phi_c/M, \tag{4.5}$$

where the superscript (n) indicates $\Phi = n\Phi_0$, in this case with n=0. At this point the SQUID makes a transition to either the k = +1 state or the k = -1 state. As the SQUID traverses the hysteresis loop, energy ΔE is extracted from the tank circuit. Because of this loss, the peak flux on the next half cycle is less than Φ_c, and no transition occurs. The tank circuit takes many cycles to recover sufficient energy to induce a further transition, which may be into either the k = +1 or -1 states. If we now increase I_{rf}, transitions are induced at the same values of I_T and V_T but, because energy is supplied at a higher rate, the stored energy builds up more rapidly after each energy loss ΔE, and transitions occur more frequently. In the absence of thermal fluctuations (Sec. 4.2), the "step" AB in Fig. 17 is at constant voltage. At B, a transition is induced on each positive and negative rf peak, and a further increase in I_{rf} produces the "riser" BC. At C, transitions from the k = ±1 to the k = ±2 states occur, and a second step begins. As we continue to increase I_{rf}, we observe a series of steps and risers.

If we now apply an external flux $\Phi = \Phi_0/2$, the hysteresis loops in Fig. 15(b) are shifted by $\Phi_0/2$. Thus, a transition occurs on the positive peak of the rf cycle at a flux $(\Phi_c - \Phi_0/2)$, whereas on the negative peak the required flux is $-(\Phi_c + \Phi_0/2)$. As a result, as we increase I_{rf} from zero, we observe the first step at D in Fig. 17 at

$$V_T^{(n+1/2)} = \omega_{rf}L_T(\Phi_c-\Phi_0/2)/M. \tag{4.6}$$

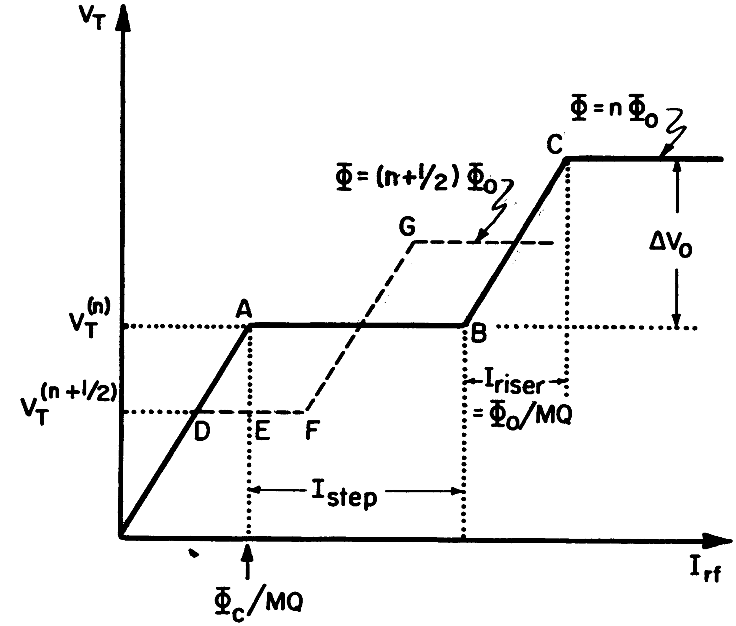

Figure 17. V_T vs. I_{rf} in the absence of thermal noise for $\Phi = n\Phi_0$, $(n+1/2)\Phi_0$.

As we increase I_{rf} from D to F, the SQUID traverses only one hysteresis loop, corresponding to the k = 0 to k = +1 transition at $(\Phi_c - \Phi_0/2)$. A further increase in I_{rf} produces the riser FG, and at G, transitions begin at a peak rf flux $-(\Phi_C + \Phi_0/2)$. In this way, we observe a series of steps and risers for $\Phi = \Phi_0/2$, interlocking those for $\Phi = 0$ (Fig. 17). As we increase Φ from zero, the voltage at which the first step appears will drop to a minimum (D) at $\Phi_0/2$ and rise to its maximum value (A) at $\Phi = \Phi_0$. The change in V_T as we increase Φ from 0 to $\Phi_0/2$, found by subtracting Eq. (4.6) from Eq.(4.5), is $\omega_{rf}L_T\Phi_0/2M$. Thus, for a small change in flux near $\Phi = \Phi_0/4$, we find the transfer function

$$V_\Phi = \omega_{rf}L_T/M. \tag{4.7}$$

At first sight, Eq.(4.7) suggests that we can make V_Φ arbitrarily large by reducing K sufficiently. However, we obviously cannot make K so small that the SQUID has no influence on the tank circuit, and we need to establish a lower bound on K. To operate the SQUID, we must be able to choose a value of I_{rf} that intercepts the first step for all values of Φ : this requirement is satisfied if the point F in Fig. 17 lies to the right of E, that is, if DF exceeds DE. We can calculate DF by noting that the power dissipation in the SQUID is zero at D and $\Delta E(\omega_{rf}/2\pi) \approx I_0\Phi_0\omega_{rf}/2\pi$ at F. Thus, $(I_{rf}^{(F)}-I_{rf}^{(D)})V_T^{(n+1/2)}/2 = I_0\Phi_0\omega_{rf}/2\pi$ (I_{rf} and V_T are peak, rather than rms values). Furthermore, we easily can see that $I_{rf}^{(E)} - I_{rf}^{(D)} = \Phi_0/2MQ$. Assuming $LI_0 \approx \Phi_0$ and using Eq.(4.5), we find that the requirement $I_{rf}^{(E)} > I_{rf}^{(D)}$ can be written in the form

$$K^2Q \gtrsim \pi/4. \tag{4.8}$$

If we set $K \approx Q^{-1/2}$, Eq.(4.7) becomes

$$V_\Phi \approx \omega_{rf}(QL_T/L)^{1/2}. \tag{4.9}$$

To operate the SQUID, one adjusts I_{rf} so that the SQUID remains biased on the first step - see Fig. 17 - for all values of Φ. The rf voltage across the tank circuit is amplified and demodulated to produce a signal that is periodic in Φ. A modulating flux, typically at 100kHz and with a peak-to-peak amplitude of $\Phi_0/2$, is also applied to the SQUID, just as in the case of the dc SQUID. The voltage produced by this modulation is lock-in detected, integrated, and fed back as a current into the modulation coil to flux-lock the SQUID.

4.2 THEORY OF NOISE IN THE RF SQUID

A detailed theory has been developed for noise in the rf SQUID [52-60]; in contrast to the case for the dc SQUID, noise contributions from the tank circuit and preamplifier are also important. We begin by discussing the intrinsic noise in the SQUID. In the previous section we assumed that transitions from the k = 0 to the k = 1 state occurred precisely at $\Phi = \Phi_C$. In

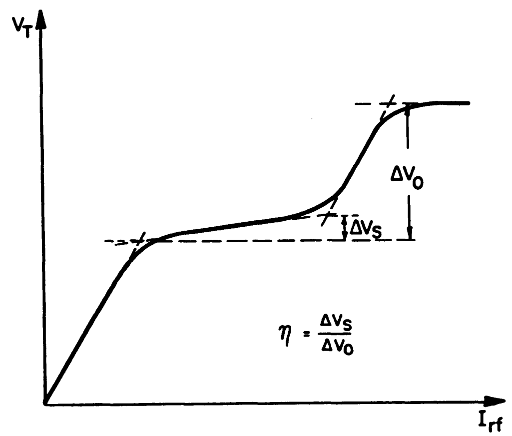

Figure 18. V_T vs. I_{rf} showing the effects of thermal noise.

fact, thermal activation causes the transition to occur stochastically, at lower values of flux. Kurkijärvi [52] calculated the distribution of values of Φ at which the transitions occur; experimental results [61] are in good agreement with his predictions. When the SQUID is driven with an rf flux, the fluctuations in the value of flux at which transitions occur have two consequences. First, noise is introduced on the peak voltage V_T, giving an equivalent intrinsic flux noise spectral density [53, 57]

$$S_\Phi^{(i)} \approx \frac{(LI_0)^2}{\omega_{rf}} \left[\frac{2\pi k_B T}{I_0 \Phi_0}\right]^{4/3}. \tag{4.10}$$

Second, the noise causes the steps to tilt (Fig. 18), as we easily can see by considering the case for $\Phi = 0$. In the presence of thermal fluctuations the transition from the k = 0 to the k = 1 state (for example) has a certain probability of occurring at any given value of the total flux

$\Phi + \Phi_{rf}$. Just to the right of A in Fig. 17 this transition occurs at the peak of the rf flux once in many rf cycles. Thus, the probability of the transition occurring in any one cycle is small. On the other hand, at B a transition must occur at each positive and negative peak of the rf flux, with unity probability. To increase the transition probability, the peak value of the rf flux and hence V_T must increase as I_{rf} is increased from A to B. Jackel and Buhrman [54], introduced the slope parameter η defined in Fig. 18, and showed that it was related to $S_\Phi^{(i)}$ by the relation

$$\eta^2 \approx S_\Phi^{(i)}\omega_{rf}/\pi\Phi_0^2\ , \tag{4.11}$$

provided η was not too large. This relation is verified experimentally.

The noise temperature T_a of typical rf amplifiers operated at room temperature is substantially higher than that of amplifiers operated at a few hundred kilohertz, and is therefore not negligible for rf SQUIDs operated at liquid ^{4}He temperatures. Furthermore, part of the coaxial line connecting the tank circuit to the preamplifier is at room temperature. Since the capacitances of the line and the amplifier are a substantial fraction of the capacitance of the tank circuit, part of the resistance damping the tank circuit is well above the bath temperature. As a result, there is an additional contribution to the noise which we combine with the preamplifier noise to produce an effective noise temperature T_a^{eff}. The noise energy contributed by these extrinsic sources can be shown to be [54, 58] $2\pi\eta k_B T_a^{eff}/\omega_{rf}$. Combining this contribution with the intrinsic noise, one finds

$$\varepsilon \approx \frac{1}{\omega_{rf}}\left(\frac{\eta\pi^2\Phi_0^2}{2L} + 2\pi\eta k_B T_a^{eff}\right)\ . \tag{4.12}$$

Equation (4.12) shows that ε scales as $1/\omega_{rf}$, but one should bear in mind that T_a tends to increase with ω_{rf}. Nonetheless, as we shall see shortly, improvements in performance have been achieved by operating the SQUID at frequencies much higher than the usual 20 or 30 MHz.

4.3 PRACTICAL rf SQUIDs

Although generally less sensitive than the dc SQUID, the rf SQUID is entirely adequate for a wide range of applications. It is has been commercially available since the early 1970's, notably from BTi (formerly SHE). Figure 19 shows a cut-away drawing of the BTi rf SQUID [44], which has a toroidal configuration machined from Nb. One way to understand this geometry is to imagine rotating the SQUID in Fig. 14 through 360° about a line running through the junction from top to bottom of the page. This procedure produces a toroidal cavity connected at its center by the junction. If one places a toroidal coil in this cavity, a current in the coil produces a flux that is tightly coupled to the SQUID. In Fig. 19, there are actually two such cavities, one containing the tank circuit-modulation-feedback coil and the other the input coil. This separation eliminates cross-talk between the two coils. Leads to the two coils are brought out via screw-terminals. The junction is made from thin films of Nb. This device is self-shielding against external magnetic field fluctuations, and has proven to be reliable and convenient to use. In particular, the Nb input terminals enable one to connect different input circuits in a straightforward way. A typical device has a white noise energy of 5×10^{-29} JHz^{-1}, with a 1/f noise energy of perhaps 10^{-28} JHz^{-1} at 0.1Hz.

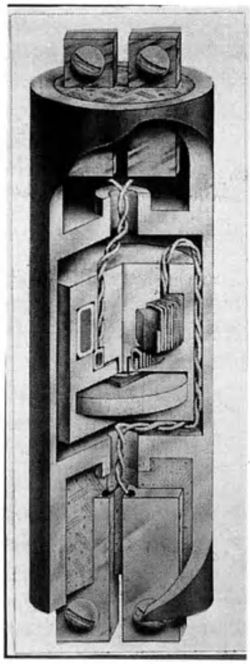

Figure 19. Cut-away drawing of toroidal SQUID (courtesy D. Paulsen, BTi, Inc.).

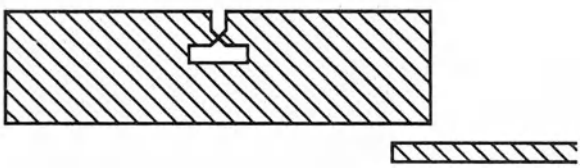

Figure 20. Microwave rf SQUID consisting of Nb film microstrip resonator coupled to microstrip input and output line (from ref. [65]).

As we saw in Eq. (4.12), one can improve the noise energy by operating the rf SQUID at high frequencies [62, 63]. One can also reduce T_a^{eff} by cooling the preamplifier [62, 64], thereby reducing T_a and reducing the temperature of the tank circuit to that of the helium bath. Recently, Mück and co-workers [65] have taken advantage of both of these techniques to make substantial improvements in the performance of rf SQUIDs.

To operate a SQUID at 3GHz, Mück used an ingenious microstrip configuration, shown in Fig. 20. The SQUID consisted of a 100-nm-thick niobium film, with a hole varying from 50 x $50\mu m^2$ to 200 x $200\mu m^2$, deposited on a 1-mm-thick sapphire substrate. The junction was either a microbridge or a Nb-Al_2O_3-Nb tunnel junction with a resistive shunt to reduce β_c to about 0.8. The sapphire substrate was mounted on a printed circuit board, the copper cladding serving as a ground plane for the microstrip resonator. The microwaves were coupled in via a second microstrip (Fig. 20) and the SQUID signal was coupled out via the same microstrip; a directional coupler separated the incoming bias from the outgoing signal. The Q of the resonator was typically 500 to 1000, and K was chosen to make $K^2Q \approx 1$. For SQUIDs with a tunnel junction, a peak-to-peak signal as high as $80\mu V$ was obtained, corresponding to

$V_\Phi = 160\mu V/\Phi_0$. Using a room temperature amplifier with an rms noise of 0.5 $nVHz^{-1/2}$, Mück obtained a flux noise of $3 \times 10^{-6}\Phi_0\ Hz^{-1/2}$ in a flux-locked loop at frequencies down to 0.1 Hz. The best noise energy achieved was about $2 \times 10^{-31}\ JHz^{-1}$. SQUIDs were also fabricated with integrated Nb coils deposited on them in the same way as for dc SQUIDs.

To improve the performance further, Mück [65] used a cooled GaAs HEMT (High Electron Mobility Transistor) as a preamplifier, achieving a noise energy of about 3×10^{-32} JHz^{-1} in a flux-locked loop at 1Hz. This is a remarkable improvement in the performance of the rf SQUID, to a value that is comparable with that of typical thin-film dc SQUIDs.

5. SQUID-Based Instruments

Both dc and rf SQUIDs are used as sensors in a far-ranging assortment of instruments. I here briefly discuss some of them: my selection is far from exhaustive, but does include the more commonly used instruments.

Each instrument involves a circuit attached to the input coil of the SQUID. We should recognize from the outset that, in general, the presence of the input circuit influences both the signal and noise properties of the SQUID while the SQUID, in turn, reflects a complex impedance into the input. Because the SQUID is a nonlinear device a full description of the interactions is complicated, and we shall not go into the details here. However, one aspect of this interaction, first pointed out by Zimmerman [66], is easy to understand. Suppose we connect a superconducting pick-up loop of inductance L_p to the input coil of inductance L_i to form a magnetometer, as shown in Fig. 21(a). It is easy to show that the SQUID inductance L is reduced to the value

$$L' = L\left[1 - \alpha^2 L_i / (L_i + L_p)\right], \tag{5.1}$$

where α^2 is the coupling coefficient between L and L_i. We have neglected any stray inductance in the leads connecting L_i and L_p, and any stray capacitance. The reduction in L tends to increase the transfer coefficient of both the dc SQUID [Eq.(3.7)] and the rf SQUID [Eq.(4.9)]. In most cases, the reduction of L and the change in the noise properties will be detectable, but they will not have a major effect on the results presented here.

5.1 MAGNETOMETERS AND GRADIOMETERS

One of the simplest instruments is the magnetometer [Fig. 21(a)]. A pick-up loop is connected across the input coil to make a superconducting flux transformer. The SQUID and input coil are generally enclosed in a superconducting shield. If one applies a magnetic flux, $\delta\Phi^{(p)}$, to the pick-up loop, flux quantization requires that

$$\delta\Phi^{(p)} + (L_i + L_p)J_s = 0, \tag{5.2}$$

where J_s is the supercurrent induced in the transformer. We have neglected the effects of the SQUID on the input circuit. The flux coupled into the SQUID, which we assume to be in a flux-locked loop, is $\delta\Phi = M_i|J_s| = M_i\delta\Phi^{(p)} / (L_i + L_p)$. We find the minimum detectable value of $\delta\Phi^{(p)}$ by equating $\delta\Phi$ with the equivalent flux noise of the SQUID. Defining $S_\Phi^{(p)}$ as the spectral density of the equivalent flux noise referred to the pick-up loop, we find

$$S_\Phi^{(p)} = \frac{(L_p+L_i)^2}{M_i^2} S_\Phi. \tag{5.3}$$

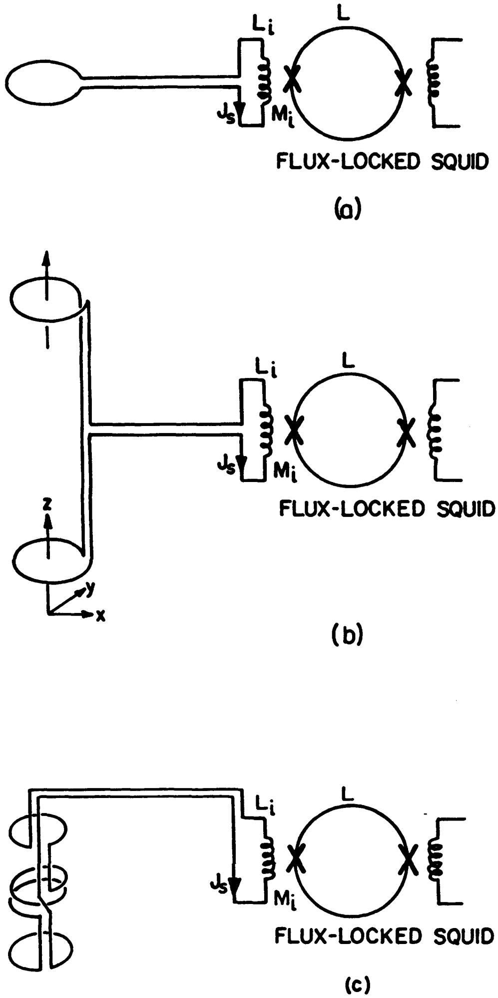

Figure 21. Superconducting flux transformers:(a) magnetometer, (b) first-derivative gradiometer, (c) second-derivative gradiometer.

Introducing the equivalent noise energy referred to the pick-up loop, we obtain

$$\frac{S_\Phi^{(p)}}{2L_p} = \frac{(L_p+L_i)^2}{L_i\,L_p}\,\frac{S_\Phi}{2\alpha^2 L}\,. \tag{5.4}$$

We observe that Eq.(5.4) has the minimum value

$$S_\Phi^{(p)}\,/\,2L_p = 4\varepsilon(f)\,/\,\alpha^2 \tag{5.5}$$

when $L_i = L_p$. Thus, a fraction $\alpha^2/4$ of the energy in the pick-up loop is transferred to the SQUID. In this derivation we have neglected noise currents in the input circuit arising from noise in the SQUID, the fact that the input circuit reduces the SQUID inductance, and any possible coupling between the feedback coil of the SQUID and the input circuit. Having obtained the flux resolution for $L_i = L_p$, we can immediately write down the corresponding magnetic field resolution $B_N^{(p)} = (S_\Phi^{(p)})^{1/2}/\pi r_p^2$, where r_p is the radius of the pick-up loop:

$$B_N^{(p)} = 2\sqrt{2}L_p^{1/2}\varepsilon^{1/2}/\pi r_p^2\alpha\,. \tag{5.6}$$

For a loop made from wire of radius r_0, one finds [67] $L_p = \mu_0 r_p[\ln(8r_p/r_0) - 2]$, where $\mu_0 = 4\pi \times 10^{-7}$ henry/meter; for a reasonable range of values of r_p/r_0 we can set $L_p \approx 5\mu_0 r_p$. Thus, we obtain $B_N^{(p)} \approx 2(\mu_0\varepsilon)^{1/2}/\alpha r_p^{3/2}$. This indicates that one can, in principle, improve the magnetic field resolution indefinitely by increasing r_p, keeping $L_i = L_p$. Of course, in practice, the size of the cryostat will impose an upper limit on r_p. If we take $\varepsilon = 10^{-28}$ $\mathrm{JHz^{-1}}$ (a somewhat conservative value for an rf SQUID), $\alpha = 1$, and $r_p = 25$ mm, we find $B_N^{(p)} \approx 5 \times 10^{-15}$ tesla $\mathrm{Hz^{-1/2}} = 5 \times 10^{-11}$ gauss $\mathrm{Hz^{-1/2}}$. This is a much higher sensitivity than that achieved by any nonsuperconducting magnetometer.

Magnetometers have usually involved flux transformers made of Nb wire. For example, one can make the rf SQUID in Fig. 19 into a magnetometer merely by connecting a loop of Nb wire to its input terminals. In the case of the thin-film dc SQUID, one can make an integrated magnetometer by fabricating a Nb loop across the spiral input coil. In this way, Wellstood *et al.* [28] achieved a magnetic field white noise of 5×10^{-15} tesla $\mathrm{Hz^{-1/2}}$ using a pick-up loop with a diameter of a few millimeters. One application of magnetometers is in geophysics [68] – see Sec. 5.7.

An important variation of the flux transformer is the gradiometer. Figure 21(b) shows an axial gradiometer that measures $\partial B_z/\partial z$. The two pick-up loops are wound in opposition and balanced so that a uniform field B_z links zero net flux to the transformer. A gradient $\partial B_z/\partial z$, on the other hand, does induce a net flux and thus generates an output from the flux-locked SQUID. Figure 21(c) shows a second-order gradiometer that measures $\partial^2 B_z/\partial z^2$; Fig. 22(a) is a photograph of a practical version. Thin-film gradiometers based on dc SQUIDs were made as long ago [32] as 1978, and a variety of devices [27,69-74] have been reported since then. Most thin film gradiometers have been planar, and therefore measure an off-diagonal gradient, for example, $\partial B_z/\partial x$ or $\partial^2 B_z/\partial x\partial y$. A representative device is shown in Fig. 22(b) [72]. However, Hoenig *et al.* [74] made a 37-channel biomagnetic system involving thin film first-derivative axial gradiometers. The pick-up loops are deposited on flexible printed circuit board which is then folded and bonded onto a supporting block. The leads from each gradiometer are bonded to the input coil of a thin-film dc SQUID.

The most important application of the gradiometer thus far is in neuromagnetism [75], notably to detect weak magnetic signals emanating from the human brain. The gradiometer discriminates strongly against distant noise sources, which have a small gradient, in favor of locally generated signals. One can thus use a second-order gradiometer in an unshielded environment, although the present trend is toward using first-order gradiometers in a shielded room of aluminum and mu-metal that greatly attenuates the ambient magnetic noise. In this application, axial gradiometers of the type shown in Fig. 21(a) actually sense magnetic field, rather than the gradient, because the distance from the signal source to the pick-up loop is less than the baseline of the gradiometer. The magnetic field sensitivity referred to one pick-up loop is typically $10\mathrm{fTHz}^{-1/2}$. Considerable progress in multichannel instruments has been made in recent years, and one with 122 gradiometers has recently been marketed [76].

(a)

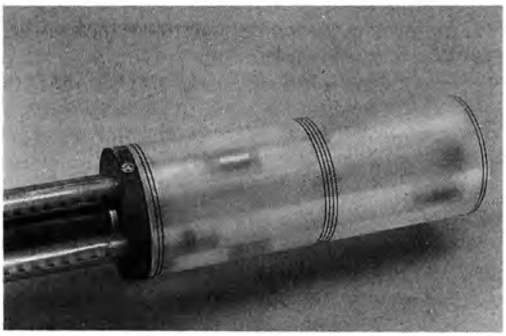

(b)

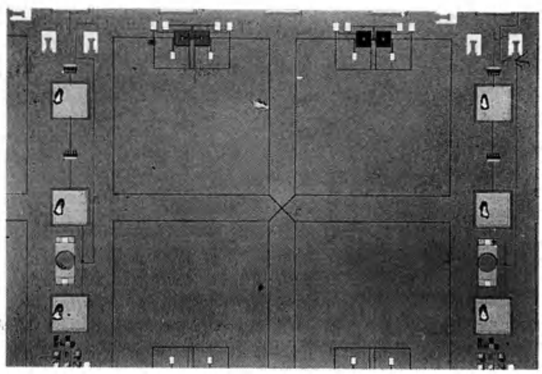

Figure 22. (a) Photograph of wire-wound second-derivative gradiometer for biomedical applications (courtesy BTi, inc.). (b) Second-order ($\partial^2 B_z/\partial x \partial y$) planar gradiometer fabricated in $Nb/Nb_2O_5/PbAuIn$ edge-junction technology. The device is 6.35mm square. (Courtesy M. B. Ketchen, W. J. Gallagher, R. L. Sandstrom and A. W. Kleinsasser, IBM [72])

There are two basic kinds of measurements made on the human brain. In the first, one detects spontaneous activity: a classic example is the generation of magnetic pulses by subjects suffering from focal epilepsy [77]. The second kind involves evoked response: for example, Romani *et al.* [78] detected the magnetic signal from the auditory cortex generated by tones of different frequencies. Extensive reviews of this work appear elsewhere in these proceedings.

There are several other applications of gradiometers. One kind of magnetic monopole detector [79] consists of a gradiometer: the passage of a monopole would link a flux h/e in the pick-up loop and produce a step-function response from the SQUID. Gradiometers have recently been of interest in studies of corrosion and in the location of fractures in pipelines and other structures. (See the chapters by Donaldson and Wikswo.)

5.2 SUSCEPTOMETERS

In principle, one easily can use the first-derivative gradiometer of Fig. 21(b) to measure magnetic susceptibility χ. One establishes a static field along the z-axis and lowers the sample into one of the pick-up loops. Provided χ is nonzero, the sample introduces an additional flux into the pick-up loop and generates an output from the flux-locked SQUID. Very sophisticated susceptometers are available commercially [80]. Room temperature access enables one to cycle samples rapidly, and one can measure χ as a function of temperature between 1.8 K and 400 K in fields up to 5.5 tesla. These systems are capable of resolving a change in magnetic moment as small as 10^{-8} emu.

Novel miniature susceptometers have been developed by Ketchen and co-workers [37, 81, 82]. One version is shown schematically in Fig. 23. The SQUID loop incorporates two pick-up loops wound in the opposite sense and connected in series. The two square pick-up loops, 17.5 μm on a side and with an inductance of about 30 pH, are deposited over a hole in the ground plane that minimizes the inductance of the rest of the device. The SQUID is flux biased at the maximum of V_Φ by means of a control current I_C in one of the pick-up loops. One can apply a magnetic field to the two loops by means of the current I_F; by passing a fraction of this current into the center tap I_C, one can achieve a high degree of electronic balance between the two loops. The sample to be studied is placed over one of the loops, and the output from the SQUID when the field is applied is directly proportional to the magnetization. At 4.2 K, the susceptometer is capable of detecting the magnetization due to as few as 3000 electron spins.

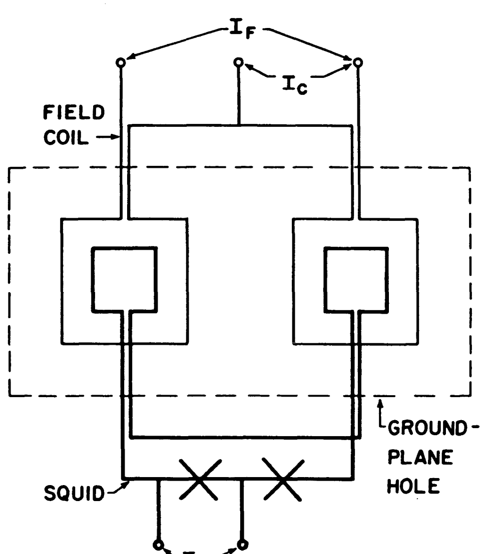

Figure 23. Thin-film miniature susceptometer (from ref. [81]).

Awschalom and co-workers [37, 82], have used a miniature susceptometer to perform magnetic spectroscopy of semiconductors with picosecond time-resolution. Linearly polarized pulses 4 ps in length are generated with a dye laser and split into a pump train and a weaker probe train. The time delay between the two trains can be varied, and each train is converted to circular polarization by a quarter-wave plate. The beams are chopped at 197Hz and passed down an optical fiber to the sample in the cryostat. The pump pulses induce a magneto-optical susceptibility χ_{op} which is subsequently measured by means of the much weaker probe pulses of intensity δI that induce a magnetization $\chi_{op}\delta I$. The magnetization is detected by the SQUID at the chopping frequency, and its output is lock-in detected. By varying the time delay between the pump and probe pulses, one can investigate the dynamics of the induced magnetization. One also can vary the dye laser frequency through the red region of the visible spectrum to study the energy dependence of the magnetization. This technique recently has been extended to temperatures down to 0.3K [82].

5.3 VOLTMETERS

Probably the first practical application of a SQUID was to measure tiny, quasistatic voltages [83]. One simply connects the signal source -- for example a low resistance through which a current can be passed -- in series with a known resistance and the input coil of the SQUID. The output from the flux-locked loop is connected across the known resistance to obtain a null-balancing measurement of the voltage. The resolution is generally limited by Nyquist noise in the input circuit, which at 4.2 K varies from about 10^{-15} V $\mathrm{Hz}^{-1/2}$ for a resistance of 10^{-8} Ω to about 10^{-10} V $\mathrm{Hz}^{-1/2}$ for a resistance of 100 Ω.

Applications of these voltmeters range from the measurement of thermoelectric voltages and of quasiparticle charge imbalance in nonequilibrium superconductors to noise thermometry and the high-precision comparison of the Josephson voltage-frequency relation in different superconductors.

5.4 THE DC SQUID AS A RADIOFREQUENCY AMPLIFIER

In recent years, the dc SQUID has been developed as a low-noise amplifier for frequencies up to 100 MHz or more [84]. To understand the theory for the performance of this amplifier, we need to extend the theory of Sec. 3.2 by taking into account the noise associated with the current J(t) in the SQUID loop. For a bare SQUID with $\beta = 1$, $\Gamma = 0.05$ and $\Phi = (2n+1)\Phi_0/4$, one finds the spectral density of the current to be [85]

$$S_J(f) \approx 11\, k_BT/R. \tag{5.7}$$

Furthermore, the current noise is partially correlated with the voltage noise across the SQUID, the cross-spectral density being [85]

$$S_{VJ}(f) \approx 12\, k_BT\ . \tag{5.8}$$

The correlation arises, roughly speaking, because the current noise generates a flux noise which, in turn, contributes to the total voltage noise across the junction, provided $V_\Phi \neq 0$.

If one imagines coupling a coil to the SQUID, the coil will "see" an impedance Z in the SQUID loop that can be written in the form [86]

$$\frac{1}{Z} = \frac{1}{j\omega\mathcal{L}} + \frac{1}{\mathcal{R}}\ . \tag{5.9}$$

The dynamic inductance $\mathcal{L}$ and dynamic resistance $\mathcal{R}$ are not simply related to L and R, but vary with bias current and flux; for example, $1/\mathcal{L}$ is zero for certain values of Φ.

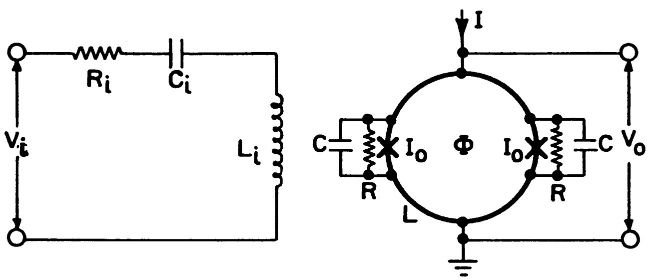

Figure 24. Tuned radiofrequency amplifier based on dc SQUID (from ref. [84]).

One can make a tuned amplifier, for example, by connecting an input circuit to the SQUID, as shown in Fig. 24. In general, the presence of this circuit modifies all of the SQUID parameters and the magnitude of the noise spectral densities [87]. Furthermore, the SQUID reflects an impedance $\omega^2 M_i^2/Z$ into the input circuit. Fortunately, however, one can neglect the mutual influence of the SQUID and input circuit, provided the coupling coefficient α^2 is sufficiently small, as it is under certain circumstances. For the purpose of illustration, we derive the noise temperature of the amplifier in Fig. 24. We assume given values of $S_V(f)$, $S_J(f)$, $S_{VJ}(f)$ and L_i, and find the values of C_i and R_i that optimize the noise temperature.

In the weak coupling limit, the noise current $J_N(t)$ induces a voltage $-M_iJ_N$ into the input circuit, and hence a current $-M_iJ_N / Z_i$, where

$$Z_i \approx R_i + j\omega L_i + 1/j\omega C_i \, . \tag{5.10}$$

Here, Z_i is the impedance of the input circuit and L_i and C_i are the series inductance and capacitance. The noise current in the input circuit, in turn, induces a flux in the SQUID loop and finally a voltage $-M_i^2 J_N V_\Phi/Z_i$ across the SQUID. Thus, the noise voltage across the SQUID in the presence of the input circuit is [84]

$$V_N'(t) = V_N(t) - M_i^2 \dot{J}_N V_\Phi / Z_i \, , \tag{5.11}$$

where $V_N(t)$ is the noise voltage of the bare SQUID, which we assume to be unchanged by the input circuit in the limit $\alpha^2 \to 0$. The spectral density of $V_N'(t)$ is easily found to be

$$S_V'(f) = S_V(f) + \frac{\omega^2 M_i^4 V_\Phi^2 S_J(f)}{|Z_i|^2} - \frac{2\omega M_i^2 V_\Phi(\omega L_i - 1/\omega C_i) S_{VJ}(f)}{|Z_i|^2} \, . \tag{5.12}$$

We now suppose that we apply a sinusoidal input signal frequency $\omega/2\pi$, with a mean-square amplitude $\langle V_i^2 \rangle$. The mean-square signal at the output of the SQUID is

$$\langle V_0^2 \rangle = M_i^2 V_\Phi^2 \langle V_i^2 \rangle / |(Z_i)|^2 . \tag{5.13}$$

The signal-to-noise ratio is

$$S/N = \langle V_0^2 \rangle / S_V'(f) B \tag{5.14}$$

in a bandwidth B. It is convenient to introduce a noise temperature T_N for the amplifier by setting S/N = 1 with $\langle V_i^2 \rangle = 4k_B T_N R_i B$. This procedure implies that the output noise power generated by the SQUID is equal to the output noise power generated by the resistor R_i when it is at a temperature T_N. We then can optimize T_N with respect to R_i and C_i for a given value of L_i, and find

$$R_i^{(opt)} = \frac{\alpha^2 \omega L_i L V_\Phi}{S_V} (S_V S_J - S_{VJ}^2)^{1/2}, \tag{5.15}$$

$$\frac{1}{\omega C_i^{(opt)}} = \omega L_i \left(1 + \frac{\alpha^2 S_{VJ} L V_\Phi}{S_V}\right), \tag{5.16}$$

and

$$T_N^{(opt)} = \frac{\pi f}{k_B V_\Phi} (S_V S_J - S_{VJ}^2)^{1/2}. \tag{5.17}$$

We note from Eq.(5.16) that the optimum noise temperature occurs off-resonance. It often is more convenient in practice to use the amplifier at the resonant frequency of the tank circuit, given by $\omega^2 L_i C_i = 1$ (neglecting reflected components from the SQUID). In that case, one finds optimum values [84]

$$R_i^{(res)} = \alpha^2 \omega L_i L V_\Phi (S_J / S_V)^{1/2} \tag{5.18}$$

and

$$T_N^{(res)} = \frac{\pi f}{k_B V_\Phi} (S_V S_J)^{1/2}. \tag{5.19}$$

Using the results of Eqs.(3.7), (3.8), (5.7) and (5.8), we can write Eq.(5.18) in the form

$$\alpha^2 \omega L_i / R_i^{(res)} = \alpha^2 Q \approx 1. \tag{5.20}$$

This result shows that high-Q input circuits imply that α^2 is small, thereby justifying the assumption made at the beginning of this section. One also finds

$$T_N(f) \approx 18 f T / V_\Phi \approx 2 f \varepsilon(f) / k_B. \tag{5.21}$$

Thus, although $\varepsilon(f)$ does not fully characterize an amplifier, as noted earlier, within the framework of the model, it does enable one to predict T_N.

One can easily calculate the gain on resonance. For $\alpha^2 \ll 1$, an input signal V_i produces an output voltage $V_0 \approx (V_i / R_i^{(res)}) M_i V_\Phi$. The power gain is thus $G = (V_0^2/R_D)/(V_i^2/R_i)$, where R_d is the dynamic output resistance $(\partial V/\partial I)_\Phi$ of the SQUID. If we take $R_d \approx R$, we find

$$G \approx V_\Phi / \omega. \tag{5.22}$$

Hilbert and Clarke [84] made several radiofrequency amplifiers with both tuned and untuned inputs, flux biasing the SQUID near $\Phi = (2n + 1)\Phi_0/4$. There was no flux-locked loop. The measured parameters were in good agreement with predictions. For example, for an amplifier with $R \approx 8\ \Omega$, $L \approx 0.4$ nH, $L_i \approx 5.6$nH, $M_i \approx 1$nH and $V_\Phi \approx 3\times10^{10}$ sec^{-1} at 4.2K, they found $G = 18.6 \pm 0.5$dB and $T_N = 1.7 \pm 0.5$K at 93MHz. The predicted values were 17dB and 1.1K, respectively.

We emphasize that in this theory and these measurements one is concerned only with the noise temperature of the amplifier itself. Nyquist noise from the resistor adds a contribution which, in the example just given, exceeds the amplifier noise. Thus, the optimization procedure just outlined does not necessarily give the lowest system noise, and one would use a different procedure when the value of T_N in Eq.(5.17) or Eq.(5.19) is well below T.

In concluding this section, we comment briefly on the quantum limit for the dc SQUID amplifier. At T = 0, Nyquist noise in the shunt resistors should be replaced with zero point fluctuations [Eq.(2.11]. Koch *et al.* [88] performed a simulation in this limit and concluded that, within the limits of error, the noise temperature of a tuned amplifier in the quantum limit should be given by

$$T_N \approx hf/k_B \ln 2. \qquad (5.23)$$

This is the result for any quantum-limited amplifier. The corresponding value for ε was approximately $\hbar$, but it should be emphasized that quantum mechanics does not impose any precise lower limit on ε [89]. A number of SQUIDs have obtained noise energies of $3\hbar$ or less, but there is no evidence as yet that a SQUID has attained quantum-limited performance as an amplifier.

5.5 MAGNETIC RESONANCE

SQUIDs have been used for two decades to detect magnetic resonance [90]. Most of the experiments involved the detection of magnetic resonance at low frequencies or the change in the static susceptibility of a sample induced by a resonance at high frequency. However, the development of the radiofrequency amplifier described in the previous section enables one to detect pulsed magnetic resonance directly at frequencies up to ~300 MHz.

Clarke, Hahn and co-workers have used the radiofrequency amplifier to perform nuclear quadrupole resonance [90] (NQR) and nuclear magnetic resonance [91] (NMR) experiments. They observed NQR in ^{35}Cl, which, in zero magnetic field, has two doubly degenerate nuclear levels with a splitting of 30.6856 MHz. The experimental configuration is shown in Fig. 25. The sample is placed in a superconducting pick-up coil, in series with which is an identical, counterwound coil. These coils are in series with an adjustable tuning capacitor C_i, the 4-turn input coil of a planar dc SQUID and 20 unshunted Josephson junctions. The resistor R_i represents contact resistance and losses in the capacitor. Radiofrequency pulses applied to the transmitter coil cause the nuclear spins to precess; after each pulse is turned off, the amplifier detects the precessing magnetization. The amplified signal is mixed down with a reference provided by the rf generator, and the mixed-down signal is passed through a low-pass filter, observed on an oscilloscope, and recorded digitally for further analysis.

The major difficulty with this technique, and indeed with other pulsed methods, is the saturation of the amplifier by the very large rf pulse. In the present experiments, the effects of this pulse are reduced in two ways. First, the gradiometer-like configuration gives a common-mode rejection that can be as high as 3×10^4. Second, the series of junctions in the input circuit acts as a Q-spoiler [90]. As the current begins to build in the tuned circuit, the junctions switch to the resistive state with a total resistance of about 1 kΩ, thereby reducing the Q to ~1. When the pulse is turned off, the transients die out very quickly and the junctions revert to their zero voltage state, rapidly restoring Q to its full value, usually several thousand. In this way, one can combine the benefits of a high-Q tuned circuit and a sensitive amplifier while retaining a relatively short dead-time after each pulse. In their initial experiments, Hilbert *et al.*

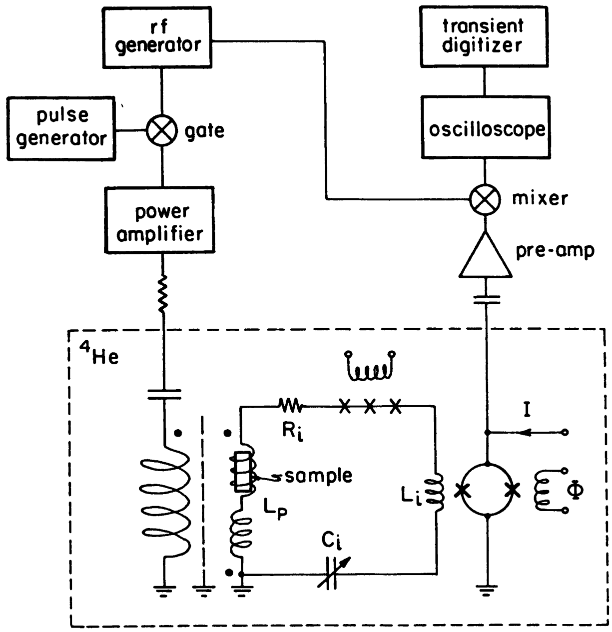

Figure 25. Circuit for NQR with dc SQUID amplifier (from ref. [90]).

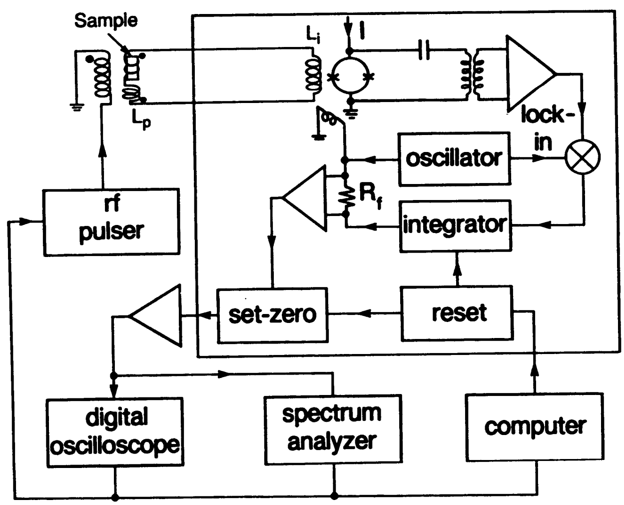

Figure 26. Configuration of NQR Fourier-transform spectrometer based on a dc SQUID amplifier (from ref. [95]).

[90] achieved a resolution for a single pulse of ~2×10^{16} spins (~2×10^{16} nuclear Bohr magnetons) in a bandwidth of 10kHz.

Subsequently, the Q-spoiler and SQUID amplifier were used to detect atomic polarization induced by precessing nuclear electric quadrupoles [92]. In this experiment, the $NaClO_3$ sample was placed in a capacitor that formed part of the tuned input circuit, and NQR induced in the usual way by radiofrequency pulses. The precessing electric quadrupole moments induce a net electric dipole moment in the neighboring atoms, provided the crystal is noncentro-symmetric. These dipole moments, in turn, produce an oscillating electric polarization in the crystal and hence a voltage on the capacitor that is amplified in the usual way. This technique yields information on the location and polarization of atoms near nuclear quadrupole moments.

The Q-spoiler and amplifier also have been used to detect nuclear magnetic resonance [91]. In these experiments one applies a magnetic field with an amplitude of several tesla to the crystal, and places the superconducting circuitry some distance away in a relatively low field. In yet another experiment, Sleator *et al.* [93] observed "spin noise" in ^{35}Cl. An rf signal at the NQR frequency equalized the populations of the two nuclear spin levels, and then was turned off to leave a zero-spin state. A SQUID amplifier (without a Q-spoiler) was able to detect the photons emitted spontaneously as the upper state decayed, even though the lifetime per nucleus for this process was ~10^6 centuries. The detected power was about 5×10^{-21}W in a bandwidth of about 1.3 kHz.

More recently, a dc SQUID with an untuned input circuit [94, 95] has been used to detect NQR in the frequency range 10 to 200kHz. The circuit configuration is shown in Fig. 26. The sample is placed inside one half of the turns of the superconducting pickup loop, which is wound in a gradiometer configuration and is connected to the input coil of the SQUID to form a superconducting flux transformer. The transmitter solenoid is wound coaxially around the sample and pick-up coil. The SQUID is flux modulated at 500kHz and operated in a flux-locked loop with a bandwidth of about 200kHz. During the application of the pulse that induces precession, the feedback loop is opened; after the pulse is turned off, the integrator is reset to zero before data acquisition begins. The use of an untuned input circuit not only results in a broad bandwidth but eliminates the Nyquist noise associated with a tuned circuit at the signal frequency. The effective noise temperature of the spectrometer was approximately 1mK for a bath temperature of 1.5K.

The spectrometer was used to study the zero-field NQR resonance of ^{14}N in powdered ammonium chlorate (NH_4ClO_4). Figure 27(a) shows the signal produced by two pulses 5ms apart, each pulse consisting of a single rf cycle at 45kHz. The averaged signal, consisting of 16,000 pulse sequences with a cycle rate of 3Hz, shows a free induction decay after the second pulse and the formation of a spin echo after 5ms. For the purpose of display, the signal has been demodulated with a frequency of 35kHz. Figure 27(b) shows the Fourier transform of a similar echo: we observe three sharp peaks at 17.4, 38.8 and 56.2kHz. Note that the frequencies of the lower two peaks sum to the highest frequency, indicating that we are exciting and observing simultaneously the three transitions of a three-level system. The longitudinal and transverse relaxation times at 1.5K were measured to be $T_1 = 63\pm6$ms and $T_2 = 22\pm2$ms, respectively. The sensitivity, resolution and broad bandwidth of the spectrometer, as well as the possibility of pulsed spin echo, relaxation and multidimensional experiments, make the technique attractive for low-frequency NQR and NMR studies of a wide range of solids, particularly in the polycrystalline or amorphous state.

5.6 GRAVITY WAVE ANTENNAS

A quite different application of SQUIDs is the detection of minute displacements, such as those of the bar in a gravity wave antenna [96, 97]. Several groups worldwide are using these antennas to search for the pulse of gravitational radiation that is expected to be emitted when a

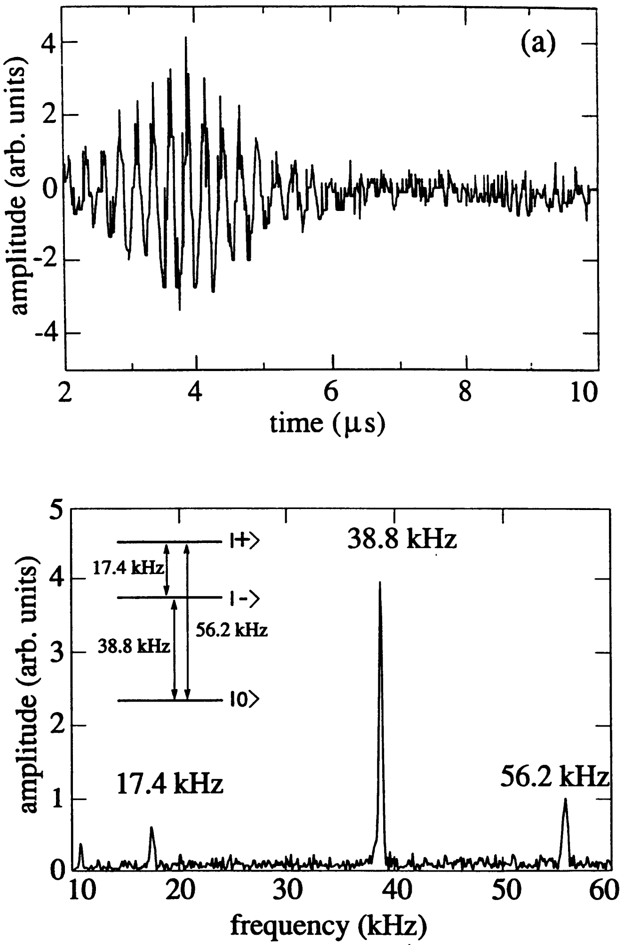

Figure 27. (a) Free induction decay after second pulse and spin echo of NH_4ClO_4 at T = 1.5 K. For the purpose of display, the real-time signal has been demodulated with 35kHz. (b) Fourier transform of spin echo. The three resonant peaks are due to transitions between energy levels (shown inset) of ^{14}N nuclei in the presence of electric field gradient in NH_4ClO_4 (see text). In inset, $|0\rangle = |10\rangle$ and $|\pm\rangle = (|11\rangle \pm |1 -1\rangle)/\sqrt{2}$ where $|I,m\rangle$ is the eigenstate of ^{14}N nucleus (I = 1) with $I_z = m$.

star collapses. The radiation induces longitudinal oscillations in the large, freely suspended bar, but because the amplitude is very tiny, one requires the sensitivity of a dc SQUID to detect it. As an example, we briefly describe the antenna at Stanford University, which consists of an aluminum bar 3 meters long (and weighing 4800 kg) suspended in a vacuum chamber at 4.2 K. The fundamental longitudinal mode is at $\omega_a/2\pi \approx 842$ Hz, and the Q is 5×10^6. The transducer is shown schematically in Fig. 28. A circular niobium diaphragm is clamped at its perimeter to one end of the bar, with a flat spiral coil made of niobium wire mounted on each side. The two coils are connected in parallel with each other and with the input coil of a SQUID; this entire circuit is superconducting. A persistent supercurrent circulates in the closed loop formed by the two spiral coils. The associated magnetic fields exert a restoring force on the diaphragm so that by adjusting the current, one can set the resonant frequency of the diaphragm equal to that of the bar. A longitudinal oscillation of the bar induces an oscillation in the position of the diaphragm relative to the two coils, thereby modulating their inductances. As a result of flux quantization, a fraction of the stored supercurrent is diverted into the input coil of the SQUID, which detects it in the usual way.

The present Stanford antenna has a root-mean-square strain sensitivity $\langle(\delta\ell)^2\rangle^{1/2}/\ell$ of 10^{-18}, where ℓ is the length of the bar, and $\delta\ell$ is its longitudinal displacement. This very impressive sensitivity, which is limited by thermal noise in the bar, is nonetheless adequate to detect events only in our own galaxy. Because such events are rare, there is very strong motivation to make major improvements in the sensitivity.

If the bar could be cooled sufficiently, the strain resolution would be limited only by the bar's zero-point motion and would have a value of about 3×10^{-21}. At first sight one might expect that the bar would have to be cooled to an absurdly low temperature to achieve this quantum limit, because a frequency of 842 Hz corresponds to a temperature $\hbar\omega_a/k_B$ of about 40nK. However, it turns out that one can make the effective noise temperature T_{eff} of the antenna much lower than the temperature T of the bar. If a gravitational signal in the form

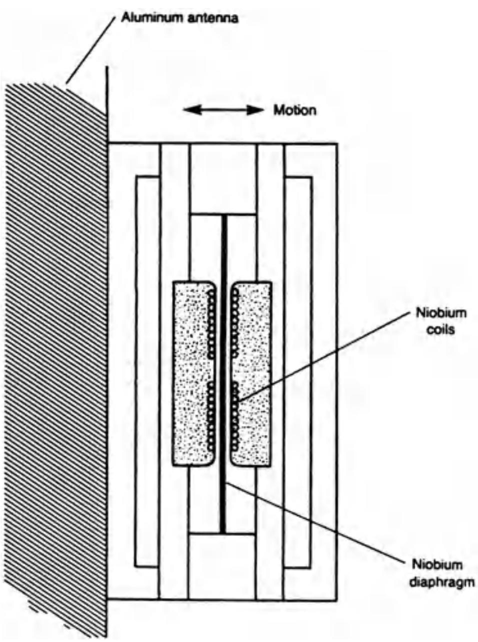

Figure 28. Transducer for gravity wave antenna. (Courtesy P.F. Michelson)

of a pulse of length τ_s interacts with an antenna that has a decay time Q/ω_a, then the effective noise temperature is given approximately by the product of the bar temperature and the pulse length divided by the decay time: $T_{eff} \approx \tau_s \omega_a T/Q$. Thus, one can make the effective noise temperature much less than the temperature of the bar by increasing the bar's resonant quality factor sufficiently. To achieve the quantum limit, in which the bar energy $\hbar\omega_a$ is greater than the effective thermal energy $k_B T_{eff}$, one would have to lower the temperature T below $Q\hbar/k_B\tau_s$, which is about 40 mK for a quality factor Q of 5 x 10^6 and a pulse length τ_s of 1 msec. One can cool the antenna to this temperature with the aid of a large dilution refrigerator.

Needless to say, to detect the motion of a quantum-limited antenna, one needs a quantum-limited transducer, a requirement that has been the major driving force in the development of ultra-low-noise dc SQUIDs. As we have seen, however, existing dc SQUIDs at low temperatures are now within striking distance of the quantum limit, and there is every reason to believe that one will be able to operate an antenna quite close to the quantum limit within a few years.

5.7 GEOPHYSICAL APPLICATIONS

Low-T_c SQUIDs have been used in a wide range of geophysical applications, including magnetotellurics, controlled source electromagnetic sounding, gravity gradiometers, rock magnetism and paleomagnetism, tectomagnetism and internal ocean waves [68]. We shall briefly describe two very different techniques, namely the gravity gradiometer and magnetotellurics.

The gravity gradiometer, which also makes use of a transducer to detect minute displacements, has been pioneered by Paik [98] and Mapoles [99]. The gradiometer consists of two niobium proof masses, each constrained by springs to move along a common axis (Fig. 29). A single-layer spiral coil of niobium wire is attached to the surface of one of the masses so that the surface of the wire is very close to the opposing surface of the other mass. Thus, the inductance of the coil depends on the separation of the two proof masses, which, in turn, depends on the gravity gradient. The coil is connected to a second superconducting coil which is coupled to a SQUID via a superconducting transformer. A persistent supercurrent, I, maintains a constant flux in the detector circuit. Thus, a change in the inductance of the pick-up coil produces a change in I, and hence, a flux in the SQUID that is related to the gravity gradient. More sophisticated versions of this design enable one to balance the restoring forces of the two springs electronically [99], thereby eliminating the response to an acceleration (as opposed to an acceleration gradient). Sensitivities of a few Eötvös $Hz^{-1/2}$ have been achieved at frequencies above 2 Hz. Instruments of this kind could

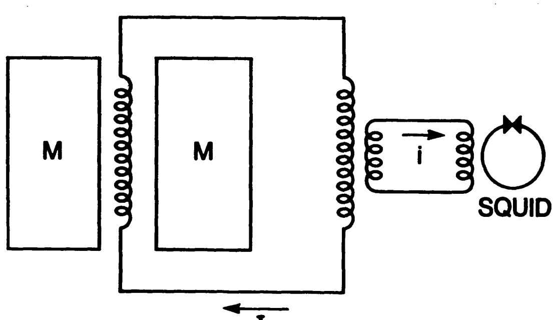

Figure 29. Gravity gradiometer showing two proof masses (M) on either side of a planar spiral coil (from ref. [99]).

be used to map the earth's gravity gradient, and may be used to test the inverse gravitational square law and in inertial navigation.

We turn now to magnetotellurics [100], in which one makes use of electromagnetic energy propagating to the earth from the ionosphere (<1Hz) and thunderstorm activity (>1Hz). The incident field is reflected by the earth, but components of the electric and magnetic fields, $\vec{E}(\omega)$ and $\vec{H}(\omega)$, decay into the ground with a characteristic length $\delta \approx 0.5\ (\rho T)^{1/2}$ km, where ρ is the resistivity in Ωm and T is the period in seconds. The frequency range of interest is typically 10^{-4} to 10^2Hz; at 1Hz δ is usually between 1 and 5km. One measures simultaneously the horizontal components of the magnetic field, $H_x(t)$ and $H_y(t)$, and of the electric field, $E_x(t)$ and $E_y(t)$, the Fourier components of which are related via the impedance tensor $\underline{\underline{Z}}(\omega)$:

$$E_x(\omega) = Z_{xx}(\omega)H_x(\omega) + Z_{xy}(\omega)H_y(\omega) \tag{5.24}$$

and

$$E_y(\omega) = Z_{yx}(\omega)H_x(\omega) + Z_{yy}(\omega)H_y(\omega) \quad . \tag{5.25}$$

The magnetic fields are measured by magnetometers or induction coils and the electric fields by buried electrodes connected to sensitive amplifiers. In the conventional analysis scheme, one multiplies each equation in turn by the complex conjugate of one of the fields, and averages the equations over a number of data records to reduce noise. One then solves a subset of the equations for the elements of the impedance tensor. For a homogeneous earth, the elements Z_{xx} and Z_{yy} are zero. In general, however, all four elements are non-zero, and in the usual procedure one rotates the axes of $\underline{\underline{Z}}$ to minimize the quantity $|Z_{xx}(\omega)|^2 + |Z_{yy}(\omega)|^2$. One of the axes is then aligned along the direction of maximum translational invariance, and one assumes that the ground can be represented adequately by a 2-D model so that Z_{xx} and Z_{yy} are negligible. The results are presented as the apparent resistivities in the x- and y-directions of the rotated tensor, $\rho_{xy}(\omega) = 0.2|Z_{xy}(\omega)|^2T$ and $\rho_{yx}(\omega) = 0.2|Z_{yx}(\omega)|^2T$, where ρ_{xy} and ρ_{yx} are in Ωm, and Z_{xy} and Z_{yx} are in (mV/km)nT.

Unfortunately, estimates of $\underline{\underline{Z}}(\omega)$ obtained in this way are often unreliable because of noise that can produce large biases in the results. Gamble *et al.* [101] attempted to overcome this problem by using SQUID magnetometers with much lower noise than the induction coils used previously. They found, however, that the use of a quieter magnetometer did not lead to an improvement in the data. They then introduced the remote reference technique [101] in which in addition to the measurement of H_x, H_y, E_x and E_y at the magnetotelluric site one also measures simultaneously the magnetic fields H_{xr} and H_{yr} at a remote site several kilometers away using a second magnetometer. By multiplying Eqs. (5.24) and (5.25) in turn by $H^*_{xr}(\omega)$ and $H^*_{yr}(\omega)$ and averaging over many data records one obtains four equations that can be solved for the elements of the impedance tensor. For example, one finds

$$Z_{xy}(\omega) = \frac{\langle E_x H^*_{yr}\rangle \langle H_x H^*_{xr}\rangle - \langle E_x H^*_{xr}\rangle \langle H_x H^*_{yr}\rangle}{\langle H_x H^*_{xr}\rangle \langle H_y H^*_{yr}\rangle - \langle H_x H^*_{yr}\rangle \langle H_y H^*_{xr}\rangle} \quad . \tag{5.26}$$

Provided any noise sources at the magnetotelluric site and at the remote site are uncorrelated, the estimates for the impedance tensor will be unbiased by noise. Figure 30 shows the apparent resistivities obtained at a site in Bear Valley, California, and illustrates the very high quality of the data that can be obtained with this technique.

An important additional benefit of the remote reference scheme is that it enables one to place reliable confidence limits [102] on the apparent resistivities, an essential requirement if one is to carry out meaningful modeling. The probable errors can be as low as a few tenths

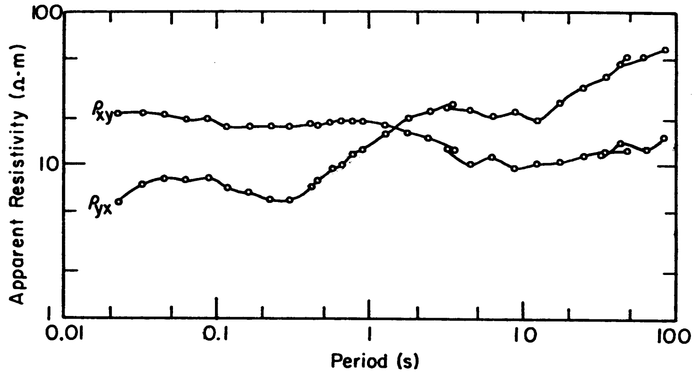

Figure 30. Apparent resistivities obtained at site in Bear Valley, California using remote reference magnetotellurics. (From ref. [101].)

of one percent, particularly at higher frequencies where a good deal of data is usually available. Once the apparent resistivities and other data have been collected at a series of sites, one performs an inversion to obtain the resistivity of the ground as a function of position and depth.

SQUIDs were used for magnetotellurics in the early 1980's but were abandoned when the price of oil dropped, and oil prospecting was curtailed. The need to use liquid helium in remote areas outside the continental United States also proved to be a serious impediment. However, the introduction of liquid nitrogen-cooled SQUIDs is likely to generate a renewed interest in their applications to geophysics.

6. High-T_c SQUIDs

The advent of the high-T_c superconductors has resulted in a world-wide effort to develop SQUIDs and flux transformers operating in liquid nitrogen at 77K. I cannot hope to do justice to the vast literature on the subject that has appeared in the last seven years, but I will give some idea of the current state of the art. I begin with a brief survey of the many types of Josephson junction that have been invented, and then discuss the design criteria for SQUIDs operating at 77K. The rest of the section is devoted to a description of practical dc and rf SQUIDs and flux transformers.

6.1 JOSEPHSON JUNCTIONS

The development of a reproducible junction technology has been a major preoccupation. Many structures have been made, all with nonhysteretic I-V characteristics, and I have divided them into three broad classes: *grain boundary* junctions, which may be natural or engineered, *barrier* junctions, which involve a barrier of a nonsuperconducting material, and *weakened* junctions, in which a region of the film is weakened in a controlled way. These various junctions are illustrated in Fig. 31.

To my knowledge, the first thin-film Josephson junction was made by Koch *et al.* [103], who made polycrystalline films of $YBa_2Cu_3O_{7-x}$ (YBCO) containing randomly oriented grains [Fig. 31(a)]. Using a photomask they ion implanted a region of the film to make it nonsuperconducting, leaving a microbridge of superconductor crossed by one or perhaps

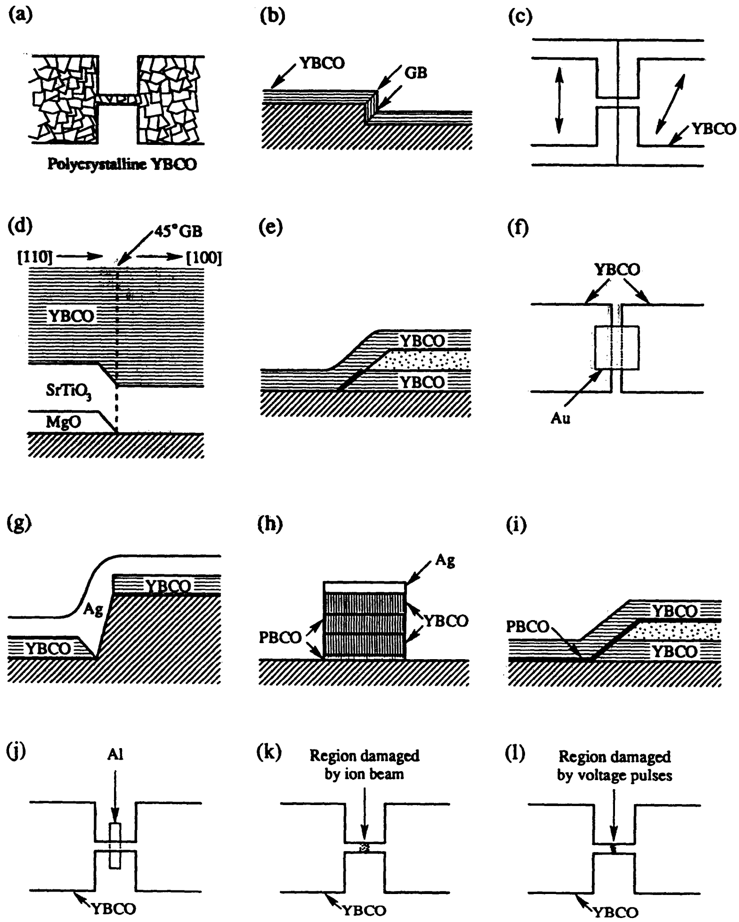

Figure 31. Schematic representation of twelve types of high-T_C thin-film Josephson junction: (a) naturally occurring grain boundary junction [103], (b) step-edge grain boundary (GB) junction [106], (c) bicrystal grain boundary junction (arrows indicate [100] axes) [108], (d) bi-epitaxial grain boundary junction [109], (e) edge junction [110], (f) YBCO-Au-YBCO c-axis junction [111], (g) YBCO-Ag-YBCO a-axis junction [112], (h) trilayer YBCO-PBCO-YBCO junction [115], (i) trilayer YBCO-PBCO-YBCO edge junction [116], (j) poison stripe junction [106], (k) ion beam damage junction [117, 118], (l) electroshocked junction [119].

several grain boundaries that behaved as weak links or Josephson junctions. Subsequently, many groups have made similar junctions, usually by removing regions of the film with acid etching or ion-beam milling, and extended the technique to other materials such as BiSrCaCuO [104] and TlBaCaCuO [105]. Grain boundary junctions with not too high critical current densities often exhibit almost ideal resistively shunted junction behavior. However, they suffer from the drawback that one has little control of their properties and none of their location.

Several techniques have been devised to induce the growth of a grain boundary at a specific location. Simon *et al.* [106] deposited a film across a step etched in a substrate [Fig. 31(b)]. The film was then patterned to form a bridge across the step; provided the step edge is sharp enough, a grain boundary junction is formed at top and bottom. Subsequent transmission electron microscopy at Jülich [107] showed that if the step angle is steeper than 45°, the film has an a-axis orientation on the step, thus forming a grain boundary with each of the c-axis films on either side.

Another widely adopted technique involves bicrystal substrates [108], made by cutting a wedge from a crystal of (100) $SrTiO_3$ and fusing the two pieces together to form a grain boundary between two regions with a known in-plane misorientation [Fig. 31(c)]. When YBCO is deposited with an *in situ* process, the ab-axes mimic the orientation of the substrate, producing a grain boundary. One can pattern microbridges across any part of the grain boundary to produce junctions with relatively predictable characteristics. Related to the bicrystal junction is the bi-epitaxial process [109] [Fig. 31(d)], in which an appropriate seed layer is deposited on the substrate and then selectively removed to leave edges in predetermined locations. One deposits a $SrTiO_3$ buffer layer followed by a YBCO film which undergoes a 45° in-plane re-orientation wherever it crosses the edge of the seed layer. Again, one patterns microbridges across the 45° grain boundaries to form junctions.

In the second group of junctions, we begin with the edge junction [Fig. 31(e)] of Laibowitz *et al.* [110]. These authors first deposited a YBCO film and a (non-epitaxial) insulating layer, and then ion-milled an edge. After exposing this edge to an oxygen-fluorine plasma, they deposited a YBCO film to form an edge junction in which the supercurrent flowed along the ab-planes of the films. Both junctions and SQUIDs have been made with this technique, but the yield and reproducibility are apparently poor.

Making use of the proximity effect, Schwartz *et al.* [111] fabricated a junction by patterning a narrow slit in a YBCO film using electron-beam lithography and depositing a gold film across the slit [Fig. 31(f)]. This junction exhibited supercurrents at temperatures up to 16K. Using a different configuration [Fig. 31(g)], DiIorio *et al.* [112] fabricated proximity effect junctions that exhibited Josephson effects to temperatures well over 77K. A step is milled in a $LaAlO_3$ substrate and a YBCO film is sputtered at an angle to the substrate so as to leave the step edge uncovered. A silver film, deposited immediately afterwards, connects the two films so that currents flow in the ab-plane. Another class of proximity effect junctions, involving PrBaCuO (PBCO) as the barrier was pioneered by Rogers *et al.* [113]. In their early work, they grew a c-axis trilayer of YBCO-PBCO-YBCO, with a PBCO thickness of typically 50nm, and patterned it to form junctions [Fig. 31(h)]. Some of these junctions exhibited a supercurrent at temperatures up to 65K. However, given the weak proximity effect of c-axis films [114], it seems likely that the supercurrent was due to shorts through the PBCO. Subsequently, Barner *et al.* [115] fabricated a -axis trilayers which, after being patterned into junctions, exhibited supercurrents at temperatures as high as 80K. An alternative configuration for a-axis junctions [Fig. 31(i)] was adopted by Gao *et al.* [116] who fabricated edge junctions with PBCO barriers.

The third category contains "weakened" structures. Simon *et al.* [106] deposited a YBCO film across a thin aluminum strip which "poisons" the superconductor locally, thereby reducing its transition temperature [Fig. 31(j)]. In another method [Fig. 31(k)], one reduces the transition temperature of a narrow region by focusing high energy ions [117] onto a microbridge or using a mask patterned with electron-beam lithography [118] to define the area exposed to an ion beam. In a third technique [119], controlled electrical pulses were applied to microbridges at 77K, again producing a weakened region [Fig. 31(ℓ)]. Although these weakening techniques are controllable at least to some degree, they generally lead to flux-flow characteristics (probably because the weakened region is long compared with the coherence length) that are undesirable for most applications. However, if the region weakened by poisoning or ion-bombardment could be reduced to a few tens of nanometers, these techniques might prove to be very useful.

Which of the various junctions look most promising for SQUIDs? To date, the best SQUIDs have been made from step edge grain boundary or bicrystal grain boundary junctions. These structures generally exhibit RSJ-like current-voltage characteristics with I_0R products up to about 200μV at 77K. Resistances vary from the order of 1Ω to as high as 10-20Ω [120]. Although careful fabrication procedures have improved the yield of these junctions, particularly in the case of the bicrystal devices, the scatter in the critical current and resistance remains higher than one would like. There is ongoing work to improve the understanding and reproducibility of trilayer edge junctions with a variety of barrier materials [121] and one might hope to see steady progress in the yield of this class of junction. For the moment, the simplicity offered by the grain boundary junctions, which involve only a single YBCO layer, makes them very appealing for practical applications.

6.2 PREDICTIONS FOR WHITE NOISE

In designing dc SQUIDS for operation at 77K, we should bear in mind not only the constraints on the critical current and inductance, $I_0\Phi_0 2\pi >> k_BT$, but also the requirement that the thermally induced flux noise in the SQUID loop, $<\Phi_N^2>^{1/2} = (k_BTL)^{1/2}$, be much less than one flux quantum. For low-T_c SQUIDs the corresponding upper bound on the inductance, $L << \Phi_0^2/k_BT$, is sufficiently large that it is almost never an important constraint; however, this is not the case at 77K. Although computer simulations of course take into account the effects of thermal noise, a result by Enpuku *et al.* [122] is useful in predicting the reduction in V_Φ that results from the thermal flux noise:

$$V_\Phi = \frac{4I_0R}{\Phi_0(1+\beta)}[1 - (L/L_T)^{1/2}] \quad . \tag{6.1}$$

Here, $L_T \equiv \Phi_0^2/4\pi k_BT$ = 321pH at 77K is a temperature-dependent inductance; Eq. (6.1) is valid for inductances rather less than 321pH. We see that the effects of flux noise can be very significant: for example, for L = 100pH, $(L/L_T)^{1/2} = 0.56$. Thus, there is a good reason to keep L well below 100pH for most applications at 77K. On the other hand, at 4.2K $L_T \approx$ 6nH and since dc SQUIDs typically have inductances of 100-200pH, the flux noise term in Eq. (6.1) is relatively unimportant. For a high-T_c SQUID with an inductance of 50pH and with $\beta = 1$ (I_0 = 20 pA), Eq. (6.1) predicts $V_\Phi \approx 100\mu V/\Phi_0$ for R = 2Ω. Assuming that Eq. (3.8) is approximately valid for the higher value of Γ (0.16), we find $S_\Phi^{1/2} \approx 2\times10^{-6}\Phi_0 Hz^{-1/2}$ and $\varepsilon \approx 2\times10^{-31}$ JHz^{-1}. This noise energy is an order-of-magnitude higher than that expected for low-T_c SQUIDs with comparable parameters operating at 4.2K, reflecting the increase in temperature.

In the case of the rf SQUID, if we use I_0 = 50μA, $LI_0 = 2.5\Phi_0$, $\omega_{rf}/2\pi$ = 30 MHz and T = 77K in Eq. (4.10), we find $\varepsilon \approx 3\times10^{-29}$ JHz^{-1}. This noise energy is not too different from that obtained for typical 20MHz devices operating at 4.2K, where the effective noise temperature T_a^{eff} [Eq. (4.12)] of the room temperature preamplifier and tank circuit is much higher than the bath temperature. When the SQUID is operated at 77K, there is no reason for T_a^{eff} to increase, and the system noise energy should be comparable with that for a 4.2K SQUID. Thus, although at 4.2K dc SQUIDs are clearly superior to rf SQUIDs operating at around 20 MHz, we expect the margin to be narrower for 77K devices.

With regard to l/f noise, one expects both critical current fluctuations and flux noise to contribute. However, it is not possible to make any *a priori* predictions of the magnitude of these contributions.

6.3 DC SQUIDS

I shall give a brief summary of the fabrication and performance of bicrystal SQUIDs at Berkeley; other groups have made similar devices. We deposit the YBCO film on a $10 \times 10 mm^2$ bicrystal $SrTiO_3$ (STO) substrate with a 24° grain boundary using an excimer laser operating at 248nm and a repetition rate of 5Hz. The substrates are maintained at approximately 810°C in 210mTorr of O_2, and the films are grown at 0.05-0.07nm per pulse. Typical film thicknesses are 150-180nm. After completing the deposition we admit 0.8 atm of O_2 to the chamber and cool the substrate to 450°C in 20 min. We then allow it to cool to ambient temperatures in about 30 min. To enable us to make low-resistance electrical contacts to the YBCO film, we transfer the chip from the deposition chamber to an evaporator and deposit roughly 50nm of Ag through a shadow mask on the region of the film where the contact pads will be patterned. We pattern up to 12 SQUIDs on a single chip using conventional photolithography and a 500eV Ar ion mill. The junction width is 1-3μm. Subsequently, 32μm-diameter Al leads are attached to the Ag pads with a wedge bonder.

We measure the noise of the SQUIDs using the flux modulation scheme and flux-locked loop described in Sec. 3.4. The voltage across the SQUID is amplified by a cooled transformer which has a turns ratio of 1:15. The power spectrum of the noise for a relatively low inductance device, with an estimated inductance L of 10pH and measured with a static bias current, is shown in Fig. 32. The SQUID was enclosed in a 40 mm-diameter conetic shield and immersed in liquid nitrogen in a dewar surrounded by three concentric mu-metal shields. The magnetic shielding is not quite sufficient to eliminate the pickup of 60Hz and its odd harmonics, as can be seen in the figure; spikes at lower frequencies are due to microphonics. The flux noise at frequencies above about 5kHz is very low, about $1.5 \mu\Phi_0 \, Hz^{-1/2}$, corresponding to a noise energy of about $5 \times 10^{-31} \, JHz^{-1/2}$. However, at lower frequencies the spectral density increases as l/f, and the rms noise at 1 Hz is an order of magnitude higher than at 5kHz. Also shown in Fig. 32 is the result of operating the SQUID with the bias reversal scheme described in Sec. 3.6. The l/f noise power at 1Hz is reduced by two orders of magnitude, indicating that the l/f noise was produced by critical current fluctuations rather than by the hopping of vortices. Similar reductions in the level of l/f noise have been reported by other authors [123].

Although the magnetic flux noise is very low in this device, its small area implies that the magnetic field noise is high. To obtain low magnetic field noise, we must enhance the effective area. The following two sections are concerned with single and multilayer flux transformers that enhance the sensitivity of the SQUID to magnetic field.

6.4 SINGLE-LAYER MAGNETOMETERS

The directly-coupled magnetometer [124] consists of a single film of YBCO deposited on a bicrystal and patterned in the configuration shown in Fig. 33. A magnetic field B applied to the pickup loop of area A_p and inductance L_p induces a supercurrent $J = BA_p / L_p$ which, in turn, links a flux $\alpha_d LJ$ to the SQUID. Here, α_d is the fraction of the SQUID inductance L to which the current couples. The effective area of the magnetometer is thus

$$A_{eff}^{(d)} = A_s + \alpha_d A_p L / L_p , \tag{6.2}$$

where A_s is the effective area of the bare SQUID. Neglecting A_s and using the estimated values for a particular device, $\alpha_d = 0.8$, $A_p = 47 mm^2$, $L = 20pH$ and $L_p = 11nH$, we find $A_{eff}^{(d)}$

$\approx$ 0.068mm^2. The measured value was somewhat higher, 0.086mm^2. Figure 34(a) shows the magnetic field noise of a directly coupled magnetometer with $I_0 \approx 45\mu A$, $R \approx 3.4\Omega$ and the parameters listed above, operated at 77K in a flux-locked loop with bias reversal. The noise is white at frequencies down to below 1 Hz with the value 93fTHz$^{-1/2}$. This value is listed in Table I.

Subsequently, we increased the effective area of the device by coupling it to a single-layer flux transformer [125] in the configuration of Fig. 35. The smaller loop is inductively coupled to the pickup loop of a directly coupled magnetometer in a flip-chip arrangement in which the two chips are pressed together with a mylar sheet between the YBCO films. We define $\mathcal{A}_i$ and $\mathcal{L}_i$ as the area and inductance of the small input loop, $\mathcal{A}_p$ and $\mathcal{L}_p$ as the area and inductance of the large pickup loop and α' as the coupling coefficient between $\mathcal{L}_i$ and L_p. The effective area is easily shown to be

$$A_{eff}^{(m)} \approx \alpha_d \frac{L}{L_p}\left[A_p + \mathcal{A}_p \frac{\alpha' (L_p \mathcal{L}_i)^{1/2}}{\mathcal{L}_i + \mathcal{L}_p}\right] . \tag{6.3}$$

For the directly coupled magnetometer described above and a transformer with the estimated parameters $\alpha = 0.9$, $\mathcal{L}_i = 10$ nH, $\mathcal{L}_p$ = 85nH, and $\mathcal{A}_p = 1.33\times10^{-3}m^2$, we calculate an estimated effective area $A_{eff}^{(m)} \approx 0.26mm^2$. The measured value was 0.29mm^2, yielding a transformer gain of 3.4. The measured magnetic field noise, shown in Fig. 34(b), is 31fTHz$^{-1/2}$ at 1kHz and 39fTHz$^{-1/2}$ at 1Hz.

Further improvements in the performance of the directly-coupled magnetometer were achieved by Lee *et al.* [120], who made pickup loops with larger linewidths, thereby lowering their inductance. A typical performance is 40fTHz$^{-1/2}$ at 1kHz and 65fTHz$^{-1/2}$ at 1Hz. An even lower noise was achieved by Cantor *et al.* [126] with the aid of a 20x20mm^2 bicrystal and a larger pickup loop: 14fTHz$^{-1/2}$ at 1kHz and 26fTHz$^{-1/2}$ at 1Hz.

6.5 MULTILAYER FABRICATION PROCEDURES

We turn now to a discussion of magnetometers involving multilayers, namely two YBCO films separated by an insulating layer of STO. At specified points it is necessary to open a via in the STO to enable one to make a superconducting connection between the YBCO films. Clearly, each layer has to be patterned separately. The fabrication of multilayer devices is much more demanding than single-layer devices, and for a long period of time patterned multilayers produced relatively high levels of 1/f noise due to the thermally activated hopping of vortices. It is believed that the excess noise arose predominantly from the upper YBCO film which had a poorer crystalline quality than YBCO films deposited directly on a substrate. However, we have recently developed processing techniques that substantially reduce the 1/f noise, and we begin with a brief summary of our current technique [127].

We first deposit a 10nm-thick STO buffer layer on a STO (100) substrate and follow it with a 120nm-thick YBCO film and a 15nm-thick "cap" of STO. The cap plays a crucial role in that it is subject to less damage than a YBCO film during photolithographic patterning. As a result, the subsequent layers of STO and YBCO grow with a higher degree of crystallinity and fewer defects than in the uncapped case. We pattern the first, capped layer with Ar ion milling at a 45° degree of incidence to the rotating substrate, remove the photoresist, and return the chip to the deposition chamber where we deposit 230nm of STO as the insulating layer. We discovered that the quality of this film was sufficiently high to reduce the diffusion of O_2 into the YBCO substantially; as a result, our standard O_2 annealing procedure yielded transition temperatures as low as 40K. To remedy this oxygen deficiency, after depositing the STO film we cool the bilayer over a period of 30 min to

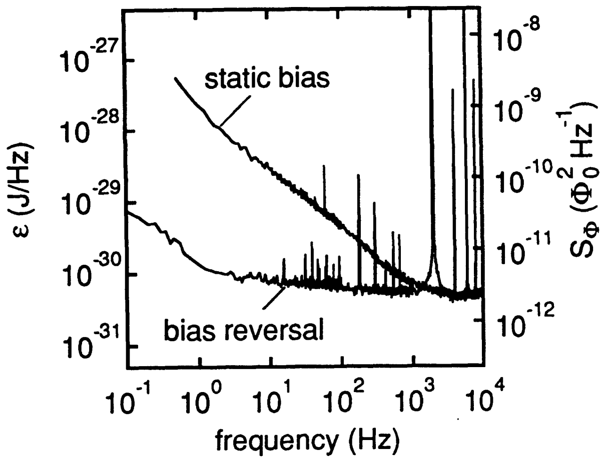

Figure 32. Flux noise spectral density $S_\Phi(f)$ of 10 pH SQUID at 77K with static bias and with bias reversal. Left-hand ordinate shows noise energy $\varepsilon(f) = S_\Phi(f) / 2L$.

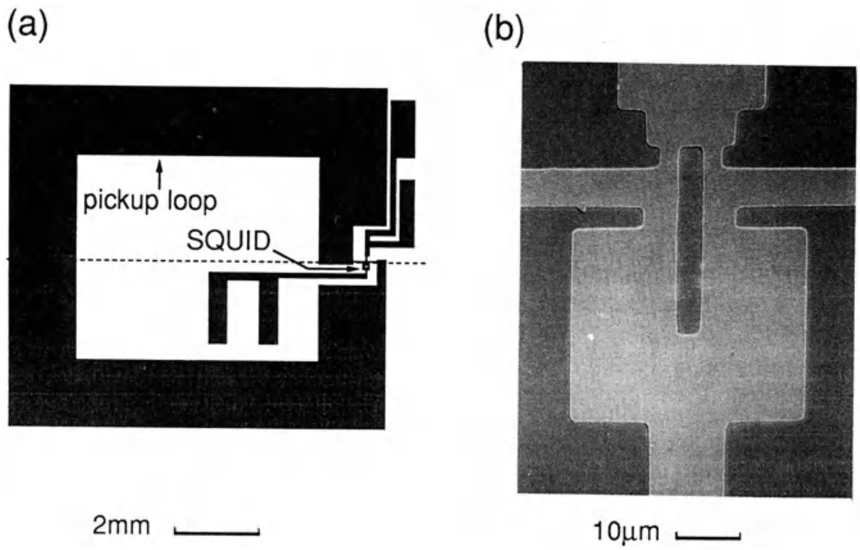

Figure 33. Single-layer magnetometer deposited on 10 x 10mm^2 bicrystal; outer dimensions of pickup loop are 7mm x 8mm. Pickup loop in (a) is connected to the SQUID in (b); square washer is 32μm x 32μm. Dashed line in (b) indicates grain boundary.

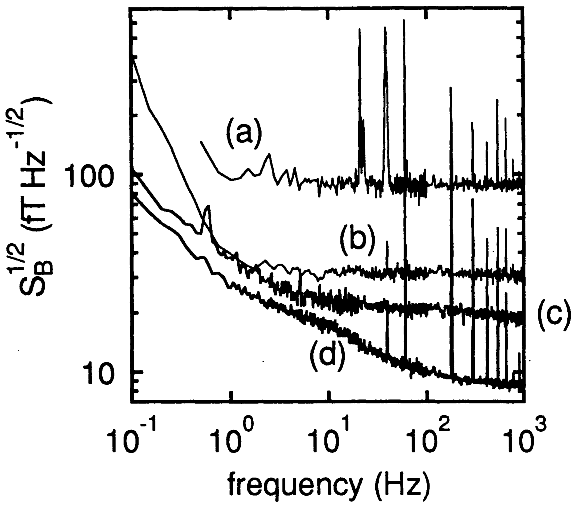

Figure 34. Magnetic field noise of four magnetometers, all operated at 77K with bias reversal: (a) directly coupled magnetometer, (b) directly coupled magnetometer with flip-chip 50 mm flux transformer, (c) fractional turn SQUID, (d) SQUID with flip-chip 16-turn flux transformer.

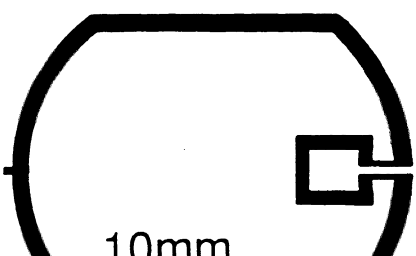

Figure 35. Configuration of single-layer flux transformer. The smaller loop is inductively coupled to a directly coupled magnetometer in a flip-chip arrangement.

500 °C in 0.8 atm of O_2, and maintain this temperature for 3 hours before turning off the heater. Even this protracted annealing step results in a somewhat suppressed transition temperature, typically 85K. We open vias in the STO, again using an Ar ion mill at a 45° angle of incidence and a rotating substrate. In the patterning of both the capped YBCO and STO films the angled ion mill and rotating substrate are important in producing smoothly beveled edges over which subsequent films can grow with relatively high quality. The final, 250nm-thick YBCO film is patterned at a normal angle of incidence on a stationary substrate.

6.6 FRACTIONAL TURN SQUIDs

The configuration of the fractional turn SQUID [128, 129] (multiloop magnetometer) is shown in Fig. 36(a). In the center is a patterned YBCO-STO-YBCO multilayer. Each pickup loop, patterned largely in the upper YBCO film, makes contact with the lower film in the cross-shaded region. The two bicrystal junctions, in series, connect the upper and lower YBCO films. The films are patterned in such a way that no narrow lines other than those forming the two junctions cross the grain boundary.

The effective inductance and area are given by [130]

$$L_{eff} = L_p / N^2 + L_s / N + L_j \tag{6.4}$$

and

$$A_{eff} = A_p / N - A_s \ . \tag{6.5}$$

Here, L_p and A_p are the inductance and area of the large, outer loop, L_s and A_s are the average inductance and area of one spoke of the "cartwheel," L_j is the inductance of the connections from the pickup loops to the junctions, and N is the number of loops. Drung *et al.* [131] have discussed the optimization of the design for operation at 77K, and concluded that the optimum value of N is between 15 and 20 for a device diameter of 7mm. We fabricated two 16-loop devices [shown in Fig. 36(b)], with two bicrystal junctions nominally

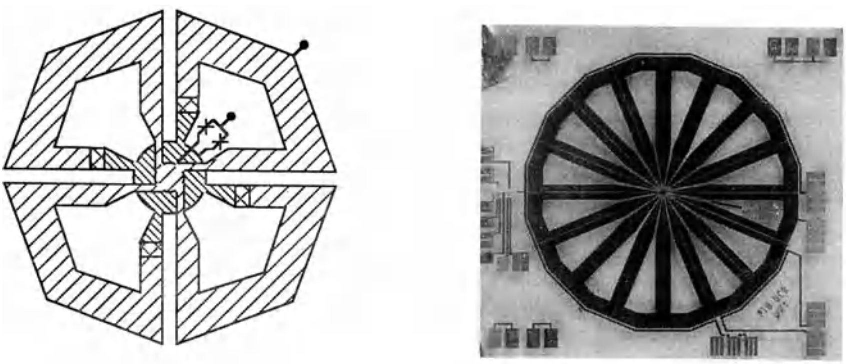

(a) (b)

Figure 36. (a) Schematic layout and (b) photograph of multiloop magnetometer. The 16-loop device in (b) is 7 mm across.

2.5 μm wide in the first YBCO film [132]. For these devices we estimate L_p = 12.2nH, A_p = 34.5 mm^2, L_s = 1.17nH, A_s = 0.39 mm^2 and L_j = 24 pH, yielding an effective inductance of 145pH and an effective area of 1.77mm^2. The measured effective areas were 1.84mm^2 and 1.89mm^2, in good agreement with our estimate. For the better of the two magnetometers the junction resistance R was 10Ω and the critical current I_0 (corrected for thermal noise rounding) was about 13μA. These values give an I_0R product of about 130μV (typical for our process) and $\beta_L = 2LI_0 / \Phi_0 \approx 1.8$.

After measuring the noise of the magnetometers we concluded that there was a non-negligible contribution from the Nyquist noise of the conetic shield. Consequently, we replaced it with a superconducting shield consisting of an yttria stabilized zirconia tube with a length of 125mm and inner and outer diameters of 25mm and 32.5mm, coated on both sides with a thick film of YBCO [133]. The resulting noise of the better magnetometer, plotted in Fig. 34(c), was 18fT $Hz^{-1/2}$ at 1kHz and 37 fT $Hz^{-1/2}$ at 1Hz.

6.7 MULTITURN FLUX TRANSFORMERS

A number of groups have successfully fabricated multilayer flux transformers in which a multiturn coil is inductivley coupled to the SQUID. These magnetometers fall into two classes: in one the transformer and SQUID are fabricated on separate substrates and coupled in a flip-chip arrangement, and in the other the magnetometer is fabricated on a single substrate.

We begin with the flip-chip devices; the configuration of the multiturn flux transformer is shown in Fig. 37(a). The multiturn input coil is inductively coupled to the SQUID, for which two designs are also shown in Fig. 37. The effective area of the magnetometer is given by

$$A_{eff} = A_s + A_p \frac{M_i}{L_i + L_p} , \tag{6.6}$$

where $M_i = \alpha(LL_i)^{1/2}$ is the mutual inductance between the SQUID and the multiturn input coil of inductance L_i. Provided that α does not depend on L_i and that $A_s << A_{eff}$, for a given pickup loop A_{eff} is a maximum when $L_i = L_p$:

$$A_{eff}^{max} = \frac{\alpha}{2} A_p \left(\frac{L}{L_p}\right)^{1/2} . \tag{6.7}$$

For the representative values α = 0.5, A_p = 80mm^2, L = 40pH and L_p = 20nH, we find $A_{eff}^{max} \approx 1\ mm^2$.

In our most recent series of such devices [127, 134, 135] we used 16-turn input coils, generally patterning the pickup loop and input coil in the lower YBCO film and the crossover connecting the innermost turn to the pickup loop in the upper YBCO film. The pickup loop is 10mm on a side with a width of 1 mm, giving an area A_p of about 80mm^2. The input coil lines were 10μm wide with a pitch of 14μm, and the crossovers were 50μm wide. Photographs of the input coil appear in Fig. 38.

We patterned 12 SQUIDs in the two configurations A/A and A/C shown in Figs. 37(b) and (c) [135]. The YBCO film, deposited at Conductus on a 24° STO bicrystal, was 250nm thick. Each SQUID had an outer dimension of 500μm, a slit width of 4μm and junction widths of 1-3μm. The resistance R of each junction ranged from 2.4-8.6Ω. To assemble the magnetometers, we carefully aligned the input coil of the transformer over the SQUID and clamped the two chips together with a 3μm-thick mylar sheet between them. The magnetic field noise of our best magnetometer, with a type A/A SQUID, is shown in Fig. 34(d). At 1kHz the noise is white with a value of 8.5fT $Hz^{-1/2}$, and at 1Hz it is 27fT $Hz^{-1/2}$; at frequencies just above 1Hz the rms noise falls off more slowly than $1/f^{1/2}$, and appears to have a contribution from a random telegraph signal.

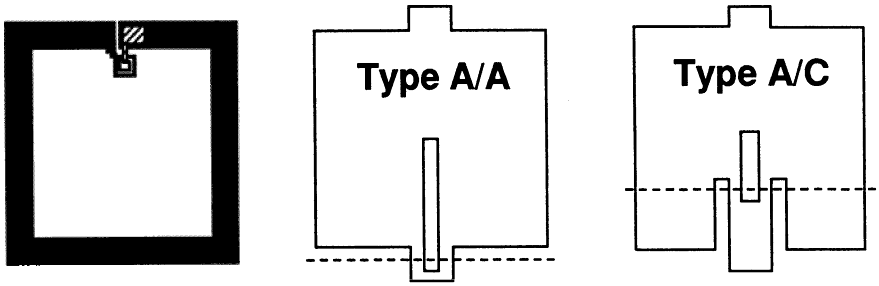

(a) (b) (c)

Figure 37. (a) Configuration of multiturn flux transformer (not to scale). (b) Type A/A SQUID, and (c) type A/C SQUID; each washer is 500μm x 500μm.

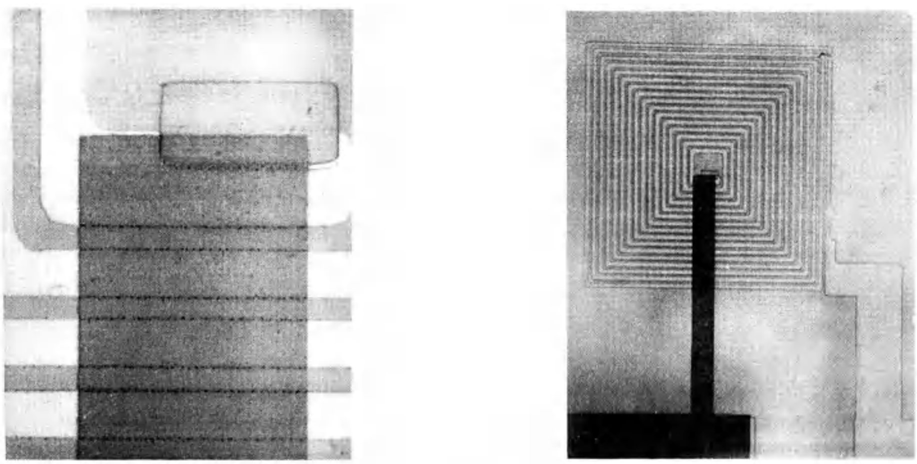

(a) (b)

Figure 38. (a) Photograph of 16-turn input coil of flux transformer, with enlargement of central region shown in (b). Outer dimension of coil is 500μm.

We [134] and several other groups [136-139] have successfully integrated magnetometers in which the SQUID and flux transformer are deposited on the same substrate. The SQUID washer is often used as either a crossunder or a crossover for the flux transformer [140], so that only two superconducting layers are required. The process of manufacturing an integrated device of this kind is more challenging than for flip-chip mangetometers because one has to achieve not only a functioning flux transformer with low levels of flux noise but also junctions with near-optimum parameters. At the time of writing, the most sensitive integrated magetometer of this type was fabricated on a $10 \times 10 mm^2$ bicrystal by Dössel *et al.* [139], and achieved a magnetic field noise of 200fT $Hz^{-1/2}$ at frequencies down to 1Hz. To increase the yield, they used two SQUIDs with two input coils connected to the same pickup loop. One might expect substantial improvements in the performance of integrated devices in the near future.

6.8 RF SQUIDS

Several groups have successfully made rf SQUIDs that operate at 77K; of these, the most sensitive are those of the Jülich group [65, 141, 142], which I briefly describe.

For operation at 150MHz, the SQUIDs were made from YBCO films deposited on $SrTiO_3$ substrates in which shallow pits had been ion milled to produce step-edge junctions. The films were patterned as square washers with inner dimensions (d_1) of $20 \times 20\ \mu m^2$ to $400 \times 400\ \mu m^2$ and outer dimensions (d_2) of $6 \times 6\ mm^2$ to $8 \times 8\ mm^2$. The tank circuit had a Q of 40-60, and the measured values of V_Φ were greater than $40\mu V / \Phi_0$ for 120 pH SQUIDs. The best of these devices, with an inner area less than $100 \times 100\ \mu m^2$, exhibited a white noise of $40\mu\Phi_0\ Hz^{-1/2}$ at frequencies down to 1Hz, corresponding to a noise energy of 5×10^{-29} JHz^{-1}. It is particularly noteworthy that the large outer dimensions of these SQUIDs produces a substantial effective area, $A_{eff} \approx d_1 d_2$, due to the focusing of the externally applied magnetic flux [143], and thus yields a high sensitivity to magnetic fields, $\Phi_N(f) / d_1 d_2$. The best magnetic field sensitivity reported was 170fT $Hz^{-1/2}$ at 1 Hz. Subsequently, Zhang *et al.* [144] coupled an rf SQUID washer with inner and outer dimensions of 0.2mm and 8mm to a flux transformer with a $40 \times 40 mm^2$ pickup loop and achieved a magnetic field noise of 24ftHz-1/2 at frequencies down to 0.5Hz. The rf bias frequency was 150MHz.

The Jülich group have also achieved impressive results with rf SQUIDs operated at microwave frequencies. Zhang *et al.* [142] patterned a YBCO SQUID in the configuration of Fig. 39 and biased it at 3GHz. In an early version, an S-shaped microstrip resonator was

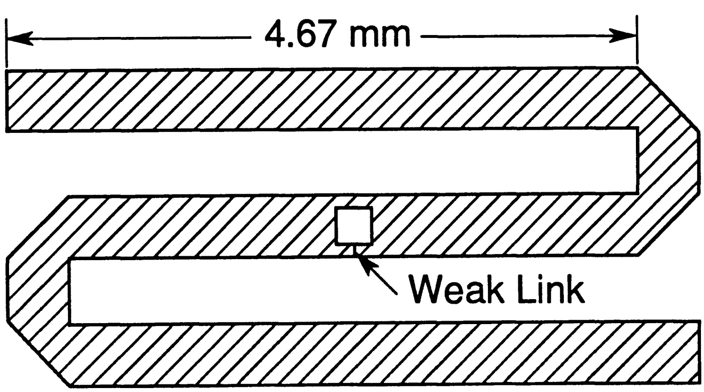

Figure 39. Configuration of microwave SQUID resonator with $100 \times 100 \mu m^2$ hole (re-drawn from ref. [142]).

patterned to contain a 100x100 μm^2 hole with two step-edge junctions along one edge; subsequently, the SQUID area was reduced to 10x100 μm^2, with the longer side parallel to the edge of the resonator. The microstrip configuration, formed by a copper ground plane on the underside of the substrate, was capacitively coupled to a 50Ω coaxial cable leading to the room temperature electronics. For the smaller SQUID, with an estimated inductance of 80 pH, the transfer function was about 100 $\mu V / \Phi_0$ and the flux noise about 1.6×10^{-5} $\Phi_0 Hz^{-1/2}$ at frequencies down to about 0.1 Hz, corresponding to a noise energy of 6.4×10^{-30} JHz^{-1}. The noise energy is about a factor of 8 better than that of the 150 MHz SQUID described earlier. Mück [65] suggests that a factor of two improvement in the noise energy of the microwave SQUID could be achieved with a cooled preamplifier.

The flux-focusing factor of the microwave SQUID was about 8, leading to a magnetic field sensitivity of about 0.5 pT $Hz^{-1/2}$. The geometry of the stripline makes it difficult to achieve substantially higher flux focusing, so that a flux transformer will be necessary to improve the magnetic field sensitivity further.

6.9 MAGNETIC FLUX NOISE

A persistent problem with the high-T_c magnetometers has been the presence of l/f magnetic flux noise at low frequencies. This phenomenon was investigated by Ferrari *et al.* [145, 146] who measured the flux noise generated by high-T_c films in a nearby low-T_c square washer SQUID. The assembly was enclosed in a vacuum can immersed in liquid helium. The SQUID was maintained at 4.2K, while the temperature of the chip could be increased by means of a heater. All films studied exhibited l/f flux noise at temperatures below T_c, with a peak in the noise at T_c. In early polycrystalline YBCO films [145], the noise level was very high -- of the order of 10^{-5} Φ_0^2 Hz^{-1} at 4.2K and 1 Hz -- but the noise has diminished substantially as the quality of the films has improved. For example, in high quality epitaxial YBCO films [146] the noise at 77K is well below 10^{-10} Φ_0^2 Hz^{-1} at 1 Hz. At least in single layer *in situ* films, it is possible to achieve this noise level quite consistently: for example, in the bicrystal SQUID illustrated in Fig. 32, the noise is below 10^{-11} Φ_0^2 Hz^{-1} at 1 Hz.

Using a modified version of the theory presented in Sec. 3.6, Ferrari *et al.* [147] have described the origin of the noise in terms of the motion of flux quanta in the film. Each vortex hops independently between two pinning sites under thermal activation, a process that produces a random telegraph signal with a Lorentzian power spectrum of the form $\tau / (1 + \omega^2\tau^2)$, where $\tau = \tau_0 \exp[-U(T) / k_B T]$ is a characteristic time, τ_0 is an attempt frequency and U(T) is the height of the energy barrier separating the wells. One computes the spectral density of an ensemble of such independent processes by adding the individual Lorentzians; if the distribution of activation energies is broad on the scale of $k_B T$, the result is a l/f power spectrum [147]. The spectral density of the noise increases approximately linearly with the magnetic field in which the sample is cooled.

As mentioned in Sec. 6.5, the levels of l/f noise in multilayer structures have generally been higher than in single-layer films, because of the difficulty in maintaining sufficiently high qualtiy microstructure through several growth processes. Considerable progress has been made, however, and levels of l/f flux noise in (say) three-layer structures will hopefully be reduced to levels approaching the noise of the SQUID before too long. The increase in l/f noise in an ambient magnetic field -- in both single-layer and multilayer devices -- remains an extremely important issue. All of the noise spectra shown in Fig. 34 were obtained in zero field, and the l/f noise is appreciably higher when the devices are operated in magnetic fields comparable with that of the earth. It may be hoped that the ever-improving quality of YBCO films will lead to a reduction in l/f noise not only in zero magnetic field but also in fields of (say) 100μT. For the moment, one solution for biomagnetic measurements is to operate the magnetometers in a magnetically shielded room, as is currently the practice for low-T_c instruments. Of course, for geophysical measurements, this solution is not applicable.

An important alternative suggested by Koch *et al.* [148] is to cool the magnetometer in zero field and then to move it into the earth's magnetic field with a "flux dam" (weak link) in the pickup loop to limit the supercurrents induced and thus inhibit the entry of magnetic flux into the material. More work on the crucial issue of low-frequency noise in static magnetic fields is very much in order.

7. Concluding Remarks

Progress with high-T_c SQUIDs in the three years since the 1992 NATO ASI has been very impressive. We now have high-T_c multilayer magnetometers with $10x10mm^2$ pickup loops operating in liquid nitrogen achieving white noise levels of less than $10fTHz^{-1/2}$ and below $30fTHz^{-1/2}$ at 1Hz. A single-layer device on a $20x20mm^2$ bicrystal has achieved $14fTHz^{-1/2}$ at 1kHz and $26fTHz^{-1/2}$ at 1Hz -- and is readily available commercially. These performances compare favorably with those for commercially available low-T_c SQUIDs not so many years ago. It is important to appreciate that a substantial number of groups worldwide have successfully fabricated high-T_c magnetometers with good performance, and there is every reason to believe they will become widely used in the next two or three years. For applications requiring high sensitivity in a small area -- notably arrays of magnetometers for biomagnetic measurements -- it is likely that multilayer devices will be preferred. On the other hand, in applications involving a relatively small number of magnetometers, for example, in geophysics or nondestructive evaluation -- single-layer devices are likely to be perfectly adequate.

High-T_c SQUIDs are already beginning to make their way into a variety of applications. Miklich *et al.* [149] made a picovoltmeter by inductively coupling a 2-turn YBCO coil (patterned in a single-layer) to the pickup loop of a directly-coupled magnetometer. The coil is connected in series with a resistor and the voltage source to be measured. Dantsker *et al.* [150] constructed a 3-axis geophysical magnetometer involving directly-coupled magnetometers, and demonstrated that it functioned in the field. In a quite different application, Black *et al.* [151] used a high-T_c SQUID in a scanning mode to image a variety of objects, including the simulation of a crack induced in the underside of Al sheets by a rivet. A number of groups have obtained high quality magnetocardiograms. The most ambitious system to date is the 16-channel system operated at the Superconducting Sensor Laboratory in Japan [152]. Operating in a tiny shielded room just sufficient to accommodate a person, this system successfully recorded 16 channels of data.

Of course, challenges remain. One of the most important issues is the increase in the 1/f flux noise in YBCO films operated in the earth's magnetic field. Hopefully, the continuing improvements in the quality of films will ameliorate this problem. Also, the reproducibility of Josephson junctions is still not as good as any of us would like. Now that high-T_c SQUIDs have white noise levels close to the predicted values, a factor-of-two departure from the design values of critical current or resistance can cause a significant deterioration in performance. Such variation in parameters means that the yield in fully integrated magnetometers with high performance is less than that with flip-chip magnetometers, where one can select the best SQUID from a set fabricated on a single chip. However, I have no doubt that continuing refinements of the fabrication process will improve the margins of junction critical current and resistance quite substantially.

Thus, I believe that we are about to enter a new era of SQUID applications brought about by the use of liquid nitrogen. Liquid nitrogen is of course appreciably cheaper than liquid helium, but more importantly it boils away much more slowly. As a result, one can readily achieve operating times of many months with a dewar that is still readily portable, or operate a system the size of a coffee can for at least a day. Not to be overlooked is the fact that SQUIDs at 77K can be operated significantly closer to objects at room temperature and pressure than helium temperature devices. This may have interesting consequences for both biology and nondestructive evaluation. I believe that the next few years will see the most explosive growth ever in the use of SQUIDs -- not only high-T_c devices but also low-T_c devices as multi-channel systems have an increasing impact on biomedical measurements.

Acknowledgments

I am indebted to A. Barfknecht for supplying Fig. 7, D. Crum Fig. 22(a), W. J. Gallagher Fig. 22(b), P.F. Michelson Fig. 28, D. Paulsen Fig. 19, and F. C. Wellstood Fig. 10. For that part of the work carried out at Berkeley, I wish to thank the following for their hard work and dedication: Mark Colclough, Gene Dantsker, Gordon Donaldson, Non Fan, Mark Ferrari, Tom Gamble, Wolf Goubau, Erwin Hahn, Mike Heaney, Claude Hilbert, Christoph Heiden, Martin Hürlimann, Mark Johnson, Mark Ketchen, Jack Kingston, Reinhold Kleiner, Roger Koch, Dieter Koelle, Rasmus Kromann, Philippe Lerch, Frank Ludwig, John Martinis, Andy Miklich, David Nemeth, Charles Pennington, Alex Pines, Du Quan, Didier Robbes, Bonaventura Savo, Tim Shaw, Tycho Sleator, Claudia Tesche, Cristian Urbina, Dale Van Harlingen and Fred Wellstood.

This work was supported by the Director, Office of Energy Research, Office of Basic Energy Sciences, Materials Sciences Division of the U.S. Department of Energy under contract number DE-AC03-76SF00098.

General References

I draw the readers' attention to the comprehensive reviews:

Ryhänsen, T., Seppä, H., Ilmoniemi, R., and Knuutila, J. (1989) SQUID magnetometers for low-frequency applications', *J. Low Temp. Phys.* **76**, 287-386,

Hämäläinen, M., Hari, R., Ilmoniemi, J., Knuutila, J., Lounasmaa, O.V. (1993) Magnetoencephalography-theory, instrumentation, and applications to noninvasive studies of the working human brain, *Rev. Mod. Phys.* **65**, 413-497,

and to the recent book containing 7 chapters by different authors:

Barone, A. (ed.) (1992) *Principles and Applications of Superconducting Quantum Interference Devices*, World Scientific Publishing Company, Singapore.

References

1. London, F. (1950) *Superfluids*, Wiley, New York .
2. Josephson, B. D. (1962) Possible new effects in superconductive tunneling, *Phys. Lett.* **1**, 251-253; Supercurrents through barriers, (1965) *Adv. Phys.* **14**, 419-451.
3. Jaklevic, R. C., Lambe, J., Silver, A. H., and Mercereau, J. E. (1964) Quantum interference effects in Josephson tunneling, *Phys. Rev Lett.* **12**, 159-160.
4. Zimmerman, J. E., Thiene, P., and Harding. J. T. (1970) Design and operation of stable rf-biased superconducting point-contact quantum devices, and a note on the properties of perfectly clean metal contacts, *J. Appl. Phys.* **41**, 1572-1580.
5. Mercereau, J. E. (1970) Superconducting magnetometers, *Rev. Phys. Appl.* **5**. 13-20; Nisenoff. M. (1970) Superconducting magnetometers with sensitivities approaching 10^{-10} gauss, *Rev. Phys. Appl.* **5**, 21-24.
6. Clarke, J. (1993) SQUIDs: theory and practice, in H. Weinstock and R. W. Ralston (eds.), *The New Superconducting Electronics*, Kluwer Academic Publishers, Dordrecht, pp. 123-180.
7. Stewart, W. C. (1968) Current-voltage characteristics of Josephson junctions, *Appl. Phys. Lett.* **12**, 277-280.
8. McCumber, D. E. (1968) Effect of ac impedance on dc voltage-current characteristics

of Josephson junctions, *J. Appl. Phys.* **39**, 3113-3118 .
9. Ambegaokar, V. and Halperin, B. I. (1969) Voltage due to thermal noise in the dc Josephson effect, *Phys. Rev. Lett.* **22**, 1364-1366.
10. Clarke, J. and Koch, R. H. (1988) The impact of high-temperature superconductivity on SQUIDs, *Science* **242**, 217-223.
11. Likharev, K. K. and Semenov, V. K. (1972) Fluctuation spectrum in superconducting point junctions, *Pis'ma Zh. Eksp. Teor. Fiz.* **15**, 625-629. [(1972) *JETP Lett.* **15**, 442-445].
12. Vystavkin, A. N., Gubankov, V. N., Kuzmin, L. S., Likharev, K. K., Migulin, V. V., and Semenov, V. K. (1974) S-c-s junctions as nonlinear elements of microwave receiving devices, *Phys. Rev. Appl.* **9**, 79-109.
13. Koch, R. H., Van Harlingen, D. J., and Clarke, J. (1980) Quantum noise theory for the resistively shunted Josephson junction, *Phys. Rev Lett.* **45**, 2132-2135.
14. Tesche, C. D. and Clarke. J. (1977) dc SQUID: noise and optimization *J. Low. Temp. Phys.* **27**, 301-331.
15. Bruines, J. J.P., de Waal, V. J., and Mooij, J. E. (1982) Comment on DC SQUID noise and optimization, by Tesche and Clarke *J. Low. Temp. Phys.* **46**, 383-386.
16. De Waal, V. J., Schrijner, P., and Llurba, R. (1984) Simulation and optimization of a dc SQUID with finite capacitance, *J. Low. Temp. Phys.* **54**, 215-232.
17. Ketchen, M. B., and Jaycox, J. M. (1982) Ultra-low noise tunnel junction dc SQUID with a tightly coupled planar input coil, *Appl. Phys. Lett.* **40**, 736-738.
18. Jaycox, J. M. and Ketchen, M. B. (1981) Planar coupling scheme for ultra low noise dc SQUIDs, *IEEE Trans. Magn.*, **MAG-17**, 400-403.
19. Barfknecht, A., Colclough, M. S., and de la Cruz, A. Conductus, Inc., Sunnyvale, California (unpublished).
20. Gurvitch, M., Washington, M. A., and Huggins, H. A. (1983) High quality refactory Josephson tunnel junction utilizing thin aluminum layers, *Appl. Phys. Lett.* **42**, 472-474.
21. De Waal, V. J., Klapwijk, T. M., and Van den Hamer, P. (1983) High performance dc SQUIDs with submicrometer niobium Josephson junctions, *J. Low. Temp. Phys.* **53**, 287-312 .
22. Tesche, C. D., Brown, K. H., Callegari, A. C., Chen, M. M., Greiner, J. H., Jones, H. C., Ketchen, M. B., Kim, K. K., Kleinsasser, A. W., Notarys, H. A., Proto, G., Wang, R. H., and Yogi, T. (1985) Practical dc SQUIDs with extremely low 1/f noise, *IEEE Trans. Magn.* **MAG-21**, 1032-1035.
23. Pegrum, C. M., Hutson, D., Donaldson, G. B., and Tugwell, A. (1985) DC SQUIDs with planar input coils, *ibid*, 1036-1039.
24. Noguchi, T., Ohkawa, N., and Hamanaka, K. (1985) Tunnel junction dc SQUID with a planar input coil, in H. D. Hahlbohm. and H. Lubbig (eds.), *SQUID 85 Superconducting Quantum Interference Devices and their Applications*, Walter de Gruyter, Berlin, pp. 761-766.
25. Foglietti, V., Gallagher, W. J., Ketchen, M. B., Kleinsasser, A. W., Koch, R. H., and Sandstrom, R. L., (1989) Performance of dc SQUIDs with resistively shunted inductance, *Appl. Phys. Lett.* **55**, 1451-1453.
26. Muhlfelder. B., Beall. J. A., Cromar, M. W., and Ono, R. H. (1986) Very low noise tightly coupled dc SQUID amplifiers, *Appl. Phys. Lett.* **49**, 1118-1120.
27. Knuutila, J., Kajola, N., Seppä, H., Mutikainen, R., and Salmi. J. (1988) Design, optimization and construction of a dc SQUID with complete flux transformer circuits, *J. Low. Temp. Phys.* **71**, 369-392.
28. Wellstood, F. C., Heiden. C., and Clarke. J. (1984) Integrated dc SQUID magnetometer with high slew rate, *Rev. Sci. Inst.* **55**, 952-957.
29. Carelli, P. and Foglietti, V. (1982) Behavior of a multiloop dc superconducting

quantum interference device, *J. Appl. Phys.* **53**, 7592-7598.

30. Ketchen, M. B., Stawiasz, K. G., Pearson, D. J., Brunner, T. A. Hu, C-K, Jaso, M. A., Manny, M. P., Parsons, A. A., and Stein, K. J. (1992) Submicron linewidth input coils for low T_c integrated thin-film dc superconducting quantum interference devices, *Appl. Phys. Lett.* **61**, 336-338.
31. Clarke. J., Goubau, W. M., and Ketchen. M. B. (1976) Tunnel junction dc SQUID: fabrication, operation, and performance, *J. Low. Temp. Phys.* **25**, 99-144.
32. Ketchen, M. B., Goubau, W. M., Clarke, J., and Donaldson, G.B. (1978) Superconducting thin-film gradiometer, *J. Appl. Phys.* **44**, 4111-4116.
33. Wellstood, F.C., and Clarke, J. unpublished.
34. Wellstood, F. C., Urbina, C., and Clarke, J. (1987) Low-frequency noise in dc superconducting quantum interference devices below 1K, *Appl. Phys. Lett.* **50**, 772-774.
35. Roukes, M. L., Freeman, M. R., Germain, R. S., Richardson, R. C., and Ketchen, M. B. (1985) Hot electrons and energy transport in metals at millikelvin temperatures, *Phys. Rev. Lett.* **55**, 422-425.
36. Wellstood, F. C., Urbina, C., and Clarke, J. (1989) Hot-electron limitation to the sensitivity of the dc superconducting quantum interference device, *Appl. Phys. Lett.* **54**, 2599-2601.
37. Ketchen, M. B., Awschalom, D. D., Gallagher, W. J., Kleinsasser, A. W., Sandstrom, R. L., Rozen, J. R., and Bumble, B. (1989) Design, fabrication and performance of integrated miniature SQUID susceptometers, *IEEE Trans. Magn.* **MAG-25**, 1212-1215.
38. Koch, R. H., Clarke, J., Goubau, W. M., Martinis, J. M., Pegrum, C. M. and Van Harlingen, D. J. (1983) Flicker (l/f) noise in tunnel junction dc SQUIDs, *J. Low. Temp. Phys.* **51**, 207-224.
39. Rogers, C.T. and Buhrman, R.A. (1984) Composition of l/f noise in metal-insulator-metal tunnel junctions, *Phys. Rev. Lett.* 53, 1272-1275.
40. Dutta, P. and Horn, P.M. (1981) Low-frequency fluctuations in solids: l/f noise, *Rev. Mod. Phys.* **53**, 497-516.
41. Savo, B., Wellstood, F. C. and Clarke. J. (1987) Low-frequency excess noise in Nb-Al_2O_3-Nb Josephson tunnel junction, *Appl. Phys. Lett.* **50**, 1757-1759.
42. Tesche, C. D., Brown, R. H., Callegari, A. C., Chen, M. M., Greiner, J. H., Jones, H. C., Ketchen, M. B., Kim, K. K., Kleinsasser, A. W., Notarys, H. A., Proto, G., Wang, R. H. and Yogi. T. (1984) Well-coupled dc SQUID with extremely low l/f noise, in U. Eckern, A. Schmid, W. Weber, H. Wühl (eds.), *Proc. 17th International Conference on low temperature physics LT-17*, North Holland, Amsterdam, pp. 263-264.
43. Foglietti, V, Gallagher, W. J., Ketchen, M. B., Kleinsasser, A. W., Koch, R. H., Raider, S. I. and Sandstrom, R. L. (1986) Low-frequency noise in low l/f noise dc SQUIDs, *Appl. Phys. Lett.* **49**, 1393-1395.
44. Biomagnetic Technologies, Inc. 9727 Pacific Heights Blvd., San Diego, CA 92121-3719.
45. Fujimaki, N., Tamura, H., Imamura, T. and Hasuo, S. A single-chip SQUID magnetometer, Digest of Tech. papers of 1988 International Solid-State conference, (ISSCC), San Francisco, pp. 40-41.
46. Drung, D. (1986) Digital feedback loops for dc SQUIDs, *Cryogenics* **26**, 623-627; Drung, D., Crocoll, E., Herwig, R., Neuhaus, M. and Jutzi, W. (1989) Measured performance parameters of gradiometers with digital output, *IEEE Trans. Magn.* **MAG-25**, 1034-1037.
47. Mück, M. and Heiden, C. (1989) Simple dc SQUID system based on a frequency modulated relaxation oscillator, *IEEE Trans. Magn.* **MAG-25**, 1151-1153.
48. Drung, D., (1991) Investigation of a double-loop dc SQUID magnetometer with

additional positive feedback, in H. Koch and H. Lübbig (eds.), *Superconducting Devices and their Applications*, Springer-Verlag, Berlin, pp. 351-356.

49. Seppä, H. (1991) DC SQUID electronics based on adaptive noise cancellation and a high open-loop gain controller, in H. Koch and H. Lübbig (eds.) *Superconducting Devices and their Applications*, Springer-Verlag, Berlin, pp. 346-350.
50. Clarke, J. (1977) Superconducting QUantum Interference Devices for low frequency measurements' in B. B. Schwartz. and S. Foner. (eds.), *Superconductor Applications : SQUIDs and Machines*, Plenum, New York, pp 67-124.
51. Giffard, R. P., Webb, R. A. and Wheatley, J. C. (1972) Principles and methods of low-frequency electric and magnetic measurements using rf-biased point-contact superconducting device, *J. Low. Temp. Phys.* **6**, 533-610.
52. Kurkijärvi, J. (1972) Intrinsic fluctuations in a superconducting ring closed with a Josephson junction, *Phys. Rev.* **B 6**, 832-835.
53. Kurkijärvi, J. and Webb, W. W. (1972) Thermal fluctuation noise in a superconducting flux detector, in H. M. Long and W. F. Gauster (eds.), *Proc. Applied Superconductivity Conference*, Annapolis, MD, pp. 581-587.
54. Jackel, L.D. and Buhrman, R.A. (1975) Noise in the rf SQUID, *J. Low. Temp. Phys.* **19**, 201-246.
55. Ehnholm, G. J. (1977) Complete linear equivalent circuit for the SQUID, in H. D. Hahlbohm and H. Lubbig (eds.), *SQUID Superconducting Quantum Interference Devices and their Applications*, Walter de Gruyter, Berlin, pp. 485-499; Theory of the signal transfer and noise properties of the rf SQUID, *J. Low. Temp. Phys.* 29, 1-27 (1977).
56. Hollenhorst, H. N. and Giffard, R. P. (1980) Input noise in the hysteretic rf SQUID: theory and experiment, *J. Appl. Phys.* **51**, 1719-1725.
57. Kurkijärvi, J. (1973) Noise in the superconducting flux detector, *J. Appl. Phys.* **44**, 3729-3733.
58. Giffard, R. P., Gallop, J. C. and Petley, B. N. (1976) Applications of the Josephson effects, *Prog. Quant. Electron* **4**, 301-402.
59. Ehnholm, G. J., Islander, S. T., Ostman, P. and Rantala, B. (1978) Measurements of SQUID equivalent circuit parameters, *J. de Physique* **39**, colloque C6. 1206-1207.
60. Giffard, R. P. and Hollenhorst, J. N. (1978) Measurement of forward and reverse signal transfer coefficients for an rf-biased SQUID, *Appl. Phys. Lett.* **32**, 767-769.
61. Jackel, L. D., Webb, W. W., Lukens, J. E. and Pei, S. S. (1974) Measurement of the probability distribution of thermally excited fluxoid quantum transitions in a superconducting ring closed by a Josephson junction, *Phys. Rev.* B9, 115-118.
62. Long, A., Clark, T. D., Prance.,R. J. and Richards, M. G. (1979) High performance UHF SQUID magnetometer, *Rev. Sci. Instrum.* **50**, 1376-1381.
63. Hollenhorst, J. N. and Giffard, R. P. (1979) High sensitivity microwave SQUID, *IEEE Trans. Magn.* **MAG-15**, 474-477.
64. Ahola, H., Ehnholm, G. H., Rantala, B. and Ostman, P. (1978) Cryogenic GaAs-FET amplifiers for SQUIDs, *J. de Physique* 39, colloque C6, 1184-1185; Cryogenic GaAs-FET amplifiers for SQUIDs, (1979) *J. Low Temp. Phys.* **35**, 313–328.
65. Mück, Michael (1993) Progress in rf-SQUIDs, *IEEE Trans. Appl. Supercond.* **3**, 2003-2010.
66. Zimmerman, J. E. (1971) Sensitivity enhancement of Superconducting Quantum Interference Devices through the use of fractional-turn loops, *J. Appl. Phys.* **42**, 4483-4487.
67. Shoenberg, D. (1962) Superconductivity, Cambridge University Press, Cambridge.
68. For a review, see Clarke, J. (1983) Geophysical Applications of SQUIDs, *IEEE Trans. Magn.* **MAG-19**, 288-294.
69. De Waal, V. J. and Klapwijk, T. M. (1982) Compact Integrated dc SQUID gradiometer,

Appl. Phys. Lett. **41**, 669-671.

70. Van Nieuwenhuyzen, G. J. and de Waal, V. J. (1985) Second order gradiometer and dc SQUID integrated on a planar substrate, *Appl. Phy. Lett.* **46**, 439-441.
71. Carelli, P. and Foglietti, V. (1983) A second derivative gradiometer integrated with a dc superconducting interferometer, *J. Appl. Phys.* **54**, 6065-6067.
72. Koch, R. H., Ketchen, M. B., Gallagher, W. J., Sandstrom, R. L., Kleinsasser, A. W., Gambrel, D. R., Field, T. H., and Matz, H. (1991) Magnetic hysteresis in integrated low-T_c SQUID gradiometers, *Appl. Phys. Lett.* **58**, 1786-1789.
73. Knuutila, J., Kajola, M., Mutikainen, R., Salmi, J. (1987) Integrated planar dc SQUID magnetometers for multichannel neuromagnetic measurements, *Proc. ISEC '87* pp. 261.
74. Hoenig, H. E., Daalmans, G. M., Bär, L. Bömmel, F., Paulus, A., Uhl, D., Weisse, H. J., Schneider, S., Seifert, H., Reichenberger, H., Abraham-Fuchs, K., (1991) Multichannel dc SQUID sensor array for biomagnetic applications, *IEEE Trans. Magn.* **MAG-27**, 2777-2785.
75. For reviews, see Romani, G. L., Williamson, S. J. and Kaufman, L. (1982) Biomagnetic instrumentation, *Rev. Sci. Instrum.* **53**, 1815-1845; Buchanan, D. S., Paulson, D. and Williamson, S. J. Instrumentation for clinical applications of neuromagnetism, *Adv. Cryo. Eng.* **33**, 97-106.
76. Neuromag, Helsinki, Finland.
77. Barth, D. S., Sutherling. W., Engel. J. Jr. and Beatty J. (1984) Neuromagnetic evidence of spatially distributed sources underlying epileptiform spikes in the human brain, *Science* **223**, 293-296.
78. Romani, G. L., Williamson, S. J. and Kaufman, L. (1982) Tonotopic organization of the human auditory cortex, *Science* **216**, 1339-1340.
79. Cabrera, B. (1982) First results from a superconductive detector for moving magnetic monopoles, *Phys. Rev. Lett.* **48**, 1378-1381.
80. Quantum Design, San Diego, CA and Conductus, Inc., Sunnyvale, CA.
81. Ketchen, M. B., Kopley, T. and Ling, H. (1984) Minature SQUID susceptometer, *Appl Phys. Lett.* **44**, 1008-1010.
82. Awschalom, D. D. and Warnock, J. (1989) Picosecond magnetic spectroscopy with integrated dc SQUIDs, *IEEE Trans. Magn.* **MAG-25**, 1186-1192.
83. Clarke, J. (1966) A superconducting galvanometer employing Josephson tunneling, *Phil. Mag.* **13**, 115-127.
84. Hilbert, C. and Clarke, J. (1985) DC SQUIDs as radiofrequency amplifiers, *J. Low Temp. Phys.* **61**, 263-280.
85. Tesche, C. D. and Clarke, J. (1979) DC SQUID: current noise, *J. Low Temp. Phys.* **37**, 397-403.
86. Hilbert, C. and Clarke, J. (1985) Measurements of the dynamic input impedance of a dc SQUID, *J. Low Temp. Phys.* **61**, 237-262.
87. Martinis, J. M. and Clarke, J. (1985) Signal and noise theory for the dc SQUID, *J. Low Temp. Phys.* **61**, 227-236, and references therein.
88. Koch, R.H., Van Harlingen, D. J. and Clarke, J. (1981) Quantum noise theory for the dc SQUID, *Appl. Phys. Lett.* **38**, 380-382.
89. Danilov, V. V., Likharev, K. K. and Zorin, A. B.(1983) Quantum noise in SQUIDs, *IEEE Trans. Magn.* **MAG-19**, 572-575.
90. Hilbert, C., Clarke, J., Sleator, T. and Hahn, E. L. (1985) Nuclear quadruple resonance detected at 30MHz with a dc superconducting quantum interference device, *Appl. Phys. Lett.* **47**, 637-639. (See references therein for earlier work on NMR with SQUIDS).
91. Fan, N. Q., Heaney, M.B., Clarke, J., Newitt, D., Wald, L. L., Hahn, E. L., Bielecke, A. and Pines, A.(1989) Nuclear magnetic resonance with dc SQUID preamplifiers, *IEEE*

Trans. Magn. **MAG-25**, 1193-1199.
92. Sleator, T., Hahn, E. L., Heaney, M.B., Hilbert, C. and Clarke, J. (1986) Nuclear electric quadrupole induction of atomic polarization, *Phys. Rev. Lett.* **57**, 2756-2759.
93. Sleator, T., Hahn, E. L., Hilbert, C. and Clarke, J. (1987) Nuclear-spin noise and spontaneous emission, *Phys. Rev. B.* **36**, 1969-1980.
94. Fan, N. Q. and Clarke, J. (1991) Low-frequency nuclear magnetic resonance and nuclear quadrupole resonance spectrometer based on a dc superconducting quantum interference device, *Rev. Sci. Instrum.* **62**, 1453-1459.
95. Hürlimann, M.D., Pennington, C.H., Fan, N.Q., Clarke, J., Pines, A., and Hahn, E. L. (1992) Pulsed fourier-transform NQR of ^{14}N with a dc SQUID, *Phys. Rev. Lett.* **69**, 684-687.
96. For an elementary review on gravity waves, see Shapiro, S. L., Stark, R.F. and Teukolsky, S. J. (1985) The search for gravitational waves, *Am. Sci.* **73**, 248-257.
97. For a review on gravity-wave antennae, see Michelson, P. F., Price, J. C. and Taber, R. C. (1987) Resonant-mass detectors of gravitational radiation, *Science* **237**, 150-157.
98. Paik, H. J. (1981) Superconducting tensor gravity gradiometer with SQUID readout, in H. Weinstock and W. C. Overton, Jr. (eds.), *SQUID Applications to Geophysics*, Soc. of Exploration Geophysicists, Tulsa, Oklahoma, pp. 3-12.
99. Mapoles, E. (1972) A superconducting gravity gradiometer, in H. Weinstock and W. C. Overton, Jr. (eds.), *SQUID Applications to Geophysics*, Soc. of Exploration Geophysicists, Tulsa, Oklahoma, pp. 153-157.
100. For a review, see K. Vozoff, (1972) The Magnetotelluric Method in the Exploration of Sedimentary Basins, *Geophysics* **37**, 98-114.
101. Gamble, T. D., Goubau, W. M., and Clarke, J. (1979) Magnetotellurics with a Remote Magnetic Reference, *Geophysics* **44**, 53-68.
102. Gamble, T. D., Goubau, W. M., and Clarke, J. (1979) Error Analysis for Remote Reference Magnetotellurics, *Geophysics* **44**, 959-968.
103. Koch, R. H., Umbach, C. P., Clark, G. J., Chaudhari, P., and Laibowitz, R. B. (1987) Quantum interference devices made from superconducting oxide thin films, *Appl. Phys. Lett.* **51**, 200-202.
104. Face, D. W., Graybeal, J. M., Orlando, T. P., and Rudman, D. A. (1990) Noise and dc characteristics of thin-film Bi-Sr-Ca-Cu-oxide dc SQUIDs, *Appl. Phys. Lett.* **56**, 1493-1495.
105. Koch, R. H., Gallagher, W. J., Bumble, B., and Lee, W. Y. (1989) Low-noise thin-film TlBaCaCuO dc SQUIDs operated at 77K, *Appl. Phys. Lett.* **54**, 951-953.
106. Simon, R. W., Bulman, J. B., Burch, J. F., Coons, S. B., Daly, K. P., Dozier, W. D., Hu, R., Lee, A. E., Luine, J. A., Platt, C. E., Schwarzbek, S. M., Wire, M. S., and Zani, M. J. (1991) Engineered HTS microbridges, *IEEE Trans. Magn.* **MAG-27**, 3209-3214.
107. Jia, C. L., Kabius, B., Urban, K., Herrman, K., Cui, G. J., Schubert, J., Zander, W., Braginski, A. I., and Heiden, C. (1991) Microstructure of epitaxial $YBa_2Cu_3O_7$ films on step-edge $SrTiO_3$ substrates, *Physica C* **175**, 545-554.
108. Dimos, D., Chaudhari, P., Mannhart, J., and LeGoues, F. K. (1988) Orientation dependence of grain-boundary critical currents in $YBa_2Cu_3O_{7-\delta}$ bicrystals, *Phys. Rev. Lett.* **61**, 219-222.
109. Char, K., Colclough, M. S., Garrison, S. M., Newman, N., and Zaharchuk, G. (1991) Bi-epitaxial grain boundary junctions in $YBa_2Cu_3O_7$, *Appl. Phys. Lett.* **59**, 733-735.
110. Laibowitz, R. B., Koch, R. H., Gupta, A., Koren, G., Gallagher, W. J., Foglietti, V., Oh, B., and Viggiano, J. M. (1990) All high-T_c edge junctions and SQUIDs, *Appl. Phys. Lett.* **56**, 686-688.
111. Schwarz, D. B., Mankiewich, P. M., Howard, R. E., Jackel, L. D., Straughn, B. L., Burhat, E. G., and Dayem, A. H. (1989) The observation of the ac Josephson effect in a $Yba_2Cu_3O_7$/Au/$Yba_2Cu_3O_7$ junction, *IEEE Trans. Magn.* **MAG-25**, 1298-1300.

112. DiIorio, M. S., Yoshizumi, S. Yang, K-Y, Yang, J., and Maung, M. (1991) Practical high-T_c Josephson junctions and dc SQUIDs operating above 85K, *Appl. Phys. Lett.* **58**, 2552-2554.
113. Rogers, C. T., Inam, A., Hedge, M. S., Dutta, B., Wu, X. D., and Venkatesan, T. (1989) Fabrication of heteroepitaxial $YBa_2Cu_3O_{7-x}$-$PrBa_2CuO_{7-x}$-$YBa_2Cu_3O_{7-x}$ Josephson devices grown by laser deposition, *Appl. Phys. Lett.* **55**, 2032-2034.
114. Kupriyanov, Yu M., and Likharev, K. K. (1991) Towards the quantitative theory of the high-T_c Josephson junctions, *IEEE Trans. Magn.* **MAG-27**, 2460-2463; Beasley, M. R. (1991) Tunneling and proximity effect studies of the high temperature superconductors, *Physica C* **185-189**, 227-233.
115. Barner, J. B., Rogers, C. T., Inam, A., Ramesh, R., and Bersey, S. (1991) All a-axis oriented $YBa_2Cu_3O_{7-y}$-$PrBa_2Cu_3O_{7-x}$-$YBa_2Cu_3O_{7-y}$ Josephson devices operating at 80K, *Appl. Phys. Lett.* **59**, 742-744.
116. Gao, J., Aarnink, W. A. M., Gerritsma, G. J., Veldhuis, D., and Rogalla, H. (1991) Preparation and properties of all high-T_c SNS-type edge dc SQUIDs, IEEE Trans. Magn. MAG-27, 3062-3065.
117. Zani, M. J., Luine, J. A., Simon, R. W., and Davidheiser, R. A. (1991) Focused ion beam high-T_c superconductor dc SQUIDs, *Appl. Phys. Lett.* **59**, 234-236.
118. Tinchev, S. S., Cui, G., Zhang, Y., Buchal, Ch., Schubert, J., Zander, W., Hermann, K., Sodtke, E.,Braginski, A. I., and Heiden, C. (1990) Properties of rf-SQUIDs fabricated from epitaxial YBCO films, LT-19 Satellite Conference on High Temperature Superconductors, Cambridge, England, August 1990 (unpublished).
119. Robbes, D., Miklich, A. H., Kingston, J. J., Lerch, Ph., Wellstood, F. C., and Clarke, J. (1990) Josephson weak links in thin films of $YBa_2Cu_3O_{7-x}$ induced by electrical pulses, *Appl. Phys. Lett.* **56**, 2240-2242; *erratum* **57**, 1169.
120. Lee, L.P., Longo, J., Vinetskiy, V., and Cantor J. (1995) Low noise $Yba_2Cu_3O_{7-\delta}$ direct-current superconducting quantum interference device magnetometer with direct signal injection, *Appl. Phys. Lett.* **66**, 1539-1541.
121. Char, K, Antognazza, L, and Geballe, T.H. (1993) Study of interface resistances in epitaxial $YBa_2Cu_3O_{7-x}$/barrier/$YBa_2Cu_3O_{7-x}$ junctions, *Appl. Phys. Lett.* **63**, 2420-2422; Verhoeven, Martin A. J., Gerritsma, Gerrit J., Rogalla, Horst, and Golubov, Alexander A. (1995) Ramp type HTS Josephson junctions with PrBaCuGaO barriers, *IEEE Trans. Appl. Supercond.* **5**, 2095-2098; Faley, M.I., Poppe, U., Jia, C.L., Dähne, U., Goncharov, Yu, Klein, N., Urban, K., Glyantsev, V.N., Kunkel, G., Siegel, M. (1995) Application of Josephson edge type junctions with a $PrBa_2Cu_3O_7$ barrier prepared with Br-etthanol etching or cleaning, *IEEE Trans. Appl. Supercond.* **5**, 2608-2611; Satoh, T., Kukpriyanov, M. Yu., Tsai, J.S., Hidaka, M., and Tsuge, H. Resonant tunneling transport in YBaCuO/PrBaCuO/YBaCuO edge-type Josephson junctions, *IEEE Trans. Appl. Supercond.* **5**, 2612-2615.
122. Enpuku, K., Shimomura, Y., and Kisu, T. (1993) Effect of thermal noise on the characteristics of a high-T_c superconducting quantum interference device, *J. Appl. Phys.* **73**, 7929-7934.
123. For example: Koch, R. H., Eidelloth, W., Oh, B., Robertazzi, R.P., Andrek, S.A., and Gallagher, W. J. (1992) Identifying the source of l/f noise in SQUIDs made from high-temperature superconductors, *Appl. Phys. Lett.* **60**, 507-509; Keene, M. N., Satchell, J. S., Goodyear, S. W., Humphreys, R. G., Edwards, J. A., Chew, N. G., and Lander, K. (1995) Low noise HTS gradiometers and magnetometers constructed from $YBa_2Cu_3O_{7-x}$/$PrBa_2Cu_3O_{7-y}$ thin films, *IEEE Trans. Appl. Supercond.* **5**, 2923-2926.
124. Koelle, D., Miklich, A.H., Ludwig, F., Dantsker, E., Nemeth, D.T., and Clarke, J. (1993) DC SQUID magnetometers from single layers of $YBa_2Cu_3O_{7-x}$, *Appl. Phys. Lett.* **63**, 2271-2273.
125. Koelle, D., Miklich, A. H., Dantsker, E., Ludwig, F., Nemeth, D. T., Clarke, J., Ruby, W.

and Char, K. (1993) High performance dc SQUID magnetometers with single layer $YBa_2Cu_3O_{7-x}$ flux transformers, *Appl. Phys. Lett.* **63**, 3630-3632.

126. Cantor, R., Lee, L.P., Teepe, M., Vinetskiy, V., and Longo, J. (1995) Low-noise, single-layer $YBa_2Cu_3O_{7-x}$ dc SQUID magnetometers at 77K, *IEEE Trans. Appl. Supercond.* **5**, 2927-2930.
127. Ludwig, F., Koelle, D., Dantsker, E., Nemeth, D. T., Miklich, A. H., Clarke, John and Thomson, R. E. (1995) Low noise $YBa_2Cu_3O_{7-x}/SrTiO_3/YBa_2Cu_3O_{7-x}$ multilayers for improved superconducting magnetometers, *Appl. Phys. Lett.* **66**, 373-375.
128. Zimmerman, J. E. (1971) Sensitivity enhancement of superconducting quantum interference devices through the use of fractional-turn loops, *J. Appl. Phys.* **42**, 4483-4487.
129. Drung, D., Cantor, R., Peters, M., Scheer, H. J., and Koch H. (1990) Low-noise high-speed dc superconducting quantum interference device magnetometer with simplified feedback electronics, *Appl. Phys. Lett.* **57**, 406-408.
130. Drung, D., Cantor, R., Peters, M., Rhyänen, T., and Koch H. (199') Integrated dc SQUID magnetometer with high dV/dB, *IEEE Trans. Magn.* MAG-**27**, 3001-3004.
131. Drung, D., Knappe, S., and Koch, H. (1995) Theory for the multiloop dc superconducting quantum interference device magnetometer and experimental verification *J. Appl. Phys.* **77**, 4088-4098.
132. Ludwig, F., Dantsker, E., Kleiner, R., Koelle, D., Clarke, John, Knappe, S., Drung, D., Koch, H., Alford, Neil McN., and Button, T.W. (1995) Integrated high-T_c multiloop magnetometer, *Appl. Phys. Lett.* **66**, 1418-1420.
133. Button, T. W., Alford, N. McN., Wellhofer, F., Shields, T. C., Abell, F. S. and Day, M. (1991) The processing and properties of high-T_c thick films, *IEEE Trans. Magn.* **MAG-27**, 1434-1437.
134. Ludwig, F., Dantsker, E., Koelle, D., Kleiner, R., Miklich, A. H., Nemeth, D. T., Clarke, John, Drung, D., Knappe, S., and Koch, H. (1995) High-T_c multilayer magnetometers with improved l/f noise, *IEEE Trans. Appl. Supercond.* **5**, 2919-2922.
135. Dantsker, E., Ludwig, F., Kleiner, R., Clarke, John, Teepe, M., Lee, L. P., Alford, Neil McN., and Button, T. (1995) Addendum: Low noise $YBa_2Cu_3O_{7-x}$ $/SrTiO_3/YBa_2Cu_3O_{7-x}$ multilayers for improved superconducting magnetometers, *Appl. Phys. Lett.* **67**, 725-726.
136. Lee, L. P., Char, K., Colclough, M. S., Zaharchuk, G. (1991) Monolithic 77K dc SQUID magnetometer, *Appl. Phys. Lett.* **59**, 3051-3053.
137. David, B., Grundler, D., Krumme, J.-P., and Dössel, O. (1995) Integrated high-T_c SQUID magnetometer, *IEEE Trans. Appl. Supercond.* **5**, 2935-2938.
138. Hilgenkamp, J. W. M., Brons, G. C. S., Soldevilla, J. G., Isselsteijn, R. P., Flokstra, J., and Rogalla, H. (1994) Four layer monolithic integrated high-T_c SQUID magnetometer *Appl. Phys. Lett.* **64**, 3497-3499.
139. Dössel, O., David, B., Eckart, R., Grundler, D., and Krey, S. (1995) High-T_c SQUID magnetometers for magnetocardiography, in Dave H. A. Blank (ed.), *Proceedings of the HTS Workshop on Applications and New Materials*, University of Twente, Enschede, pp. 124-130.
140. Kromann, R., Kingston, J. J., Miklich, A. H., Sagdahl, L. T., and Clarke, John (1993) Integrated high-transition temperature magnetometer with only two superconducting layers, *Appl. Phys. Lett* **63**, 559-561.
141. Zhang, Y., Mück, M., Herrmann, K., Schubert, J., Zander, W., Braginski, A., and Heiden, C., (1992) Low noise $YBa_2Cu_3O_{7-x}$ rf SQUID magnetometer, *Appl. Phys. Lett.* **60**, 645-647.
142. Zhang, Y., Mück, M., Herrmann, K., Schubert, J., Zander, W., Braginski, A., and Heiden, C., (1992) Microwave rf SQUID integrated into a planar $YBa_2Cu_3O_{7-x}$, *Appl. Phys. Lett.* **60**, 2303-2305.

143. Ketchen, M. B., Gallagher, W. J., Kleinsasser, A. W., Murphy, S., and Clem, J. R. (1985) DC SQUID flux focuser, in H.D. Hahlbohm and H. Lübbig (eds), *Proceedings of SQUID '85*, Berlin, pp. 865-871.
144. Zhang, Y., Krüger, U., Kutzner, R., Wördenweber, R., Schubert, J., Zander, W., Strupp, M., Sodtke, E., and Braginski, A.I. (1994) Single layer $YBa_2Cu_3O_7$ radio frequency SQUID magnetometers with direct-coupled pickup coils and flip-chip flux transformers, *Appl. Phys. Lett.* **65**, 3380-3382.
145. Ferrari, M. J., Johnson, M., Wellstood, F. C., Clarke, J., Rosenthal, P. A., Hammond, R. H., and Beasley, M. R. (1988) Magnetic flux noise in thin-film rings of $YBa_2Cu_3O_{7-\delta}$, *Appl. Phys. Lett.* **53**, 695-697.
146. Ferrari, M. J., Johnson, M., Wellstood, F. C., Clarke, J., Inam, A., Wu, X. D., Nazar, L., and Venkatesan, T. (1989) Low magnetic flux noise observed in laser-deposited *in situ* films of $Yba_2Cu_3O_y$ and implications for high-T_c SQUIDs, *Nature* **341**, 723-725.
147. Ferrari, M. J., Johnson, M., Wellstood, F. C., Clarke, J., Mitzi, D., Rosenthal, P. A., Eom, C. B., Geballe, T. H., Kapitulnik, A., and Beasley, M. R. (1990) Distribution of flux-pinning in $YBa_2Cu_3O_{7-\delta}$ and $Bi_2Sr_2CaCu_2O_{8+\delta}$ from flux noise, *Phys. Rev. Lett.* **64**, 72-75.
148. Koch, R. H., Sun, J. Z., Foglietti, V., and Gallagher, W. J. (1995) Flux dam, a method to reduce extra low frequency noise when a superconducting magnetometer is exposed to a magnetic field, *Appl. Phys. Lett.* **67**, 709-711.
149. Miklich, A. H., Koelle, D., Ludwig, F., Nemeth, D. T., Dantsker, E., and Clarke, John (1995) Picovoltmeter based on a high transition temperature SQUID, *Appl. Phys. Lett.* **66**, 230-232.
150. Dantsker, E., Koelle, D., Miklich, A. H., Nemeth, D. T., Ludwig, F., Clarke, John, Longo, J. T., and Vinetskiy, V. (1994) High-T_c three-axis dc SQUID magnetometers for geophysical applications, *Rev. Sci. Instrum.* **65**, 3809-3813.
151. Black, R. C., Wellstood, F. C., Dantsker, E., Miklich, A. H., Koelle, D., Ludwig, F., and Clarke, J. (1995) High frequency magnetic microscopy using a high-T_c SQUID, *IEEE Trans. Appl. Sup.* **5**, 2137-2141.
152. Kado, H. (1994) Applied Superconductivity Conference, Boston, MA, October 1994 (unpublished).